

ELECTRON TRANSPORT AND DEPHASING IN SEMICONDUCTOR QUANTUM DOTS

A DISSERTATION
SUBMITTED TO THE DEPARTMENT OF ELECTRICAL ENGINEERING
AND THE COMMITTEE ON GRADUATE STUDIES
OF STANFORD UNIVERSITY
IN PARTIAL FULFILLMENT OF THE REQUIREMENTS
FOR THE DEGREE OF
DOCTOR OF PHILOSOPHY

Andrew G. A. Huibers
March 1999

© Copyright 2000 by Andrew Huibers
All Rights Reserved

I certify that I have read this dissertation and that in my opinion it is fully adequate, in scope and quality, as a dissertation for the degree of Doctor of Philosophy.

Charles M. Marcus
(Principal Advisor)

I certify that I have read this dissertation and that in my opinion it is fully adequate, in scope and quality, as a dissertation for the degree of Doctor of Philosophy.

James S. Harris Jr.

I certify that I have read this dissertation and that in my opinion it is fully adequate, in scope and quality, as a dissertation for the degree of Doctor of Philosophy.

Yoshihisa Yamamoto

Approved for the University Committee on Graduate Studies:

Abstract

At low temperatures, electrons in semiconductors can be phase coherent over distances exceeding tens of microns and are sufficiently monochromatic that a variety of interesting quantum interference phenomena can be observed and manipulated.

This work discusses electron transport measurements through cavities (quantum dots) formed by laterally confining electrons in the two-dimensional sub-band of a GaAs/AlGaAs heterojunction. Metal gates fabricated using e-beam lithography enable fine control of the cavity shape as well as the leads which connect the dot cavity to source and drain reservoirs.

Quantum dots can be modeled by treating the devices as chaotic scatterers. Predictions of this theoretical description are found to be in good quantitative agreement with experimental measurements of full conductance distributions at different temperatures. Weak localization, the suppression of conductance due to phase-coherent backscattering at zero magnetic field, is used to measure dephasing times in the system. Mechanisms responsible for dephasing, including electron-electron scattering and Nyquist phase relaxation, are investigated by studying the loss of phase coherence as a function of temperature.

Coupling of external microwave fields to the device is also studied to shed light on the unexpected saturation of dephasing that is observed below an electron temperature of 100 mK. The effect of external fields in the present experiment is explained in terms of Joule heating from an ac bias.

Acknowledgements

Even with cheap labor, mesoscopic physics research is an expensive endeavor requiring much specialized equipment and many dewars full of liquid Helium. Financial support for this work came from several sources, including the Army Research Office under Grant DAAH04-95-1-0331, the Office of Naval Research YIP program under Grant N00014-94-1-0622, the NSF-NYI and PECASE programs, the A. P. Sloan Foundation, and from JSEP under Grant DAAH04-94-G-0058.

I was personally supported with a fellowship from Fannie and John Hertz Foundation. This extra cushion made the difference between worrying about finances and not, and I am grateful for it, and it also freed up an RA slot for another student.

Experimental physics is a group effort – one doesn’t see any single author papers in experimental quantum transport. Members of the Marcus group put in long hours to help each other out, in fixing equipment, device fab, experimental advice, data analysis, and many other activities; this contributed greatly to the research environment. Marcus group members during my tenure include Sam Patel, Sara Cronenwett, Mike Switkes, Duncan Stewart, Joshua Folk, Randy True, Steve Grossman, Kevin Birnbaum, Dave Sprinzak, Sandra Godijn, Rob van der Hage, John Stockton and Sebastian Maurer – I wish them all well in their future endeavors.

My advisor Charles Marcus was a constant source of perspective and input during this entire experimental endeavor. His constant enthusiasm, intellectual rigor, and high standards were extremely valuable, and necessary, for this project. Charlie is also a terrific ambassador and has encouraged and organized interaction with many if not most of the world’s best theorists in our field of interest.

Wolfgang Jung of the Physics machine shop and Tom Carver of the Ginzton Microfab were both big contributors to my research efforts.

My reading and orals committee, Professors Y. Yamamoto, J. S. Harris Jr. and U. Inan,

have my appreciation for taking time out of their very busy schedules to help me on my Ph.D path. Professor Harris' group grew some of the excellent low-noise 2DEG that we used in our experiments, and I have had many good interactions with the students in the Yamamoto group during my career at Stanford.

Out of lab, many friends made the last five years a quality experience, especially SMC, IKC, and YDR. Catamaran sailing and sinking, Sierra mountaineering, motorcycles, ultimate frisbee, all these good things started in California for me.

Finally, my parents have provided constant encouragement on my educational route through a Ph.D. with its many twists and turns, and I wish to sincerely thank them here for all of their help.

Contents

Abstract	iv
Acknowledgements	v
1 Introduction	1
1.1 Introduction	1
1.2 The GaAs/Al _x Ga _{1-x} As System and Depletion Gating	3
1.3 Quantum Interferometry	4
1.4 Quantum Point Contacts	8
1.5 Features of Quantum Dot Transport	10
1.6 Organization of This Dissertation	13
2 Basic Q-Dot Transport: Theory and Experiment	15
2.1 Quantum Dot Transport Overview	15
2.2 Quantum Dot Structure	15
2.2.1 Quantum Point Contacts	16
2.2.2 Reservoirs	16
2.2.3 Quantum Dot Characteristic Scales	17
2.3 Semi-Classical Transport	17
2.4 The Scattering Matrix and Landauer Formalism	19
2.5 Random S Matrices	20
2.5.1 Justification for RMT	21
2.5.2 Distributions	21
2.5.3 Dephasing and RMT	23
2.5.4 Thermal Smearing	25

2.5.5	Experimental technique	29
2.5.6	Significance of Distribution Results	31
2.5.7	Conductance Derivatives	32
2.6	Supersymmetry Theory	32
2.6.1	Conductance autocorrelation	32
2.6.2	Temperature	34
2.6.3	High Temperature $C(E)$	35
2.6.4	High Temperature $C(B)$	36
2.6.5	Equivalence of Supersymmetry Theory and RMT	36
3	Dephasing Measurements in Quantum Dots	39
3.1	High Temperature Dephasing Measurements	40
3.1.1	Background	40
3.1.2	Related Experimental Work	40
3.1.3	Experiment	41
3.1.4	Weak Localization and Dephasing Times	43
3.1.5	Other techniques to measure τ_ϕ	43
3.2	Low Temperature Dephasing and Saturation of τ_ϕ	46
3.2.1	Experiment	47
3.2.2	Electron-electron interactions	54
3.3	Transport Under High Bias	55
3.3.1	Detailed balance model	55
3.3.2	Experimental results	56
3.4	Coulomb Blockade at $N = 1$	57
4	Dephasing and Interaction Mechanisms	59
4.1	Loss of Phase Coherence	59
4.2	Electron-electron scattering (T^2)	60
4.3	High Frequency Electric Fields	61
4.4	Nyquist mechanism	63
4.5	Quantum Dot Quasiparticle Lifetime	63
4.6	Intrinsic Dephasing	64
4.7	Electron-phonon Scattering	65
4.8	Spin-orbit Scattering	65

4.9	Summary	66
5	Microwave Excitation of Quantum Dots	67
5.1	Introduction	67
5.2	Measurements	69
5.2.1	Joule heating	72
5.2.2	Non-linear Coulomb blockade	76
5.3	Discussion	79
6	Discussion and Conclusions	81
6.1	Research Context and Philosophy	81
6.2	Summary of Accomplishments and Results	82
6.3	Future Directions	83
A	Nanofabrication	85
A.1	Fabrication Introduction	85
A.2	Photomask and e-Beam Designs	86
A.3	Photolithography	86
A.4	Electron Beam Lithography	88
A.5	Ohmic Contacts	92
A.6	Mesa Etching	92
A.7	Packaging and Wire Bonding	92
B	2D Electron Gases and Devices	95
B.1	Two-dimensional electron gases	95
B.1.1	Wafer CEM2385	96
B.1.2	Wafer 940708A	97
B.2	Device Inventory	98
B.2.1	Dots I613, I75	98
B.2.2	Dot I77	99
B.2.3	Dot I74	99
B.2.4	Dot C14	99
B.2.5	Dot C79, C63	100
B.2.6	Dot C22	100
B.2.7	Dots C32, C70	100

B.2.8	Dots C88, C15	101
C	Cold Filter	102
C.1	Motivation	102
C.2	Technical Description	102
C.3	Advantages over other methods	103
D	Measurement System	105
D.1	Cryostats	105
D.2	Measurement Configurations	106
D.3	General Observations	107
D.4	High-resistance Measurements	108
D.4.1	Combined AC/DC Measurements	109
D.5	Software	109
E	Non-linear Coulomb Blockade Model	111
E.1	Description	111
E.2	Source Code	112
	Bibliography	115

List of Tables

1.1	Typical electronic properties of GaAs/Al _x Ga _{1-x} As based 2DEG and Au films	2
2.1	Quantum dot characteristic scales	17
2.2	Theoretical <i>var(g)</i> results summary	38

List of Figures

1.1	Gated quantum dot structure	3
1.2	Band diagram of a GaAs-AlGaAs heterostructure	4
1.3	Two dimensional chaotic interferometer	5
1.4	Different types of interferometers	6
1.5	Interference fluctuations vs. magnetic field and gate voltage	7
1.6	Perspective view of a quantum dot	8
1.7	Quantum point contact and measured conductance plateaus	9
1.8	Conductance through a quantum point contact	10
1.9	Imperfect quantum point contact	11
1.10	Conductance landscape for quantum dot transport	12
1.11	Weak localization and average conductance	13
2.1	Theoretical conductance distributions for $N = 1$, $T = 0$, no dephasing. . . .	22
2.2	Experimental conductance distributions for $N = 1$	23
2.3	Theoretical conductance distributions for $N = 1$, $T = 0$, and dephasing rates $\gamma_\varphi = 1$ and $\gamma_\varphi = 0$	25
2.4	Theoretical conductance distributions for $N = 1$, $kT = 0.6\Delta$, and no dephasing	27
2.5	Measured transport quantities $\langle g \rangle$, γ_φ , $var(g)$ vs. T	28
2.6	Experimental conductance distributions at four temperatures	30
2.7	Conductance derivatives $P(dg/dV_g)$ at $B = 0$ and 40 mT	33
2.8	Thermal envelopes $f'(E)$ and $C(E, T)$	35
2.9	Energy conductance power spectrum at high T	36
3.1	Shape-averaged magnetoconductance unaveraged conductance for $4.0 \mu\text{m}^2$ dot	42
3.2	Shape-averaged weak localization amplitude	44
3.3	Phase coherence time τ_φ vs. temperature	45

3.4	Comparison of $\tau_\varphi(T)$ extracted using various methods	46
3.5	Weak localization amplitude δg vs. temperature	47
3.6	Conductance variance vs. temperature for identical devices	48
3.7	Phase coherence time τ_φ vs. temperature for dots with different areas . . .	49
3.8	Phase coherence time $\tau_\varphi(T)$ for two $8 \mu\text{m}^2$ dots	51
3.9	$\tau_\varphi(T)$ in a single $8 \mu\text{m}^2$ device (C88) taken different days	52
3.10	$\tau_\varphi(T)$ in a single device (C15) at $N = 1$ and $N = 2$ modes per channel . . .	52
3.11	Composite $\tau_\varphi(T)$	53
3.12	Electron energy distributions in reservoirs and dot under large bias	56
3.13	Magneto-conductance for different temperatures and source-drain biases . .	56
3.14	Equivalent dot temperature vs. source-drain bias	57
3.15	Traces of Coulomb blockade in $2.0 \mu\text{m}^2$ dot at $N = 1$ and $B = 0$ mT	58
3.16	Traces of Coulomb blockade in $2.0 \mu\text{m}^2$ dot at $N = 1$ and $B = 20$ mT . . .	58
4.1	Fermi surface and k vectors	61
4.2	Weak localization curves with Lorentzian fits	65
5.1	Weak localization amplitude δg vs. conductance variance	68
5.2	Magneto-conductance curves for incremental power levels at 700 MHz . . .	70
5.3	Temperature-induced and radiation-induced magneto-conductance comparison	71
5.4	$g(V)$ curves at 200 MHz matched to reference curve at 1 GHz	71
5.5	Best match to reference $g(V)$ curve at several frequencies	72
5.6	Coulomb blockade peak width in $1 \mu\text{m}^2$ dot vs. microwave power	73
5.7	dc source-drain voltage required to produce heating effect	74
5.8	Microwave powers required to create temperature-equivalent QPC trace washout	75
5.9	Attenuation of microwave power in rigid coax in dilution refrigerator	75
5.10	Non-linear Coulomb blockade plots of conductance vs. drain-source voltage V_{SD} and gate voltage V_{gate}	76
5.11	Differential conductance and dc current through the Coulomb blockaded dot	77
5.12	Current through dot in Coulomb blockade mode vs. gate voltage and source- drain voltage	78
A.1	Lithographic patterns used in quantum dot fabrication	86
A.2	Electron micrograph of device	87

A.3	Example of the e-beam lithography capability	90
A.4	e-beam patterns	91
A.5	Electron micrograph of the device showing alignment	91
A.6	SEM image of bonded device	93
A.7	SEM image of two chips side by side in ceramic chip carrier	94
B.1	Effect of a “switcher” on the conductance	96
B.2	Band diagram showing layers and position of 2DEG	97
C.1	Filter unit and cold finger of dilution refrigerator	104
D.1	Connection diagram for four-wire current bias mode	106
D.2	Battery box circuit	107
D.3	Differential amplifier circuit	108
D.4	Connection diagram for voltage bias mode	109
D.5	Connection diagram for voltage bias, V and I measuring mode	110
E.1	Coulomb blockade diamonds and example simulation	112

Chapter 1

Introduction

1.1 Introduction

Until recently, designers of man-made electronic devices have required little understanding of the basic laws of quantum mechanics. Clearly the electronic band structure of a conductor or semiconductor is dictated by quantum mechanics in the same way as chemical bond structure. However, the properties of electron flow can usually be abstracted using a fluid-like model requiring only a knowledge of bulk properties and the dimensions of the container.

This picture has been radically modified with the advent of new artificial systems in which the phase coherence, as well as the quantization of an electron's motion and charge, are very important, and can even completely determine electronic transport. The new field that encompasses much of this work has been coined “mesoscopic” physics. A universal feature of mesoscopic systems is that the coherence length can be larger than one or more dimensions of the device (container) under study. With the help of sub-Kelvin cryogenic measurement equipment, electronic coherence lengths of over 100 microns can be observed, well within the range of today's nanometer-scale fabrication techniques. In addition, low-density semiconducting systems can have conduction electrons with very large electronic wavelengths up to ~ 60 nm, approximately 200 times the atomic scale. With electron beam lithography, one can pattern arbitrary shapes near the scale of one wavelength.

From a physics perspective, mesoscopic systems give insight into fundamental issues relating to quantum mechanical systems. Recent developments in quantum computing have highlighted the importance of increasing our understanding of decoherence and quantum interactions in general. Our present study of dephasing in quantum dots is significant in that

		GaAs/ Al _x Ga _{1-x} As	Au film 20 nm thick	units
Effective mass	m_e	0.067	1.1	$m_e = 9.1 \cdot 10^{-28} \text{g}$
Density of states	$\rho(E)$	0.28×10^{11}	8	$\text{cm}^{-2} \text{meV}^{-1}$
Areal density (typ.)	n	2×10^{11}	$\sim 10^{13}$	cm^{-2}
Fermi velocity	v_F	1.9	14	10^7cm/s
Mobility	μ_e	10^6	20	cm^2/Vs
Elastic scattering time	τ_e	40	0.013	pS
Diffusion constant	D	7000	135	cm^2/s
Fermi wavelength	λ_F	60	0.5	nm
Mean free path	l_e	7	0.02	μm
Cyclotron radius	l_{cycl}	70	–	$\text{nm}(\text{B/T})^{-1}$
Thermal length (100 mK)	l_{th}	16	–	μm

Table 1.1: Typical electronic properties of GaAs/Al_xGa_{1-x}As based 2DEG and Au film (30 nm) systems.

a rich set of interactions becomes accessible. Studying coherence limits in flexible mesoscopic systems will likely result in knowledge of broad interest. The completely artificial nature of quantum dots and related devices sets them apart from much more perfect, but ultimately unmodifiable, atomic and molecular “systems”.

Two of the most popular mesoscopic systems are (1) thin metal films, specifically Au films, widely used because they are convenient to fabricate, and (2) the two-dimensional electron gas (2DEG) formed at the hetero-interface between GaAs and Al_xGa_{1-x}As. The GaAs/AlGaAs hetero-interface can be grown with few if any crystal defects, resulting in fantastically large mean free paths in the 10’s of microns. Many other mesoscopic systems have also been studied. For example, Klaus von Klitzing and coworkers discovered the quantum Hall effect in a silicon MOS structure before the widespread availability of GaAs/Al_xGa_{1-x}As material. 2DEGs based on InAs/AlSb have been used to study hybrid superconductor-2DEG systems, in which the macroscopic superconductor phase can couple to the normal electron phase, and coherent backscattering “Andreev reflection” can occur.

Table 1.1 briefly summarizes typical physical parameters for transport electrons in GaAs/Al_xGa_{1-x}As-based 2DEGs and in a typical Au film with a thickness of 20 nm [Echternach93]. The values for the GaAs/Al_xGa_{1-x}As 2DEG are typical of those used in the experiments described in this thesis.

1.2 The GaAs/Al_xGa_{1-x}As System and Depletion Gating

Devices fabricated from semiconductor 2DEGs enable the direct manipulation and control of electron wave functions. This is due to both the large electronic wavelength, and more importantly, to a MOSFET-like structure in which metal gates situated directly above the 2DEG are able to deplete it. Figure 1.1 shows a side view of the heterostructure, with both contacts to the 2DEG and a depletion gate. Since the 2DEG is typically 50 to 200 nm below the surface of the crystal (and the gates), there is a lateral resolution limit on the ability to control and pattern the electron gas. In practice one can control the wavefunction only to within a few wavelengths in a completely arbitrary way.

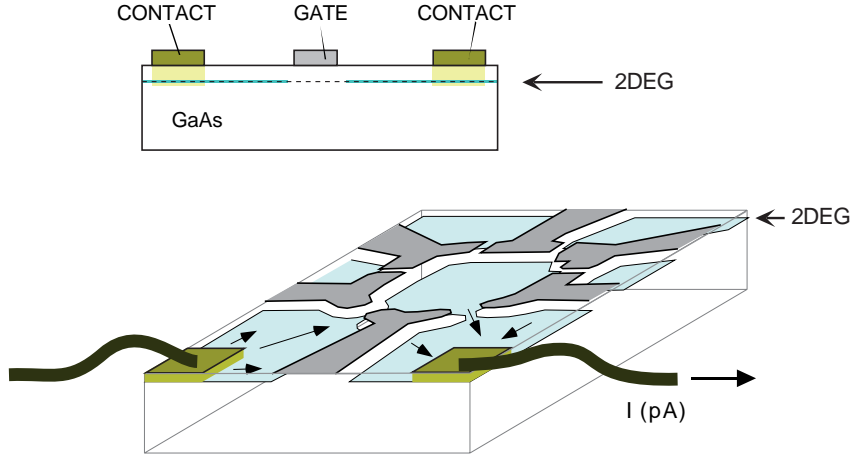


Figure 1.1: Side and perspective view of gated quantum dot structure.

A perspective dot formed using depletion gates is shown in the bottom of Figure 1.1. The 2DEG lies just under the surface. Two openings allow current to pass through the device. Measuring the conductance through the device is the fundamental means by which it is probed. In different regimes of operation, one can resolve information about energy, wave function intensity, and aggregate trajectory interference with conductance measurements.

Figure 1.2 shows the band structure which supports the 2D electron gas. Starting at the wafer surface, the GaAs cap passivates the surface from oxidation, the n-doped region provides carriers to occupy the quantum well, and the AlGaAs spacer keeps the donor sites away from the well, enhancing mobility. The 2DEG itself is defined by the quantum well formed at the interface of the AlGaAs and the bulk GaAs. A superlattice is usually added

to isolate the structure from the substrate (not shown).

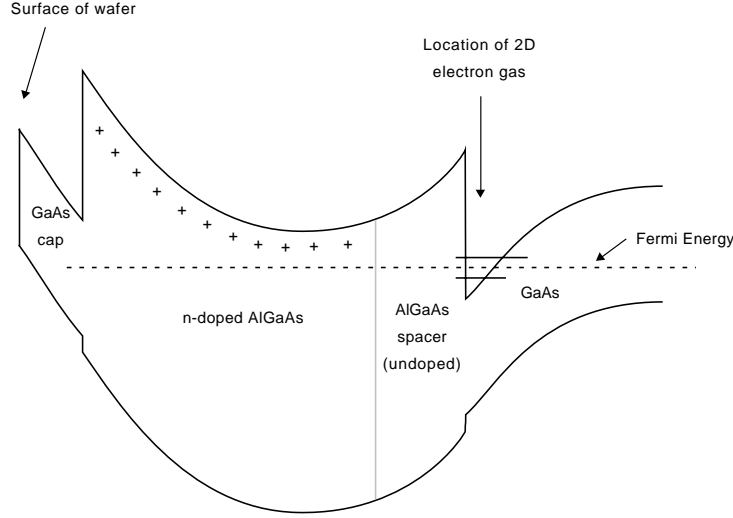


Figure 1.2: Band diagram of a GaAs/AlGaAs heterostructure created to support a high-mobility two-dimensional electron gas.

The 2D electron system created at this interface is very useful experimentally because, in addition to the large electron wavelength, GaAs and AlGaAs are almost perfectly lattice matched. As a result if the crystal is grown carefully, there are few of the normal interfacial defects due to lattice mismatch, and the mean free path (the average distance an electron wave can travel with suffering a collision) can be over 100 microns, limited only by the presence of nearby dopants (donor impurities). It is convenient that $\text{Al}_x\text{Ga}_{1-x}\text{As}$ has a simple band structure for mixture ratio $x < 0.4$, with a circular Fermi surface. Thus, the quasiparticles in the 2DEG behave like electrons, with only an effective mass substitution.

1.3 Quantum Interferometry

Electron behavior at atomic scales is governed by the Schrödinger equation, a complex-valued scalar wave equation. For an ideal 2D electron gas without interactions, the equation is separable (the z wavefunction is the quantum well ground state), and valid solutions for individual electrons are planewaves. Under typical measurement conditions, the Fermi energy is ~ 7 eV and kT for 100 mK is ~ 8.6 μeV , so the planewaves are nearly monochromatic.

A dot similar to those measured in this thesis is shown in Figure 1.3 with a simulated

wavefunction [Akis97]. If the dot is sufficiently ‘open’ such that the leads each support one or more transverse electron modes, a trajectory picture is valid, and one can visualize different trajectories from a (partly diffractive) entrance lead combining at the exit to create fluctuations in transmittance T (bottom Figure 1.3). If any parameter that affects the accumulated phase of the trajectories is altered, such as the electronic wavelength (directly related to energy), the interference pattern changes. If some of the waves contributing to the interference lose their coherence, or have a distribution of energies (such as for non-zero temperature), there will only be partial interference.

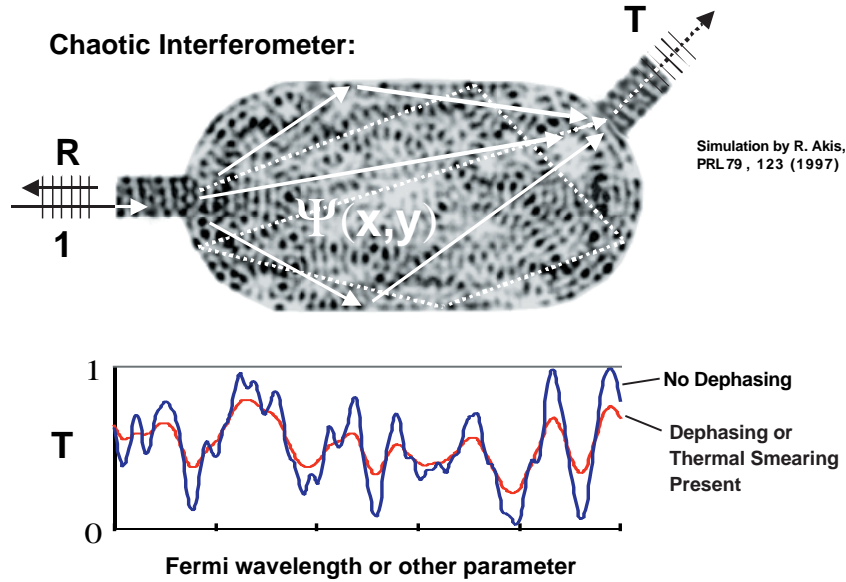


Figure 1.3: A two dimensional chaotic interferometer and simulated transmission fluctuations.

The cavity in Figure 1.3 is the classic stadium-shaped billiard, whose classical dynamics are chaotic. Other types of interferometers are shown in Figure 1.4. Structures with “regular” classical dynamics such as a two-arm interferometer or integrable cavity can be constructed. However due to the limitations of present technology they are imperfect and lead to a mixed phase-space (partly chaotic and partly regular). This is understood by thinking of the 2DEG as an electron sea. Away from the walls, the ocean surface is smooth – most bottom roughness is screened, creating long mean free paths. At the shoreline, however, the rocky bottom is exposed. Any wave reflecting off of the edge of the device is likely to suffer non-specular scattering due to border irregularities. Thus cavities made using

GaAs/AlGaAs 2DEG technology can never be perfectly regular. In contrast, the chaoticity of cavities in which chaotic trajectories are dominant is unaffected by perturbations, since the trajectories traverse phase space evenly. Therefore if one fabricates a chaotic cavity, one gets a chaotic cavity. Fortunately, the present understanding of the statistical behavior of chaotic structures has good theoretical support, which makes these structures appealing.

In a device open to a set of reservoirs, charging interactions are observed to have minimal effect on the *structure* of transport, and can be parameterized with a dephasing rate. Phenomena exhibited by closed structures however, such as Coulomb blockade peak spacing distributions, appear to be fundamentally altered by interactions [Sivan96, Simmel97, Patel98a].

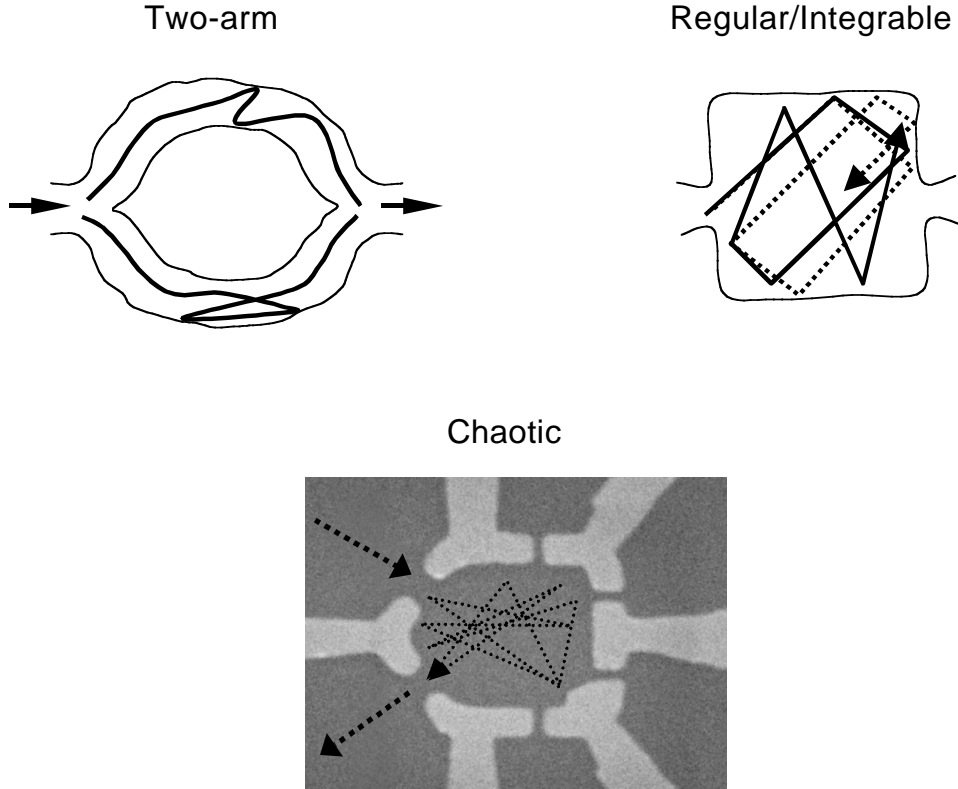


Figure 1.4: Different types of interferometers.

Some experimental data from a GaAs/AlGaAs quantum dot is shown in Figure 1.5 where conductance fluctuations (g) are shown as a function of perpendicular magnetic field, and as a function of the voltage applied to a side gate. The field modifies the phase of looped

paths due to the Aharonov-Bohm phase, and the gate voltage affects the length, and thus the accumulated phase, of paths reflected from this gate. In Figure 1.5 the dot area is about $2 \mu\text{m}^2$, and the Fermi wavelength is 60 nm. If there were no dephasing or thermal (energy) smearing of the electrons in the device, the conductance should oscillate between 0 and $2 e^2/h$, the latter being the conductance of a fully-conducting single mode lead which connects the device to one of the reservoirs (the leads are single mode in this measurement and for most of the work in this thesis). Regardless of thermal smearing and dephasing, however, the average conductance for magnetic field greater than a few flux quanta is not effected ($= 1.0 e^2/h$). This will be discussed further in the next chapter. This device, like all of those studied in this thesis, are two-lead devices. Quantum dots with more than two leads are an interesting possibility for future work, to study dephasing as well as charging physics.

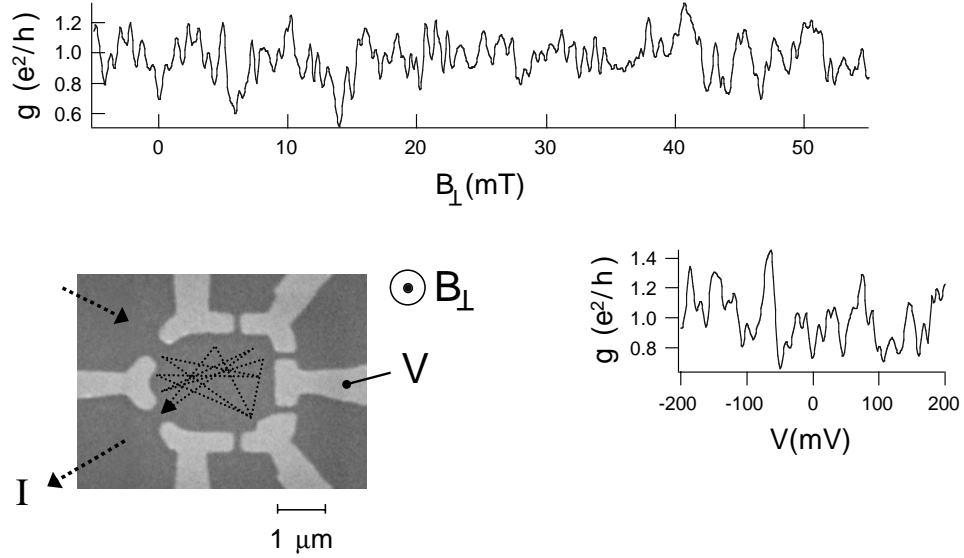


Figure 1.5: Measured interference fluctuations as magnetic field (top) and gate voltage (right) are swept.

A perspective scanning electron micrograph of the device of Figure 1.5 is shown in Figure 1.6. To measure the device, current is driven through the leads labeled I+ and I-, with the resulting voltage measured with V+ and V-. This gives a very accurate determination of the conductance through the device. The shape, energy, area and lead connections to the source and drain are controlled with the six depletion gates that define the device, as seen

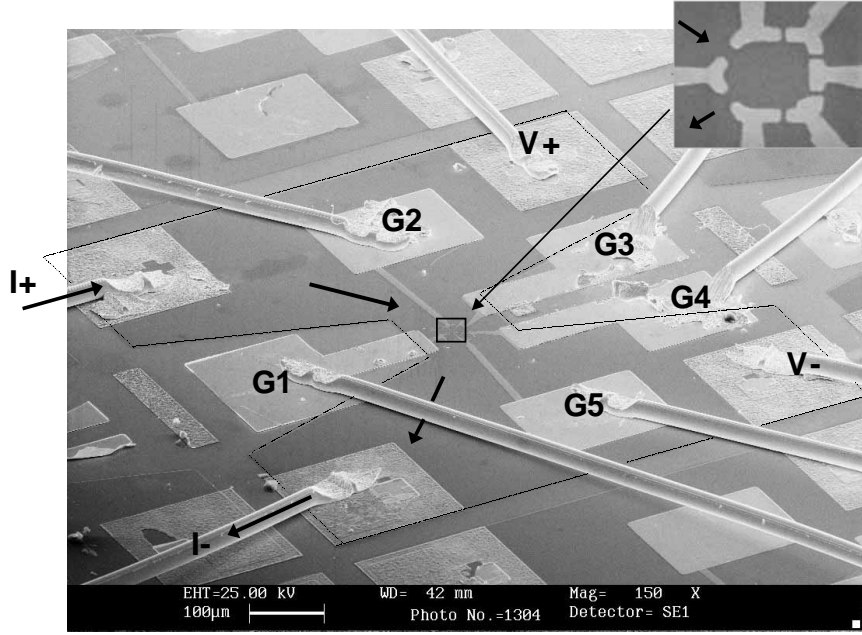


Figure 1.6: Perspective view of a quantum dot as fabricated with blowup of central region.

in the magnified inset. In this device, the 2D electron gas lies 90 nm under the surface. The device is constructed by etching, and by depositing metal layers. A detailed explanation of the fabrication procedure is available in Appendix A.

1.4 Quantum Point Contacts

To provide a more exact picture of how the depletion gated structures operate we consider a fundamental building block for quantum structures which is the quantum point contact (QPC) – a short 1D quantum wire adiabatically coupled to two reservoirs which supports one or more wave modes. These modes are quantized in the two dimensions perpendicular to the direction of propagation. For a small voltage bias each mode carries a quantum of conductance $I = e^2/hV$. The QPC is analogous to a microwave or optical waveguide.

Figure 1.7 shows a QPC schematic. As the gate voltage V_G is made more negative, the narrow channel between the gates is depleted until only a discrete number of transverse modes exist in this quantum “wire”. The graph on the right of the Figure shows the remarkable quantization of the conductance $g = I/V$, as a function of V_G , in unit of $2e^2/h$.

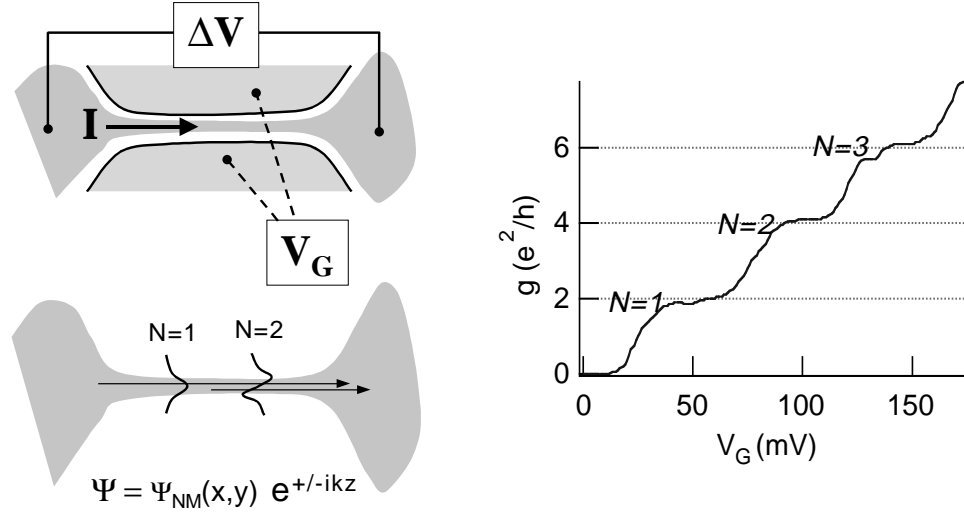


Figure 1.7: Schematic drawing of quantum point contact with measured conductance plateaus.

If the biases applied to the two side gates are independently controlled, the conductance landscape shown in Figure 1.7 results. This type of data were taken for both QPCs on all measured dots to verify that each QPC was free of significant imperfections. All of the gates not adjacent to the QPC under test are biased so as to not deplete the underlying 2DEG.

Most QPCs are not as ideal as that of Figure 1.8— an example is shown in Figure 1.9. The dark streak in Figure 1.9 is likely due to a scatterer. QPCs must be designed so that they are sufficiently smooth to be adiabatic [Beenakker91a], however not long enough to be scattered. Nearly ideal ($g_{max} \simeq e^2/h$) quantum point contacts are required for the quantitative measurements we are after, in order to eliminate free parameters. One solution when presented with a QPC like that in Figure 1.9 is to bias away from the imperfection, moving the conduction channel away from the defect.

In most experiments in this thesis, dots were biased with single mode leads (labeled $N = 1$, where N is the number of modes). In order to create the largest possible relative quantum fluctuations. It is also more accurate to measure long decoherence times if the escape rate from the dot is as slow as possible. Some data were taken with a higher number of modes ($N = 2$ or higher) to check theory and to make sure that Coulomb charging effects were not playing a significant role.

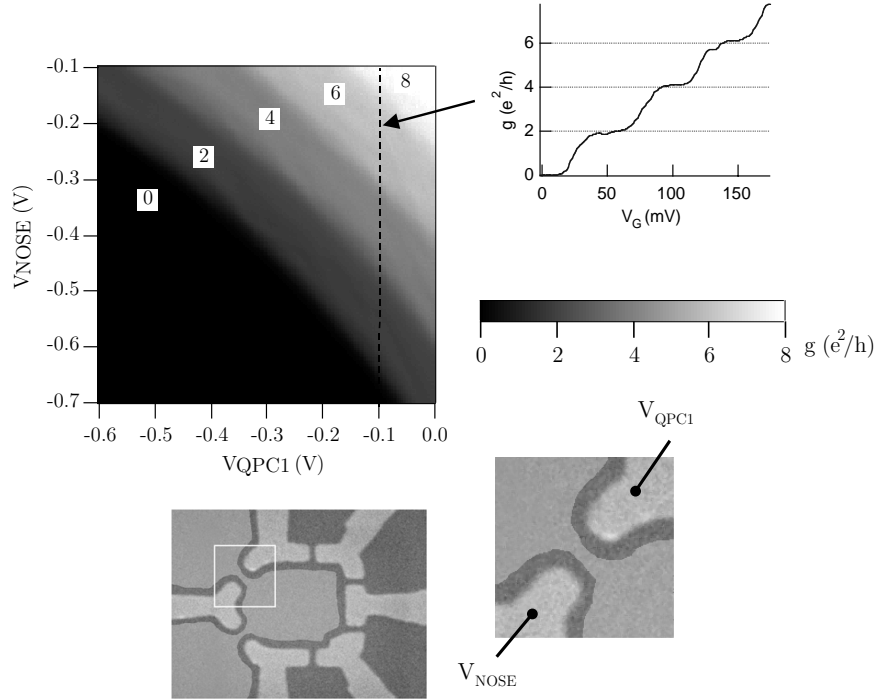


Figure 1.8: Conductance through a quantum point contact. Upper left landscape shows conductance as a function of the two adjacent gate voltages. Scale and cross sectional plot are shown on the right. Electron micrograph of device, and gates being swept for conductance landscape are shown at bottom.

1.5 Features of Quantum Dot Transport

Some introductory insight into phenomena of chaotic quantum transport in quantum dot devices is illustrated in Figure 1.10. This conductance landscape has as its two axes perpendicular magnetic field and gate voltage (the same axes discussed and shown in Figure 1.5). Although here only one gate is being altered, any of the gates may be scanned to create new sets of landscape.

Many statistical features of the fluctuations can be predicted theoretically, including:

- Amplitude of fluctuations at non-zero magnetic field.
- Amplitude of fluctuations for zero magnetic field.
- Average conductance for zero and non-zero field.
- Full distributions of conductance.

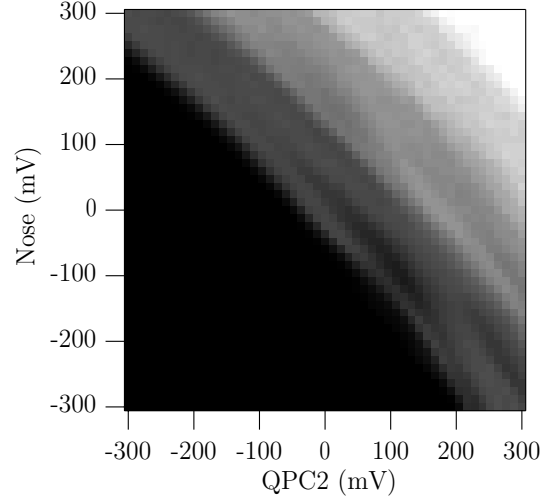


Figure 1.9: Example of an imperfect quantum point contact. Imperfection may be avoided by operating away from the defect.

- Power spectra for fluctuations vs. field and vs. voltage (shape/energy)
- All of the above for $N = 1$, $N = 2 \dots$, and even for tunnel leads ($N \ll 1$).
- All of the above at different temperatures, source-drain bias, and other environmental conditions.

In most mesoscopic systems, conductance fluctuations are tiny, however in small quantum dots they can dominate transport.

A very important phenomena should be highlighted here, which is the *weak localization of electrons* traversing the dot. In the fluctuations of Figure 1.10 there is, on average, a lower conductance at zero perpendicular magnetic field than for non-zero field. Weak localization occurs when a trajectory that enters the dot and then exits back out of the entrance (see Figure 1.11a) interferes constructively with its time-reversed twin thus reducing conductance *through* the device. Trajectories going through the device (entering and exiting through different leads) *have no such twins*. When time-reversal symmetry is broken by a perpendicular magnetic field, the twin-paired paths accumulate different Aharonov-Bohm phase and no longer interfere constructively. In the absence of dephasing, the weak localization effect reduces the conductance through the device between $1/3 e^2/h$ and $1/2 e^2/h$ – a large effect. Usually, dephasing phenomena destroy the phase coherence of the longest paths,

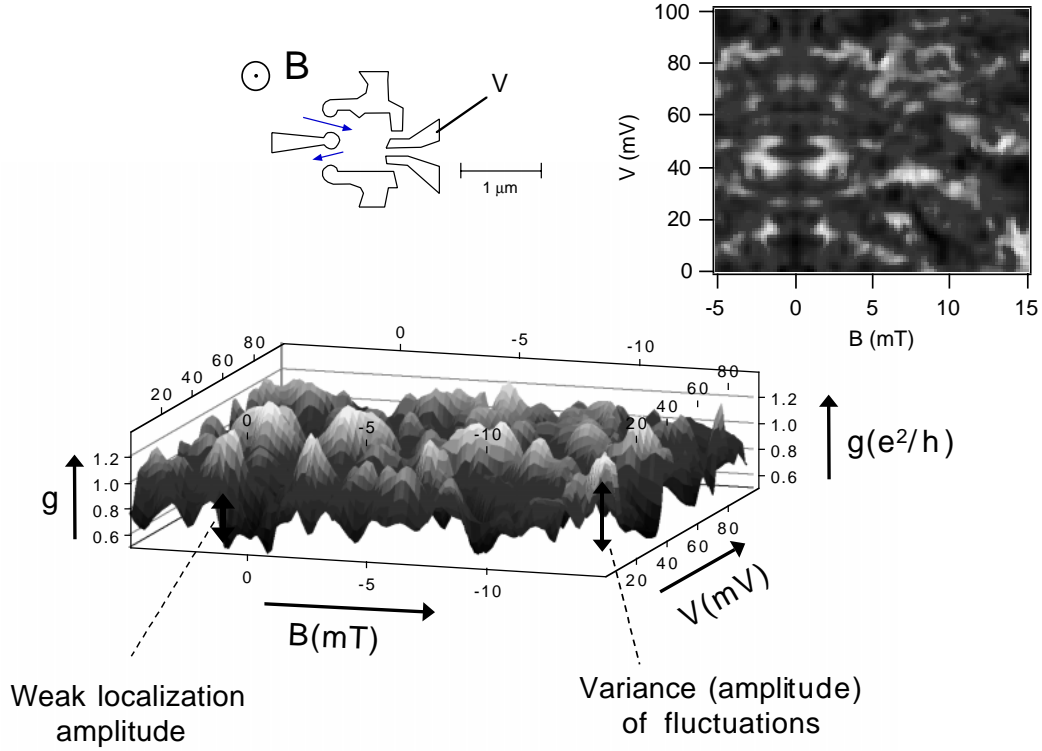


Figure 1.10: Conductance landscape for changing perpendicular magnetic field and gate voltage.

thus reducing the weak localization amplitude. This reduction will be used as the principle metric to measure dephasing in the experiments described in Chapters 3 and 5. The effect of raising the temperature and therefore the dephasing rate, resulting in the suppression of weak localization can be seen in Figure 1.11b which plots the average conductance vs. magnetic field for 400 mK and 1K for a $4\ \mu\text{m}^2$ device. The curves in Figure 1.11b are created by averaging many different magneto-conductance traces as shown in Figure 1.11c.

To sum up, even though analysis of the response of chaotic quantum dots must often rely on average or statistical quantities, these devices enjoy excellent theoretical support (as will be described in Chapter 2) and unparalleled control in a quantum system. All of this combined with the rich array of interaction physics observed makes them a compelling object of study.

For a general introduction to mesoscopic physics concepts, including weak localization, the reader is advised to consult works including refs. [Beenakker91a, Mesoscopic95, Imry97, Ferry97]

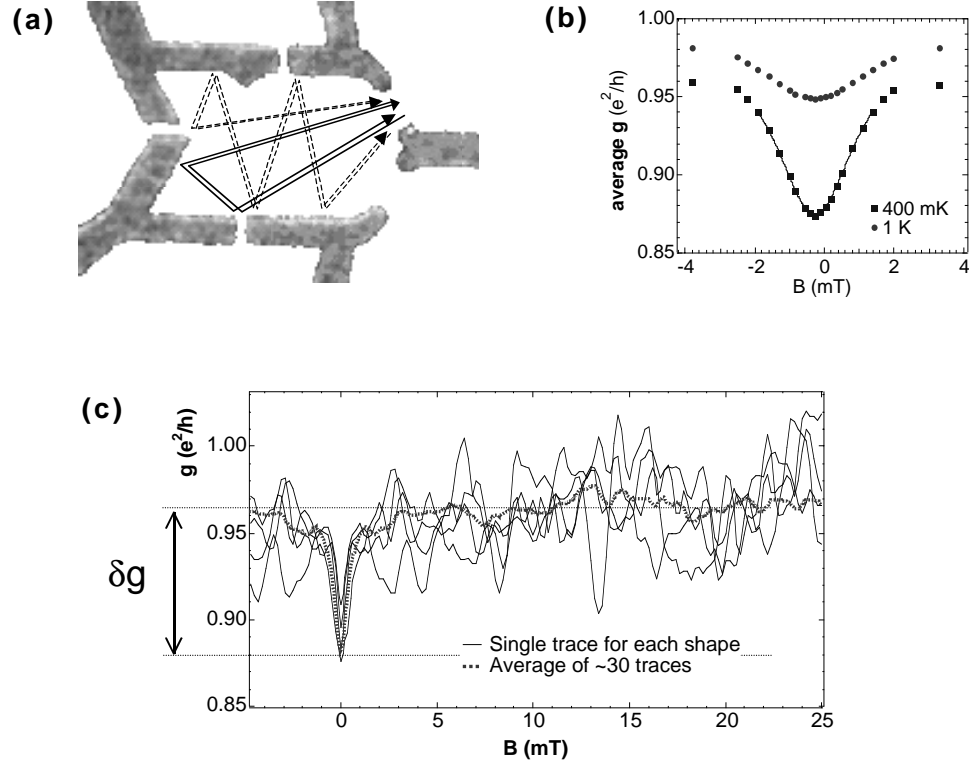


Figure 1.11: (a) path pair contributing to weak localization in $4 \mu\text{m}^2$ quantum dot. (b) average conductance for 400 mK, 1 K for dot shown in (a). 400 mK data is fit to Lorentzian lineshape. (c) Multiple conductance traces average to leave only weak localization response.

1.6 Organization of This Dissertation

This chapter has introduced semiconductor quantum dots as a research topic, and has described building blocks, including basic device construction and the quantum point contact, as well as basic mesoscopic phenomena. These topics will be expanded in the bulk of this dissertation which is organized as follows:

Chapter 2 summarizes, and derives in many places, theory relevant to electron transport measurements in quantum dots, including the effects of temperature and dephasing. Results from transport measurements illustrate the theory.

Chapter 3 describes measurements of the loss of phase coherence (dephasing) in quantum dots, which is studied principally by measuring the weak localization amplitude in many devices over a large parameter space.

Chapter 4 describes several specific decoherence mechanisms. Decoherence is usually

treated as a process described by a dephasing rate; this rate is used as a parameter in the transport theories developed in Chapter 2 to compare to experimental results.

Chapter 5 discusses experiments in which external electromagnetic radiation is deliberately applied to the quantum dots during measurement. This is an important area of investigation because low temperature decoherence is thought to be dominated by electronic-noise-based external or internal (Nyquist) dephasing mechanisms.

Finally, Chapter 6, ties together the results of this research in the context of other experiments, reiterates the conclusions of this work and suggests future avenues of investigation.

Several appendixes provide supplementary information as follows:

Appendix A gives fabrication details, mainly processes that I have developed or improved, and which are in use by our lab.

Appendix B provides detailed information about the specific devices and 2DEGs used in these experiments.

Appendix C describes a cryogenic filter unit that I devised and implemented with an undergraduate researcher. This filter has allowed our group to reach electronic temperatures much lower than previously possible.

Appendix D describes the measurement setups, with brief coverage of the standard cryogenic systems used, and a description of the measurement electronics.

Appendix E gives source code and documentation for a simulation of non-linear Coulomb blockaded quantum dots, in the presence of a thermal electron gas and ac source drain fluctuations.

Despite the frequent use of ‘we’ throughout this thesis, I did the majority of the experimental and analysis effort on all of the experiments described in this dissertation, with the exception of the He-3 system dephasing measurements done in collaboration with Mike Switkes, and many of the radiation experiments, where substantial help was received from Joshua Folk.

Chapter 2

Basic Q-Dot Transport: Theory and Experiment

2.1 Quantum Dot Transport Overview

The behavior of any quantum dot is in principle fully described by Schrödinger's equation. But just as Turing's machine has led to all sorts of fascinations, the simple laws of quantum mechanics give rise to many bizarre and interesting phenomena in condensed matter systems, including superconductivity and composite Fermions.

Quantum dots allow one to gain access to several interesting quantum phenomena. By measuring their conductance, one has a “direct” probe that is not available in other systems. Most real life quantum dots are somewhat imperfect due to disorder (perhaps the only exception to date are the very small vertical quantum dots fabricated at NTT [Tarucha96]). However, the imperfections are exploited, rather than lamented, through the use of a series of statistical metrics to interpret measurements, as we will see in the following sections.

2.2 Quantum Dot Structure

The basic structure of the quantum dots measured in this series of experiments was described in chapter 1: a 2D cavity is connected by two point contacts to source and drain reservoirs. Transport within the cavity is ballistic, as the number of scatterers is low or zero inside the cavity.

2.2.1 Quantum Point Contacts

Conductance quantization in a point contact was first observed by Van Wees [vanWees88], followed closely by Wharam and coworkers [Wharam88]. As discussed in section 1.4, each step in conductance is associated with the addition of a transverse mode (i.e. 1D sub-band) to this 1D electron waveguide. For a hardwalled QPC the number of transverse modes supported is given by $\text{Int}[\frac{k_F W}{\pi}]$. The conductance is perfectly quantized because the 1D density of states is proportional to $E^{-1/2}$, whereas the Fermi velocity $v_F = \hbar k \propto E^{1/2}$. Thus independent of wave energy, the same current is carried by any waveguide mode and is proportional to the bias voltage. The fundamental quantum of conductance is e^2/h , and each fully transmitting QPC carries a conductance of $N \times 2 \times e^2/h$ where N is the number of modes and the 2 accounts for spin degeneracy. In SI units, $h/e^2 = 25.813 \text{ k}\Omega$.

As the energy of the electrons increases, additional modes (sub-bands) are accessed. Ideally, at zero temperature, these are added in an abrupt step-like manner. However, at finite temperature the transport electrons occupy a range of energies described by the Fermi function. Tails of the Fermi function at finite T always extend into higher or lower modes (or are cut off). This causes for the gradual transition between conductance plateaus seen in Figure 1.7. In addition the finite measurement bias results in a small energy spread, although this is normally kept below kT . In the QPC's studied here, the quantum point contacts are well quantized up to $\sim 1\text{K}$.

In an “open” device with QPCs carrying one or more modes, the QPCs act as “mixers” for the various trajectories through the device. In a “closed” device, the QPCs are biased to allow only tunneling conductance ($g \ll e^2/h$, $N \ll 1$), significantly isolating the dot from the reservoirs. Closed QPCs serve to sample the wavefunction at two points on the dot boundary.

2.2.2 Reservoirs

The reservoirs in these experiments are mostly thermalized Fermi seas, with a known initial energy distribution of electrons. In any interference experiment many trajectories through the dot do not decohere significantly, and the waves add up in a quantum mechanical (complex phasor) manner. It is in the reservoirs that there is full decoherence, and we “measure” whether or not the electron has gone through the device, giving us a macroscopic current for an applied voltage.

Area	A	$2.0 \mu\text{m}^2$	
Charge density	ρ	$2.0 \times 10^{11} \text{ e/cm}^2$	
Number of electrons		4000	$\propto A, \rho$
Fermi wavelength	λ_F	60 nm	$\propto 1/\sqrt{\rho}$
$\Delta\lambda_F$ at 100 mK		0.3 nm	
Fermi energy	E_F	7 meV	$\propto \rho$
$\Delta E_F = kT$ at 100 mK		8.6 μeV	
Fermi velocity	v_F	200 $\mu\text{m/ns}$	$\propto \sqrt{\rho}$
Dwell time, two $N = 1$ leads	$\tau_{\text{dwell}} = h/2\Delta$	0.6 ns	$\propto A$
Coherence time	τ_φ	up to 3 ns	
Crossing time	$\tau_{\text{cross}} = \sqrt{A}/v_F$	7 ps	$\propto \sqrt{A}$
No. of wall bounces before escape	$\tau_{\text{dwell}}/\tau_{\text{cross}}$	85	$\propto \sqrt{A}$
Level spacing	$\Delta = \frac{2\pi\hbar^2}{m^*A}$	3.5 μeV	$\propto 1/A$

Table 2.1: Quantum dot characteristic scales

In non-equilibrium situations (see Sec. 3.3), thermalization can occur both inside the device and in the reservoirs. For small devices with short escape times, most “hot” electrons (electrons with excess energy) entering the dot from the source reservoir will keep their energy through the dot and dissipate it in the drain reservoir.

2.2.3 Quantum Dot Characteristic Scales

Several different scales and energies for a typical quantum device are important to keep in mind during the rest of the chapter. Typical parameters are listed in the following table:

The level spacing Δ is the mean separation between energy levels for a closed (isolated) dot. The dwell time is given for an open device with one mode, $N = 1$, in each QPC lead. For a $2.0 \mu\text{m}^2$ device one sees that the coherence time can far exceed the dwell time, and also that a large number of wall reflections (~ 85) occur before escape, leading to a well-mixed phase space.

2.3 Semi-Classical Transport

One definition of the transition from classical to quantum behavior is when the action of the system $S = \int (\vec{p} + e\vec{A}) \cdot d\vec{q}$ is comparable to \hbar (\vec{p} and \vec{A} are the momentum and vector potential operators). Using path formalism [Feynman65], the Schrödinger equation may be

recast in terms of a propagator:

$$\Psi(y, t) = \int e^{iS/\hbar} \Psi(x, 0)$$

The integral is taken over all possible paths from $(x, 0)$ to (y, t) . If the action is much larger than \hbar , only a small tube of paths around the classical trajectory will contribute and one obtains the semi-classical limit, part of the beauty of the approach.

Practically, it is very difficult to sum the paths, and one can obtain a “semi-classical” approximation for the behavior of a quantum system by calculating propagators over all the classical paths weighted correctly. Several useful predictions result from semi-classical analysis of quantum transport for chaotic cavities [Jalabert90, Baranger93a, Baranger93b]. Of relevance for this work, the weak localization lineshape in the conductance is predicted to be Lorentzian:

$$\langle g \rangle = g_0 - \frac{\delta g}{1 + (2B/\alpha\phi_0)^2} \quad (2.1)$$

where α is inverse of the characteristic area swept out by trajectories in the dot, and $\phi_0 = 4.14 \text{ mT } \mu\text{m}^2$ is the flux quantum. This is closely followed by experiment as was shown in Figure 1.11.

The distribution of swept lengths, times and areas before escape are exponential [Marcus95]:

$$\begin{aligned} P(L) &\propto e^{-L/L_c} & L \geq 0 \\ P(t) &\propto e^{-\gamma t} & t \geq 0 \\ P(A) &\propto e^{-2\pi\alpha|A|} \end{aligned}$$

For the above distribution of $P(A)$ it can be derived that the autocorrelation function of conductance fluctuations with respect to magnetic field is Lorentzian-squared [Jalabert90], leading to the power spectrum:

$$S(f) = S(0)[1 + 2\pi\alpha\phi_0 f]e^{-2\pi\alpha\phi_0 f} \quad (2.2)$$

The above results apply to dots with paths which are well-mixed/chaotic, and are suitable for the devices studied here. Conversely, for an integrable cavity (e.g. a perfect square

or circle) the above distributions are typically power laws, and the weak localization line-shape becomes more triangular. This has been observed experimentally [Chang94].

In the case of chaotic scattering, the direction (momentum) and phase of waves inside the cavity quickly become mixed, on a time scale that is short compared to the escape time. This will not fully hold if short paths (i.e. escape before mix) contribute significantly to transport. We design our dots to avoid straight-through or single reflection trajectories. Such trajectories have been investigated numerically [Akis97] who observes diamond trajectories and experimentally in triangular billiards with very open ($N \gg 1$) leads [Linke97b].

The true nature of “quantum chaos” is still an open problem. Chaos in quantum systems is not truly chaos in the strict sense of classical chaos (i.e. extreme sensitivity to initial conditions), since the coherence and escape rates limit the maximum possible paths lengths and thus system sensitivity. Lower size limits (the Fermi wavelength and Δ) means there can be no infinitely fine conductance structure, however the time response of the system can in theory be infinite.

2.4 The Scattering Matrix and Landauer Formalism

Many mesoscopic quantum devices, including quantum dots with waveguide leads supporting one or more modes, may be modeled by a scattering matrix S :

$$w_{\text{out}} = S w_{\text{in}} \quad (2.3)$$

where w_{in} and w_{out} are complex coefficients giving the amplitude and phase of the incoming and outgoing waves. For a discussion of the S matrix based on Schrödinger’s equation see [Datta95] (p. 124). S must be unitary in order for current conservation to exist:

$$|w_{\text{out}}|^2 = |S w_{\text{in}}|^2 = w_{\text{in}}^\dagger S^\dagger S w_{\text{in}} = |w_{\text{in}}|^2 \quad (2.4)$$

The above equation holds only if $S^\dagger = S^{-1}$ which requires $S^\dagger S = I$.

If there are two leads each supporting N modes, then

$$S = \begin{pmatrix} r & t' \\ t & r' \end{pmatrix} \quad (2.5)$$

and $t(t')$ and $r(r')$ are $N \times N$ transmission and reflection matrices for waves incident from

the first (second) lead. The conductance from the first lead through to the second lead (or vice versa) is given by the Landauer formula:

$$g = 2g_0 \sum_{n,m=1}^N t_{mn} = 2g_0 \text{Tr}(tt^\dagger) = 2g_0 \sum_{n=1}^N T_n \quad (2.6)$$

where $g_0 = e^2/h$. The 2 accounts for the spin degeneracy that exists in the absence of spin-orbit scattering. T_n are the transmission eigenvalues of transmission matrix tt^\dagger which are also the eigenvalues of matrices $t't'^\dagger$, $I - rr^\dagger$, and $I - r'r'^\dagger$ [Beenakker97]. The above applies generally; in the presence of time-reversal symmetry ($B = 0$), S must also be symmetric $S = S^T$ [Datta95].

2.5 Random S Matrices

The transport properties of quantum dots are well predicted using Random Matrix Theory (RMT). There is an excellent review of RMT by Beenakker [Beenakker97] and the research articles by Brouwer and Baranger are very accessible to the generalist so I will give only minimal background and results here.

Random matrix theory is motivated by the idea that a quantum dot with certain ergodic properties (i.e. trajectories of partial waves travelling through the dot cavity quickly explore complete phase space and no specific trajectories are preferentially favored) can be described statistically by drawing S from a random ensemble of S matrices obeying the require symmetries.

For two single mode ($N = 1$) leads, S is a 2×2 matrix (Equation 2.5). The average of the conductance $\langle g \rangle$ and conductance variance $\text{var}(g)$ can be calculated for the presence ($\beta = 1$) or absense ($\beta = 2$) of time reversal symmetry:

	$\beta = 1$	$\beta = 2$
$\langle g \rangle$	$\frac{2}{3} \frac{e^2}{h}$	$\frac{e^2}{h}$
$var(g)$	$\frac{16}{45} (\frac{e^2}{h})^2$	$\frac{1}{3} (\frac{e^2}{h})^2$

For $\beta = 2$, S is drawn from the circular unitary ensemble (the matrix eigenvalues are uniformly distributed on the unit circle), and for $\beta = 1$, S is drawn from the circular orthogonal ensemble (the matrices must also be symmetric). For arbitrary N , S is a $2N \times 2N$ scattering matrix, and the generalized conductance and variance results are:

	$\beta = 1$	$\beta = 2$
$\langle g \rangle$	$\frac{2N}{2N+1} \frac{e^2}{h}$	$N \frac{e^2}{h}$
$var(g)$	$\frac{4N(N+1)^2}{(2N+1)^2(2N+3)}$	$\frac{N^2}{4N^2-1}$

2.5.1 Justification for RMT

One would think that a theory with a simple premise would have a simple justification, but this is not true. There are two approaches to justifying RMT based on (1) successful comparison to results from numerical techniques and (2) microscopic derivation relating the S matrix to random Hamiltonians. For more information see [Beenakker97] and [Brouwer97e]. The predictions of RMT are, in identical limits (for example the limit of large N for the above expression for conductance), in full agreement with the same predictions made using super-symmetric methods (see Sec. 2.6).

2.5.2 Distributions

In addition to the distribution moments, $\langle g \rangle$ and $var(g)$ the full conductance distributions for two-lead quantum dots have been calculated within RMT [Jalabert94, Baranger94a,

Beenakker97]. The distributions are universal for any fully chaotic or disordered dot, and are sensitive only to whether time reversal symmetry is obeyed ($\beta = 1$) or broken ($\beta = 2$) (recall that time reversal symmetry can be broken with a perpendicular magnetic field, $|B| > \sim \phi_o/A_{dot}$, where A_{dot} is the dot area and $\phi_o = h/e$ is the flux quantum). Interestingly, RMT yields strongly nongaussian distributions when one or two quantum modes connect the dot to bulk reservoirs.

For single-mode leads, $N = 1$, the distribution is $P(g) = \frac{1}{2}(g/2)^{-1+\beta/2}$ [Jalabert94, Baranger94a], shown in Figure 2.1. The $\beta = 1$ distribution is sharply skewed toward smaller conductance, with average conductance $\langle g \rangle_{\beta=1} = 2/3$, while the $\beta = 2$ distribution is flat with $\langle g \rangle_{\beta=2} = 1$. The lower average conductance for $\beta = 1$ results from coherent backscattering, i.e. weak localization, at $B = 0$.

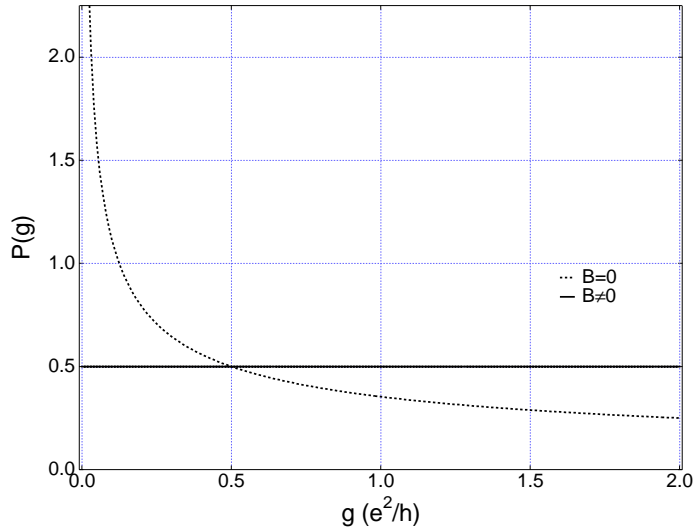


Figure 2.1: Theoretical conductance distributions for $N = 1$, $T = 0$, and no dephasing.

Experimentally obtained distributions are shown in Figure 2.2. The measured distributions are significantly more Gaussian-shaped than the ideal distributions from Figure 2.1 (shown as dashed lines). Two effects, dephasing and thermal smearing, wash out fluctuations and cause the conductance to approach e^2/h . These effects are discussed in the next two sections. The experimental technique is described in Sec. 2.5.5.

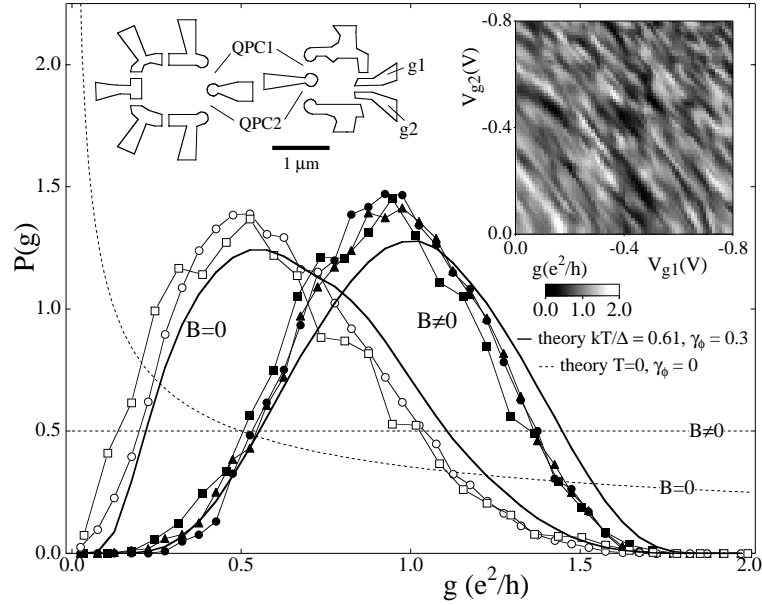


Figure 2.2: Conductance probability distributions $P(g)$ for $B = 0$ (open circles), 40 mT (filled circles) and 60 mT (filled triangles) for the $0.5 \mu\text{m}^2$ device at 100 mK, and for $B = 0$ (open squares) and 25 mT (filled squares) for the $1.0 \mu\text{m}^2$ device at 45 mK, along with the theoretical distributions for $kT/\Delta = 0.61$, $\gamma_\phi = 0.3$ (solid curves) and $T = 0$, $\gamma_\phi = 0$ (dashed curves). Theoretical distributions for $T = 0$, $\gamma_\phi = 0.3$ are shown in Figure 2.6(a). Upper left inset: Pattern of gates defining each quantum dot. Upper right inset: Conductance through $0.5 \mu\text{m}^2$ dot as a function of voltages on shape-distorting gates $g1$ and $g2$.

2.5.3 Dephasing and RMT

Dephasing, or the loss of quantum coherence, limits the time over which backscattered electrons may contribute to interference. To incorporate dephasing into random matrix theories, a fictitious voltage probe, or “ ϕ -lead”, supporting γ_ϕ modes is appended to the dot [Buttiker86a]. The number of phase-breaking modes, γ_ϕ , is related to the characteristic phase coherence time τ_ϕ by:

$$\gamma_\phi = \frac{2\pi\hbar}{(\tau_\phi\Delta)} \quad (2.7)$$

where

$$\Delta = \frac{2\pi\hbar^2}{m^*A_{dot}} \quad (2.8)$$

is the spin-degenerate mean level spacing.

The scattering matrix S is expanded to include the fictitious voltage lead [Baranger95,

Brouwer95a]. The RMT for this three-lead dot (two real leads plus the ϕ -lead) then yields a suppressed weak localization correction [Baranger94b],

$$\delta g \simeq \frac{e^2}{h} \frac{N}{2N + \gamma_\varphi} \quad N \geq 2 \quad (2.9)$$

that models the effect of dephasing. The accuracy of Equation 2.9 improves as N becomes larger, and it is a useful expression for $N \geq 2$. Note that γ_φ is proportional to dot area, so a larger dot will exhibit a smaller δg for a given τ_φ .

The variance of g , including γ_φ can be calculated using this technique as

$$\text{var}(g) \simeq \frac{N^2}{(\sqrt{4N^2 - 1} + \gamma_\varphi)^2} \quad N \geq 2, \beta = 2 \quad (2.10)$$

A recent improvement to the voltage-probe model that accounts for the spatially distributed nature of the dephasing process considers the limit of a voltage lead supporting an infinite number of modes, each with vanishing transmission, allowing a continuous value for the dimensionless dephasing rate γ_φ [Brouwer97a]. This effectively distributes the phase breaking throughout the dot rather than concentrating it at the location of a single lead.

The analytic expression for δg in this case is as follows [Brouwer96]:

$$\begin{aligned} \delta g = e^2/h & (1 - 2((-12(e^{\gamma_\varphi} - 1) + (38e^{\gamma_\varphi} - 26)\gamma_\varphi + 4(e^{\gamma_\varphi} - 7)\gamma_\varphi^2 - 3(e^{\gamma_\varphi} + 3)\gamma_\varphi^3 + \\ & (e^{\gamma_\varphi} - 1)\gamma_\varphi^4)/e^{\gamma_\varphi} + \gamma_\varphi^2(\gamma_\varphi + 4)(12(e^{\gamma_\varphi} - 1) - 6(e^{\gamma_\varphi} + 1)\gamma_\varphi + \\ & (e^{\gamma_\varphi} - 1)\gamma_\varphi^2) \text{ExpInt}(-\gamma_\varphi))/24\gamma_\varphi^2) \end{aligned} \quad (2.11)$$

Where the function $\text{ExpInt}(x)$ is defined by:

$$\text{ExpInt}(x) = \int_x^\infty \frac{e^{-t}}{t} dt$$

Fortunately Equation 2.11 can be approximated by:

$$\delta g \simeq \frac{e^2}{h} \frac{1}{2N + 1 + \gamma_\varphi} \quad \text{for all } N \quad (2.12)$$

At $N = 1$ the above approximation for $\delta g(\gamma_\varphi)$ agrees with the theoretical expression found in [Brouwer97a] to within $0.015 e^2/h$.

We note here that both the ϕ -lead model and its distributed extension [Brouwer97a] ignore the effects of Coulomb charging on δg , which may be important particularly at $N=1$ [Furusaki95a, Aleiner96]. The consistency between measured values of using different methods and dot sizes suggests that any field-dependent charging effects are probably not corrupting the present measurement significantly. Some recent theoretical results will be reviewed in Sec. 3.2.2.

The distributions of the conductance fluctuations have also been calculated by Brouwer using the distributed ϕ -lead model. $N = 1$ distributions for $\gamma_\varphi = 1$ are shown in Figure 2.3, along with the $\gamma_\varphi = 0$ curves. The effect of dephasing is to make $P(g)$ narrower and roughly gaussian, *and to reduce the difference in mean conductance upon breaking time reversal symmetry*, $\delta g = \langle g \rangle_{\beta=2} - \langle g \rangle_{\beta=1}$.

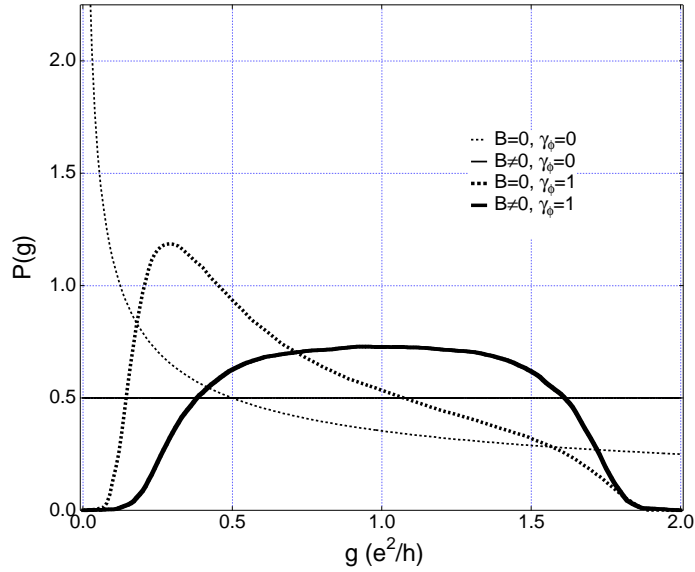


Figure 2.3: Theoretical conductance distributions for $N = 1$, $T = 0$, and dephasing rate $\gamma_\varphi = 1$ and $\gamma_\varphi = 0$.

2.5.4 Thermal Smearing

The above results are for zero temperature, i.e. perfectly monochromatic electrons. In most situations, carriers contributing to transport are spread out in energy according to the Fermi function $f(E)$. Distributions which include both dephasing thermal smearing effects are calculated for the first time here.

The dot cavity, even when open, has a characteristic energy scale of order Δ – such that when the energy (and correspondingly the wavelength) is shifted by this scale, the interference pattern can change. If the carrier energy distribution extends past this resonance width of the cavity, conductance fluctuations begin to smear out. If the electrons are Fermi distributed this is known as thermal smearing.

The net conductance is a weighted average of all conductances at all participating energies. For an energy distribution $f(E)$ the conductance through the device is:

$$g = - \int f'(E)g(E)dE \quad (2.13)$$

Since the above equation is linear in g , conductance averages and specifically δg are not affected by temperature. This fact is precisely why weak localization is particularly useful for measuring dephasing: δg depends on temperature *only* through γ_φ .

Higher moments and full distributions $P(g)$ depend on temperature both implicitly through dephasing and explicitly through thermal averaging. The combined effects of dephasing and thermal smearing must in general be evaluated numerically, which we do as follows. Samples of an averaged distribution are generated by summing independent samples x_i

$$y = \sum_i w_i(T)x_i \quad (2.14)$$

The x_i may be drawn from a known distribution $P(x, \gamma_\varphi)$ [Brouwer97a], and weighted by the derivative of the Fermi function:

$$w_i = \tilde{\Delta} f'([i + \delta]\tilde{\Delta}) \quad (2.15)$$

$$f'(E) = \frac{d}{dE}(1 + e^{E/kT})^{-1} \quad (2.16)$$

δ is a binning offset, and $\tilde{\Delta}$ is the cavity resonance width, itself dependent on γ_φ as described below. By sampling over ensembles of x values, a distribution $P(y)$ is obtained (the result is insensitive to the choice of δ for sufficiently large T). Note that neither fluctuations in level spacing nor fluctuations in the coupling between the levels and modes in the leads are included in this simple model.

The distributions for $N = 1$, $kT = 0.6\Delta$, and in the absence of dephasing are shown in Figure 2.4. The curves are clearly evolving towards a Gaussian. Indeed the well known Central Limit Theorem states that the averaging of a large number of samples from any

starting distribution will converge to a Gaussian distribution.

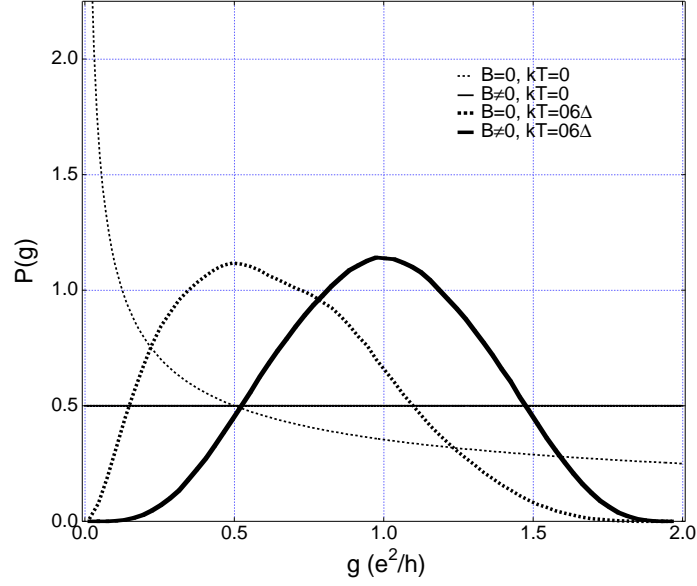


Figure 2.4: Theoretical conductance distributions for $N = 1$, $kT = 0.6\Delta$, and no dephasing.

As dephasing and thermal averaging conspire to make $P(g)$ nearly gaussian, $P(g)$ can be characterized by its mean and variance. The mean conductance $\langle g \rangle$ (an average quantity) is not affected by thermal averaging. The variance however is reduced both by dephasing and thermal smearing. The variance is well approximated by the $N = 1$ case interpolation formula:

$$\text{var}(x) = \frac{1}{(a + b\gamma_\varphi)^2} \quad (2.17)$$

where $a = \sqrt{3}$ ($\sqrt{45/16}$) and $b = 1$ ($\sqrt{1/3}$) for $\beta = 2$ (1) [Baranger95]. By applying equation 2.14 to the variance we see that

$$\text{var}(y) = \sum_i w_i^2 \text{var}(x) \quad (2.18)$$

At temperatures exceeding the level broadening $\tilde{\Delta}$ this sum can be well approximated by an integral,

$$\text{var}(y) = \tilde{\Delta} \left[\int_{-\infty}^{\infty} [f'(\epsilon)]^2 d\epsilon \right] \text{var}(x) = \frac{\tilde{\Delta}}{6kT} \text{var}(x). \quad (2.19)$$

The integral form differs from the sum by less than 1% for $kT \geq 0.6\tilde{\Delta}$. For experimental data studied here, this condition is satisfied, and Equation 2.19 is applicable at all measured temperatures.

To compare the experimental distributions to theory it is necessary to consider the dephasing rate: $P(g)$ depends on γ_φ through its effect on $\tilde{\Delta}$. Values for γ_φ are measured from the weak localization correction to the average conductivity, $\delta g = \langle g \rangle_{\beta=2} - \langle g \rangle_{\beta=1}$ using the results of Ref. [Brouwer97a], as shown in Figure 2.5(b). The values for $\gamma_\varphi(T)$ for this device agree well with other data which will be presented in Chapter 3.

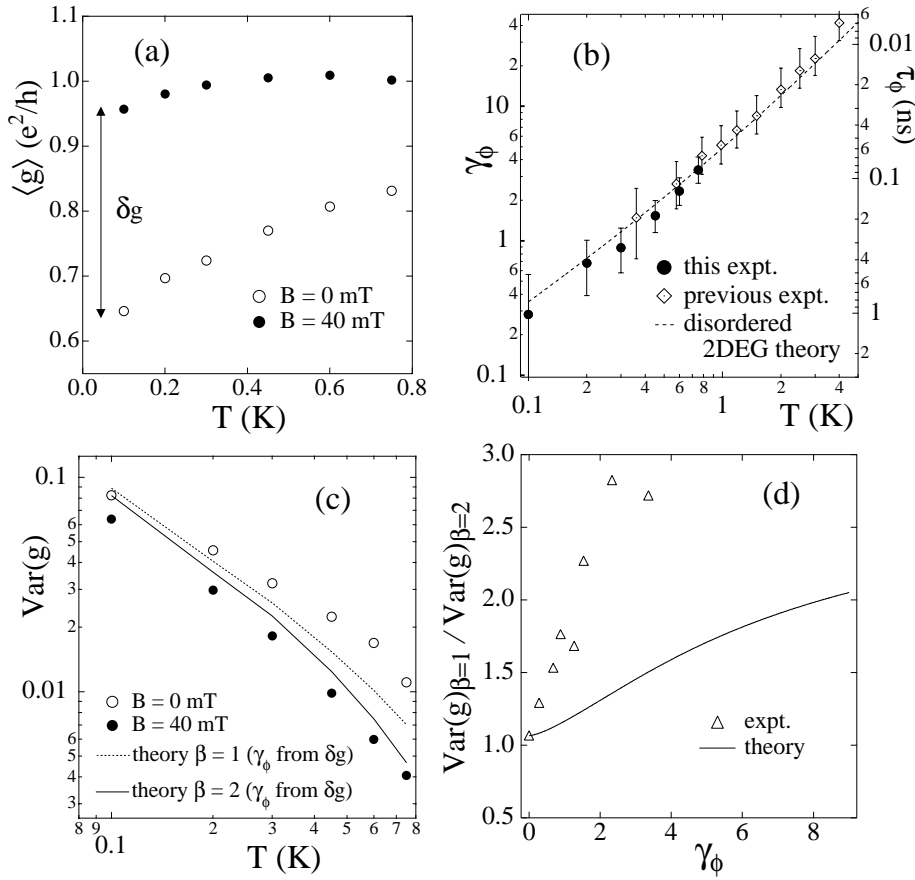


Figure 2.5: (a) Average conductance $\langle g \rangle$ as a function of temperature T for $B = 0$ and 40 mT for $0.5 \mu\text{m}^2$ dot. (b) Normalized dephasing rate γ_φ and dephasing time τ_φ determined from $\delta g(T)$ for the $0.5 \mu\text{m}^2$ dot. Note agreement with previously measured $\gamma_\varphi(T)$ in a $0.4 \mu\text{m}^2$ dot [Huibers98a]. (c) Variance of conductance for $B = 0$ and $B = 40$ mT, corresponding to expected variance for $\beta = 1$ (dashed) and $\beta = 2$ (solid) including thermal smearing and dephasing effects (see text). (d) Variance ratio $\text{Var } g_{\beta=1} / \text{Var } g_{\beta=2}$ as a function of dephasing rate γ_φ .

The re-sampling thermal averaging procedure described above takes energy intervals of size $\tilde{\Delta}$ to be statistically independent. Dephasing however results in level broadening by an amount proportional to the dephasing rate, which can be taken into account by defining the level broadening to be:

$$\tilde{\Delta} = \Delta (1 + \gamma_{\varphi}/2) \quad N = 1 \quad (2.20)$$

Inserting this definition into Equation 2.19 reproduces a number of previously obtained results for thermal $\text{var}(g)$ in various limits: ($\gamma_{\varphi} \ll 1$, $T \gg \Delta$) and ($\gamma_{\varphi} \gg 1$, $T \gg \Delta$) [Efetov95], as will be seen in Sec. 2.6.5. The measured variances of the conductance distributions for $\beta = 1$ and $\beta = 2$ as a function of temperature are compared to our thermal averaging model in Figure 2.5(c). The two are in good overall agreement, however, the ratio of variances, $\text{Var } g_{\beta=1} / \text{Var } g_{\beta=2}$ show significant disagreement between experiment and theory which remains unexplained. In particular, the experimental ratio is considerably larger than predicted, as seen in Figure 2.5(d). This ratio is an interesting quantity because, like δg , it does not suffer thermal averaging within the model considered here. Despite the disagreement in the ratio of variances, the RMT results for $P(g)$ are generally in very good agreement with experiment across a broad range of temperatures, as seen in Figure 2.6.

2.5.5 Experimental technique

The measurements presented in Figures 2.2, 2.5, and 2.6 were taken on two lateral quantum dots with areas $0.5 \mu\text{m}^2$ ($\Delta = 14 \mu\text{eV}$, device C14 in Appendix B) and $1.0 \mu\text{m}^2$ ($\Delta = 7.1 \mu\text{eV}$, device C79 in Appendix B). The devices (see Figure 2.2 inset) are defined using Cr/Au depletion gates 90 nm above a two-dimensional electron gas (2DEG) formed at a GaAs/Al_{0.3}Ga_{0.7}As heterointerface. Multiple gates on each device allowed independent control of the two point-contact leads as well as dot shape. Sheet density $n = 2 \times 10^{11} \text{ cm}^{-2}$ and mobility $\mu = 1.4 \times 10^5 \text{ cm}^2/\text{Vs}$ give an elastic mean free path of $\sim 1.0 \mu\text{m}$, comparable to device dimensions, and transport within the dots is roughly ballistic. The dots were measured in a dilution refrigerator over a range of electron temperatures from 45 mK to 750 mK using 4-wire lock-in techniques at 43 Hz (13 Hz) and less than 7 μV (2 μV) bias voltage for the $0.5 \mu\text{m}^2$ ($1.0 \mu\text{m}^2$) device. See Appendix D for details. The electron temperature was determined from a fit to the average Coulomb blockade peak width, as described in [Folk96].

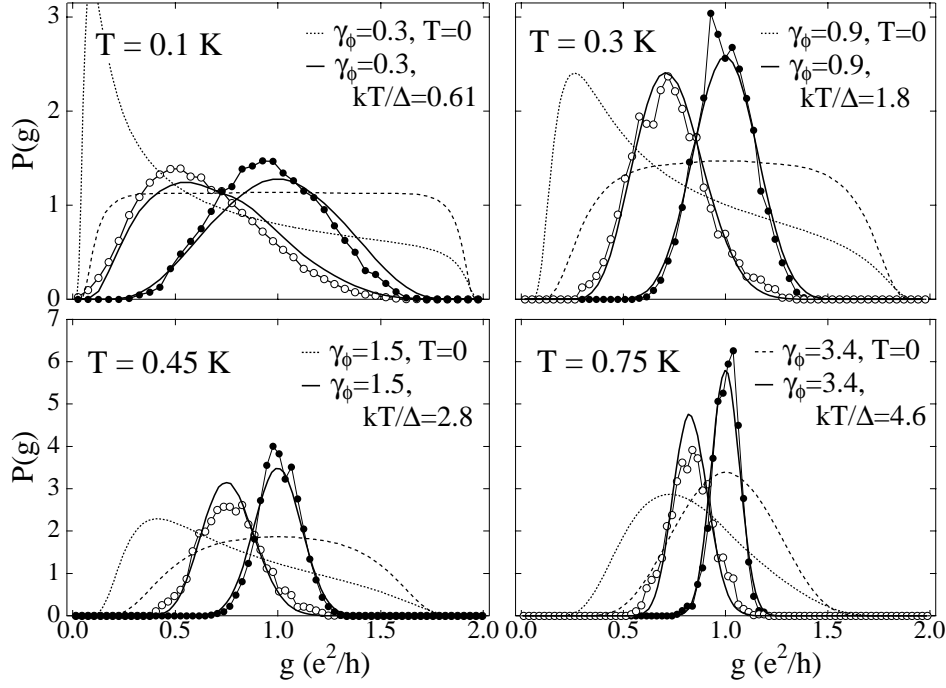


Figure 2.6: Measured conductance distributions for $B = 0$ (open circles) and 40 mT (closed circles) for $0.5 \mu\text{m}^2$ dot at four temperatures. Curves show theoretical $\beta = 1$ (dotted) and $\beta = 2$ (dashed) distributions for $T = 0$ and for measurement temperatures (solid). $T = 0$ distributions are determined using the method of Ref. [Brouwer97a]. Thermal distributions are calculated according to the sampling procedure described in the text.

To date, experimental measurements of significantly nongaussian distributions have not been reported, first because it is difficult to generate large ensembles of statistically identical devices, and second because dephasing, which acts roughly as extra modes coupling the dot to the environment, leads to nearly gaussian distributions [Brouwer97a, Chan95, McCann97]. To see the nongaussian distributions, dephasing rates and temperatures comparable to the quantum level spacing are required. We solve the first problem, of obtaining large ensembles, by using electrostatic shape distortion of gate-defined quantum dots in a GaAs/AlGaAs heterostructure [Chan95].

The experimental conductance probability distributions $P(g)$ for $|B| \ll \phi_o/A_{dot}$ ($\beta = 1$) and $|B| \gg \phi_o/A_{dot}$ ($\beta = 2$) shown in Figure 2.2 are histograms containing ~ 1000 independent samples measured at fixed B for slightly different dot shapes, as controlled by voltages applied to the gates labeled g_1 and g_2 , as well as the gate between the two point

contacts. A two-dimensional slice of this 3-D sampling space is shown in the inset of Figure 2.2. In order to precisely maintain single-mode leads throughout the measurement, voltages on the gates adjacent to the point contacts are slightly trimmed for each shape configuration after first characterizing the influence of all gates on the point contact conductances. The asymmetry of the $\beta = 1$ distribution is clearly visible in contrast to Ref. [Chan95] which found gaussian distributions due to thermal averaging and dephasing. Some asymmetry in the conductance distribution has been observed in Ref. [Lee97] though without quantitative comparison to theory. The average conductance at $\beta = 2$ is $\sim e^2/h$ as expected from RMT, with a small (4%) deviation at the lowest temperatures possibly due to imperfect quantum point contacts enhanced by charging effects [Furusaki95a, Aleiner97]. Once time-reversal symmetry is broken, the distribution becomes insensitive to magnetic field for the relatively small fields used in the experiment (the cyclotron radius is always larger than the dot size). For instance, though $g(B)$ are uncorrelated at $B = 40$ mT and 60 mT, $P(g)$ at these magnetic field values are nearly identical (ϕ_o/A_{dot} is ~ 8 mT for the $0.5 \mu\text{m}^2$ device).

2.5.6 Significance of Distribution Results

These transport measurements demonstrate the success of random matrix theory (RMT) and non-interacting theory in describing the statistics of quantum transport in this mesoscopic electronic system. This is surprising considering that electron-electron interactions are not accounted for in the theory and are sizable compared to other energy scales in these systems.

That good agreement is found between the experimental distributions and the RMT predictions over a broad range of temperatures is also surprising since we are investigating the case of single-mode leads, $N = 1$. This is the transition between open and closed dots; for any lower conductance to the dot, electron-electron interactions in the form of Coulomb blockade dominate transport, leading to dramatic departures from a non-interacting picture [Kouwenhoven97]. Some charging has been observed in small dots, although the effect is small (see Sec. 3.4). Overall, measurements performed for $N = 1$ and $N = 2$ on the same devices are very consistent, as will be seen in Chapters 3 and 5.

One should note here that the success of non-interacting theory when describing real metallic or semiconductor structures seems to depend on the quantity being measured. For instance, the mean and variance of mesoscopic conductance fluctuations in open quantum dots and disordered wires appear to be in good agreement with random matrix theory

[Beenakker97] and sigma model calculations [Efetov95] once temperature and dephasing effects are included, as shown in this chapter, whereas the distribution of energies needed to add subsequent electrons to a closed dot does not appear distributed according to the famous Wigner-Dyson law, a basic result of RMT [Sivan96, Simmel97, Patel98a].

In sum, the distribution measurements constitute a stringent test of statistical theories of mesoscopic conductance. Unlike many other experiments, there are no adjustable parameters in these measurements.

2.5.7 Conductance Derivatives

Distributions of parametric derivatives of conductance were also investigated with respect to magnetic field dg/dB and gate voltage, dg/dV_g . These quantities are of considerable interest as they are the open-system analogs of the well-studied “level velocities” dE/dX of the energy levels in closed quantum chaotic systems [Altshuler95]. Distributions of parametric derivatives of conductance have recently been investigated theoretically using a random-phase-approximation “charged fluid” model [Buttiker93], which gave interesting nongaussian distributions for both $\beta = 1$ and $\beta = 2$ [Brouwer97b]. Here we investigate both $P(dg/dB)$ and $P(dg/dV_g)$ in single-mode dots, and find that both distributions are well described by gaussians due to dephasing and thermal averaging. We focus on $P(dg/dV_g)$, shown in Figure 2.7 for zero and nonzero magnetic field, at $T = 0.1$ K and 0.2 K. Thermal averaging dominates the width of the distribution. From this data $var(g) \propto T^{-1.75}$. Distributions of dg/dB are also roughly gaussian, with variances of 9.65 mT^{-2} at $T = 0.1$ K and 0.939 mT^{-2} at $T = 0.5$ K. To observe deviations from gaussian distributions of parametric derivatives, lower temperatures than those needed to see nongaussian $P(g)$ are required.

2.6 Supersymmetry Theory

Another useful theory of quantum dot transport is based on supersymmetric techniques [Efetov97]. This theory can predict of many aspects of transport through quantum dots and provides an independent confirmation of the RMT results.

2.6.1 Conductance autocorrelation

The autocorrelation of the conductance through a mesoscopic device is a metric of the sensitivity of the wave interference in the device to environmental and system parameters

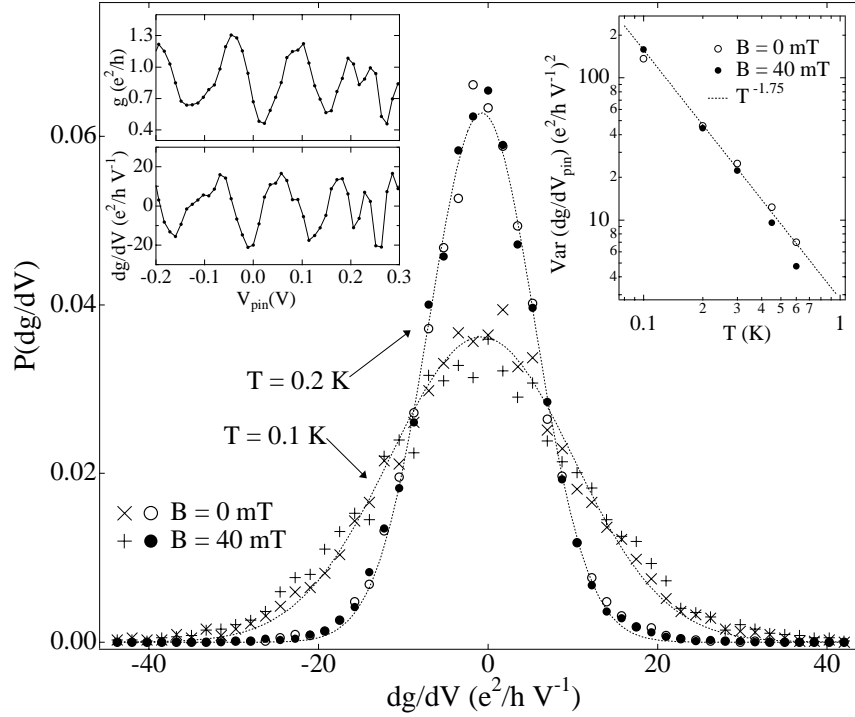


Figure 2.7: Conductance derivatives $P(dg/dV_g)$ at $B = 0$ and 40 mT for $T = 0.1$ K and $T = 0.2$ K. Upper right inset shows $\text{Var}(dg/dV_g)$ as a function of temperature, which exhibits a $T^{-1.75}$ dependence. Upper left inset shows fluctuating conductance g and derivative $P(dg/dV_g)$ as function of gate voltage.

(energy and magnetic field), mitigated by temperature, dephasing, and degree of openness.

$$C(\Delta X) = \langle \delta g(X + \Delta X) \delta g(X) \rangle \quad (2.21)$$

where $\delta g(X) = g(X) - \langle g \rangle$. Efetov provides the following correlation function for a quantum dot connected to source and drain reservoirs with N channel leads:

$$C(B, E) = \frac{1}{4} \frac{1}{\left(\left(\frac{B}{B_c} \right)^2 + \frac{\gamma_\varphi}{2N} + 1 \right)^2 + \left(\frac{\pi E}{N\Delta} \right)^2} \quad (2.22)$$

It is clear from Equation (2.22) that the parametric dependence on E and B is correlated: $C(B, E) \neq C(B)C(E)$. This makes intuitive sense: short quantum trajectories produce short range correlations in E , and also in B due to small swept areas; the same argument hold for long trajectories.

At zero temperature $T = 0$ and for no decoherence $\gamma_\varphi = 0$ the magnetic field autocorrelation function is Lorentzian-squared:

$$C(B) = \frac{1}{4} \frac{1}{\left(\left(\frac{B}{B_c}\right)^2 + 1\right)^2} \quad (2.23)$$

The autocorrelation operation in real space is the amplitude squared (power) operation in frequency space, so that the Fourier transform of the above $C(B)$ yield the power spectral density of magnetoconductance fluctuations:

$$S(f_B) = S(0)(1 + 2\pi B_c |f_B|) e^{-2\pi B_c |f_B|} \quad (2.24)$$

which is the same result obtained classically. For energy dependence at $T = 0$ and $\gamma_\varphi = 0$ we have a Lorentzian autocorrelation:

$$C(E) = \frac{1}{4} \frac{1}{1 + \left(\frac{\pi E}{N\Delta}\right)^2} \quad (2.25)$$

$$S(f_E) = S(0) e^{-2\pi E_c |f_E|} \quad (2.26)$$

2.6.2 Temperature

If we look at transport through a quantum system at a finite temperature, electrons are Fermi distributed and the measured conductance is a convolution of the zero temperature conductance and the Fermi envelope (a few kT in width), which is simply $-f'(E, T)$, the energy derivative of the Fermi function.

$$g(X, E, T) = -f'(E) * g(X, E) = - \int f'(\varepsilon) g(X, E - \varepsilon) d\varepsilon \quad (2.27)$$

For correlations of conductance we then have:

$$\begin{aligned} C(X, E, T) &= \int \int f'(\epsilon_1) g(X, \varepsilon - \epsilon_1) d\epsilon_1 \int f'(\epsilon_2) g(X, \varepsilon + E - \epsilon_2) d\epsilon_2 d\varepsilon \\ &= \int \int f'(\epsilon_1) f'(\epsilon_T) C(X, E + \epsilon_1 - \epsilon_2) d\epsilon_1 d\epsilon_2 \end{aligned} \quad (2.28)$$

2.6.3 High Temperature C(E)

At very high temperatures, energy correlation is determined by the thermal envelope, since $C(X, E)$ is nearly a delta-function in energy on a thermal scale, and the expression in Eq. (2.28) becomes for limit of kT much that correlation energy E_c :

$$\begin{aligned} C(X, E, T) &= \int \int f'(\epsilon_1) f'(\epsilon_2) \delta(E + \epsilon_1 - \epsilon_2) d\epsilon_1 d\epsilon_2 \int C(X, \epsilon, T) d\epsilon \\ &= C(E, T) \int C(X, \epsilon, T) d\epsilon \end{aligned} \quad (2.29)$$

where

$$\begin{aligned} C(E, T) &= \int f'(\epsilon) f'(E - \epsilon) d\epsilon \\ &= \frac{e^{\frac{E}{kT}} \left(2 \left(-1 + e^{\frac{E}{kT}} \right) + \left(1 + e^{\frac{E}{kT}} \right) \log(1 + e^{-\frac{E}{kT}}) - \left(1 + e^{\frac{E}{kT}} \right) \log(1 + e^{\frac{E}{kT}}) \right)}{kT \left(1 - e^{\frac{E}{kT}} \right)^3} \end{aligned}$$

$C(E, T)$ is a function nearly identical in shape to $f'(E)$ except about 1.5 times wider. Below the two are plotted in energy units of kT .

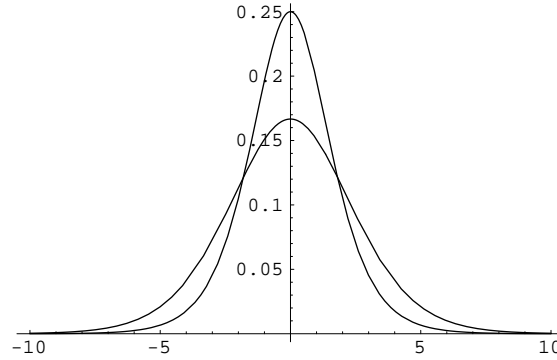


Figure 2.8: Thermal envelopes $f'(E)$ and $C(E, T)$. $f'(E)$ is the narrower one.

Some properties of $C(E, T)$ are:

$$C(0, T) = \frac{1}{6kT} \quad \text{and} \quad \int C(E, T) dE = 1$$

The Fourier transform of $C(E, T)$ is the power spectral density of energy conductance fluctuations in the high temperature limit—this does not have a simple closed-form expression and we plot the PSD calculated numerically below. Note that Fourier transform pair scale

inversely with the dependent variable: the PSD below will contract linearly with increasing temperature.

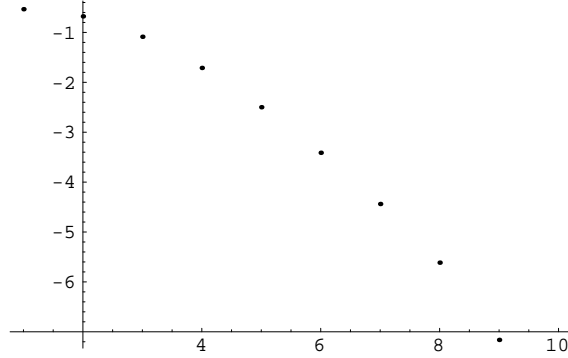


Figure 2.9: Energy conductance power spectrum at high T.

2.6.4 High Temperature $C(B)$

To compute $C(B)$ for high temperature, we perform the integral in Equation (2.29), setting $E = 0$, giving:

$$C(B) = \frac{N\Delta}{24kT} \frac{1}{(\frac{B}{B_c})^2 + 1}$$

and

$$S(f_B) = S(0)e^{-2\pi B_c |f_B|}$$

The frequency dependence of $S(f_B)$ does not change directly with temperature, but only through dephasing via $B_c(\tau_\varphi) = \frac{\phi_0}{A(\tau_{\text{total}})}$ where $\tau_{\text{total}}^{-1} = \tau_{\text{esc}}^{-1} + \tau_\varphi^{-1}$.

2.6.5 Equivalence of Supersymmetry Theory and RMT

Supersymmetry theory and Random Matrix Theory are equivalent in the limit of large N , including the thermal limit of $kT \gg \Delta$ and the presence of arbitrary dephasing.

To include dephasing in the supersymmetry results, we simply retain the $\frac{\gamma_\varphi}{2N}$ term in Equation 2.22, and propagate it through the temperature integral.

To make the comparison with RMT, we generalize the formula for $\tilde{\Delta}$ to N -mode leads (formerly we considered only the $N = 1$ case):

$$\tilde{\Delta} = \Delta \frac{2N + \gamma_\varphi}{2}$$

and make the appropriate substitution.

Variance results from both theories including temperature and dephasing are noted with *'s in the table below, which also serves to summarize many of the formulae presented in this chapter. Encouragingly, the results, derived using very different theoretical approaches, are in agreement.

theory	applies to	
Basic RMT	$\beta = 1, \gamma_\varphi = 0$	$var(g) = \frac{4N(N+1)^2}{(2N+1)^2(2N+3)}$
	$\beta = 2, \gamma_\varphi = 0$	$var(g) = \frac{N^2}{4N^2-1}$
ϕ -lead	$N \geq 2, \beta = 2$	$var(g) \simeq \frac{N^2}{(\sqrt{4N^2-1} + \gamma_\varphi)^2}$
	$\gamma_\varphi \gg 1, \beta = 2$	$var(g) \rightarrow \left(\frac{N}{\gamma_\varphi}\right)^2$
General Thermal	$kT \geq 0.6\tilde{\Delta}$, any N	$var(y) = \frac{\Delta}{6kT} var(x)$ $\tilde{\Delta} = \Delta \frac{2N + \gamma_\varphi}{2}$
Thermal RMT	$kT \geq 0.6\tilde{\Delta}$	$var(g) \simeq \frac{\Delta}{6kT} \frac{2N + \gamma_\varphi}{2} \frac{N^2}{(2N + \gamma_\varphi)^2}$ $\simeq \frac{\Delta}{6kT} \frac{1}{2} \frac{N^2}{2N + \gamma_\varphi}$ *
Supersymmetry	$\frac{2\pi^2 kT}{N\Delta} \ll 1 + Y^2$ $\frac{2\pi^2 kT}{N\Delta} \gg 1 + Y^2$	$C_{\text{lowT}}(\phi) = \frac{1}{4} \frac{1}{(Y^2 + 1)^2}$ $C_{\text{highT}}(\phi) = \frac{N\Delta}{24kT} \frac{1}{Y^2 + 1}$ $Y^2 = (\phi/\phi_c)^2 + \frac{\gamma_\varphi}{2N}$ $\phi_c = \frac{\phi_0}{2\pi} \sqrt{\frac{\pi N \Delta}{2E_c}}, \phi_0 = 4.14 \text{mT}/\mu\text{m}^2$ (no dephasing) $E_c = \pi^2 D_0/L^2$, diffusive $E_c = \tau_{\text{dwell}}/\tau_{\text{cross}}$, ballistic
Supersymmetry	$4\pi^2 kT \ll (2N + \gamma_\varphi)\Delta$ $\gamma_\varphi \gg 1$ $4\pi^2 kT \gg (2N + \gamma_\varphi)\Delta$	$var(g) = C(0)$ $var(g) = \frac{N^2}{(\gamma_\varphi + 2N)^2}$ $var(g) \rightarrow \left(\frac{N}{\gamma_\varphi}\right)^2$ $var(g) = \frac{N\Delta}{6kT} \frac{1}{2} \frac{N}{\gamma_\varphi + 2N}$ *

Table 2.2: Theoretical $var(g)$ results summary.

Chapter 3

Dephasing Measurements in Quantum Dots

This chapter focuses on measurements of the loss of phase coherence (dephasing) in quantum dots. This is studied principally by measuring the weak localization amplitude, but also using other techniques. The experiments employ devices covering a large parameter space.

Experiments were done in two phases and will be described here in that order. The first “high temperature” measurements were performed in a Helium-3 system over a temperature range of 335 mK to 4K. The second set of “low temperature” experiments were done in a dilution refrigerator over a temperature range of 45 mK (the electronic base temperature of the cryostat) to 800 mK.

The high temperature data emphasizes average weak localization curves as a primary result, and also compares several different techniques for determining τ_ϕ . The low temperature experiments focus on obtaining good statistical data for the average and variance of the conductance fluctuations, typically at zero field and at multiple values of non-zero field at which time-reversal symmetry is broken.

Results between these two experiments were highly consistent, including devices fabricated on 2D electron gases from two different sources (see appendix B for device descriptions), giving confidence in the data. Figure 3.11 at the end of the chapter combines the results and give a composite view of τ_ϕ as a function of temperature.

The low temperature experiments were extended to study the effects of radiation, which is the topic of Chapter 5.

3.1 High Temperature Dephasing Measurements

3.1.1 Background

The weak localization technique is used here as our primary technique for determining $\tau_\varphi(T)$, and is similar to standard methods used in diffusive 1D and 2D samples. This method was applied to quantum dots for the first time in these experiments, having only become possible due to the theoretical developments [Baranger94a, Brouwer97a] based on random matrix theory (RMT) [Beenakker97].

3.1.2 Related Experimental Work

Most previous studies of dephasing in mesoscopic systems have focused on disordered 1D and 2D conductors, where the dimensional crossover for quantum corrections to transport and dephasing mechanisms occurs when the sample width exceeds the phase coherence length $l_\varphi = \sqrt{\tau_\varphi}$ and thermal length $l_T = \sqrt{D\hbar/kT}$, respectively (D is the diffusion constant) [Altshuler85, Imry94]. At low temperatures, electron-phonon scattering rates are small compared to electron-electron scattering rates [Mittal96] and two electron-electron scattering mechanisms dominate dephasing: a large-energy-transfer scattering mechanism, which causes dephasing with a rate $\tau_{ee}^{-1} \propto T^2$ [Zheng96, Giuliani82, Fukuyama83, Jungwirth96, Pines96] – in a 2D electron gas (2DEG) this rate is

$$\tau_{ee}^{-1} = \frac{\pi}{4} \frac{(kT)^2}{\hbar E_F} \ln \frac{E_F}{kT} \quad (3.1)$$

for $kT \ll E_F$ where E_F is the Fermi energy – and a small energy-transfer (Nyquist) scattering mechanism, which gives a rate $\tau_{\varphi N}^{-1} \propto T^{2/(4-d)}$ where d is the dimensionality of the system ($d = 1, 2$) [Altshuler85]. In a disordered 2DEG the Nyquist dephasing rate is

$$\tau_{\varphi N}^{-1} = \frac{kT}{2\pi\hbar} \frac{\lambda_F}{l_e} \ln \frac{\pi l_e}{\lambda_F} \quad (3.2)$$

where λ_F is the Fermi wavelength and l_e is the elastic mean free path. The total dephasing rate due to electron-electron scattering is approximately the sum of these rates, [Choi87, Kurdak92, Reulet95]:

$$\tau_\varphi^{-1} \simeq \tau_{\varphi N}^{-1} + \tau_{ee}^{-1} \quad (3.3)$$

Measurements of $\tau_\varphi(T)$ in disordered 2D and 1D semiconductors [Choi87, Kurdak92, Reulet95] and 1D metals [Echternach93, Lin86] based on weak localization find good agreement with these theoretical results down to ~ 0.1 K. In clean 2D systems ($l_e \geq l_\varphi$) the dephasing rate is expected to coincide with τ_{ee} from Equation 3.1, without the Nyquist contribution, which has been confirmed experimentally using high-mobility 2DEG samples [Yacoby94, Murphy95]. In isolated quantum dots (0D systems), a dephasing rate $\tau_\varphi^{-1} \sim T^2$ is expected for intermediate temperatures ($l_T > L$ but $kT \gg \Delta$, where Δ is the mean level spacing) with a rate comparable to Equation 3.1 for ballistic dots, $l_e > L$ [Sivan94a, Blanter96, Altshuler97]. To our knowledge, there has been no explicit theoretical discussion of τ_φ in open quantum dots despite previous experimental investigation [Clarke95, Bird95a]. Dephasing mechanisms are discussed in detail in Chapter 4.

3.1.3 Experiment

Here $\tau_\varphi(T)$ is measured in ballistic quantum dots with areas ranging from 0.4 to $4 \mu\text{m}^2$ and with single-mode point-contact leads. It is found that τ_φ is independent of dot area and, surprisingly, that $\tau_\varphi(T)$ is not proportional to T^{-2} but rather shows behavior similar to that seen in disordered 2D conductors, including both T^{-1} and T^{-2} contributions. These conclusions are checked with a comparison to $\tau_\varphi(T)$ measured three other ways in the same devices.

As discussed in the previous chapter, for irregularly-shaped quantum dots with two leads each supporting N channels (or lateral modes), RMT yields a zero-temperature average conductance $\langle g \rangle$ equal to the resistors-in-series value Ne^2/h at $B \neq 0$, but is reduced to $2N^2/(2N+1)e^2/h$ at $B = 0$ due to phase-coherent backscattering (or weak localization) [Baranger94b, Jalabert94]. Dephasing suppresses the difference, δg , by limiting the time over which backscattered electrons may contribute to interference.

Measurements on four quantum dots (Appendix B, devices I613, I75, I77, I74) with areas of $0.4 \mu\text{m}^2$ (two dots), $1.9 \mu\text{m}^2$ and $4.0 \mu\text{m}^2$ ($\Delta = 17.9, 3.8$, and $1.8 \mu\text{eV}$ respectively) are described. The dots are formed by gate depletion of a 2DEG located 160 nm below the surface of a GaAs/Al_{0.3}Ga_{0.7}As heterostructure with sheet density $n = 1.8 \times 10^{11} \text{ cm}^{-2}$, mobility $\mu = 1.0 \times 10^6 \text{ cm}^2 \text{ Vs}$, Fermi wavelength $\lambda_F = 60$ nm and Fermi energy $E_F = 6.4$ meV. The elastic mean free path measured with gates undepleted is $\sim 6 \mu\text{m}$, larger than all device sizes so that transport is ballistic within the dots. The dots were measured in a ^3He cryostat at temperatures ranging from 335 mK to 4 K using standard 4-wire lock-in techniques at 105

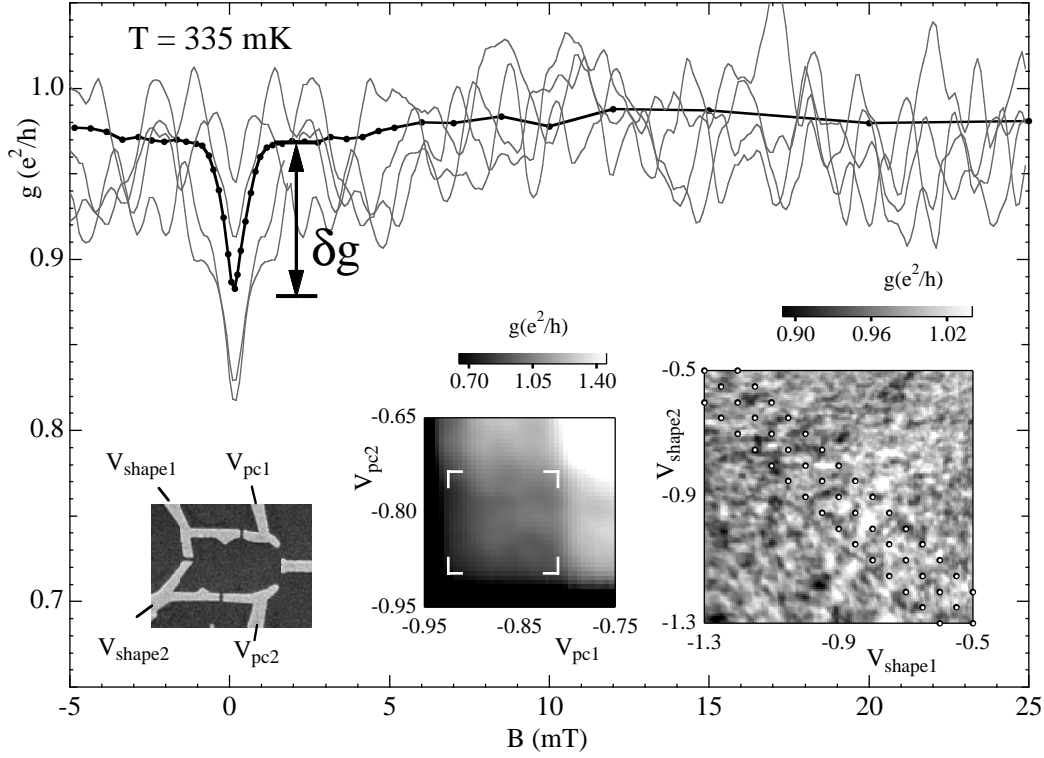


Figure 3.1: Shape-averaged magnetoconductance (black) and four unaveraged conductance curves (gray) for the $4.0 \mu\text{m}^2$ quantum dot (inset). Lower left inset: conductance as a function of V_{pc1} and V_{pc2} showing (bracketed) plateau with $N = 1$ channel in each point contact. Lower right inset: Conductance through dot as a function of V_{shape1} and V_{shape2} with circles marking the 47 points at which magnetoconductance was measured.

Hz with 0.5 nA bias current. This probe current was small enough not to affect transport due to heating— currents of 0.5 and 1 nA give identical results at base temperature (335 mK). At these temperatures, weak localization and UCF are comparable in magnitude, as seen in the gray traces of Figure 3.1. By averaging over gate-voltage-controlled shape distortions, UCF is averaged away leaving only the weak localization correction. The exact measurement procedure is illustrated in Figure 3.1. First, depletion gates V_{pc1} and V_{pc2} are swept in a raster to find the plateau with $N = 1$ channel in each lead (bracketed region lower left inset). While the leads are maintained at one channel each, the shape of the dot is distorted using V_{shape1} and V_{shape2} , creating an effective ensemble of dots. The 47 circled points on the conductance landscape in the lower right inset indicate the positions in $(V_{\text{shape1}} - V_{\text{shape2}})$ space of the samples used in the ensemble. Figure 3.1 shows $g(B)$ at

four of these 47 points, along with the average $\langle g(B) \rangle$ of all 47 points used to determine δg .

3.1.4 Weak Localization and Dephasing Times

Figure 3.2 shows δg at $N = 1$ as a function of temperature for the four devices. Using $\gamma_\varphi(\delta g)$ from Ref. [Brouwer97a], each point in Figure 3.2 is converted to γ_φ and then, using Equation 2.7, to τ_φ . The resulting $\tau_\varphi(T)$ is shown in Figure 3.3. While dots with different areas have different values of δg and γ_φ , τ_φ appears to be independent of area. The high temperature roll-off of τ_φ seen in Figure 3.3 for larger devices likely results from a breakdown of the model [Brouwer97a] when l_φ becomes of order L , so that nonergodic trajectories dominate coherent backscattering. The inequality $L > l_\varphi$ holds throughout the measured range of temperatures, however $L \sim l_T = v_f \hbar / kT$ at 2.2 K, 0.97 K and 0.69 K for the $0.4 \mu\text{m}^2$, $1.9 \mu\text{m}^2$ and $4.0 \mu\text{m}^2$ dots respectively. As seen in Figure 3.3, the temperature dependence of τ_φ for all four dots falls between $\tau_\varphi \propto T^{-2}$ and $\tau_\varphi \propto T^{-1}$. The data cannot be fit by τ_{ee} alone (dashed line in Figure 3.3) but are well fit by the sum of dephasing rates for *diffusive* 2D systems, Equations 3.1 and 3.2, (solid line in Figure 3.3) if we choose $l_e = 0.25 \mu\text{m}$, giving $\tau_\varphi^{-1}[\text{ns}^{-1}] = 10.9(T[\text{K}]) + 6.1(T[\text{K}])^2$. We do not know if the value of l_e corresponds to any physical length in the problem; certainly it is much shorter than the l_e of the unconfined electron gas.

We note that $\tau_\varphi(T)$ does not show a low- T saturation over the temperature range reported. As will be shown in Sec. 3.2, measurements down to an electron temperature of 45 mK show some saturation below 100 mK, and a $\tau_\varphi(T)$ consistent with the present data above 100 mK. As will be discussed in Chapter 5, direct application of microwave radiation (40 MHz to 25 GHz) to the sample has also been shown to cause a saturation in $\tau_\varphi(T)$ at higher temperatures but does not cause the Nyquist-like $\tau_\varphi(T)$ dependence observed here.

3.1.5 Other techniques to measure τ_ϕ

To check the results based on weak localization amplitude at $N = 1$ (which will be labeled $\delta g_{N=1}$ here), we compare to three other measurements of $\tau_\phi(T)$ in the same devices (figure 3.4). The first comparison is to $\tau_\phi(T)$ obtained from weak localization amplitude at $N = 2$ (labeled $\delta g_{N=2}$), measured as above, and using Equations 2.7 and 2.9 to convert from $\delta g_{N=2}$ to τ_ϕ . The $\delta g_{N=2}$ and $\delta g_{N=1}$ results are consistent within experimental error as shown in Figures 3.4(a) and 3.4(b) for the $0.4 \mu\text{m}^2$ and $4.0 \mu\text{m}^2$ dots.

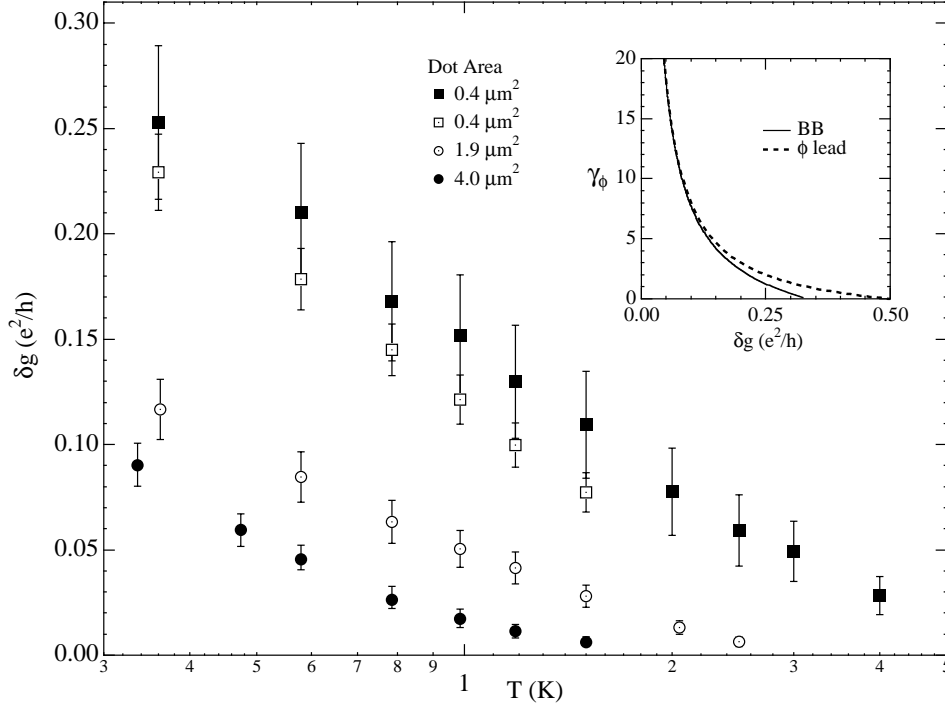


Figure 3.2: Shape-averaged weak localization amplitude δg vs. temperature T for the four measured devices. Error bars reflect uncertainty in δg as a result of conductance fluctuations remaining due to limited ensemble size. Inset: Theoretical phase breaking rate $\gamma_\phi(\delta g)$ using ϕ -lead model [Baranger94a] (Equation 2.7) and distributed voltage probe model (BB) [Brouwer97a].

A second comparison is to $\tau_\phi(T)$ extracted from power spectra of UCF, a method described previously in Ref. [Clarke95]. This method makes use of the fact that UCF measured as a function of B in open quantum dots has an exponential power spectrum [Efetov95],

$$S(f) = S(0)e^{-2\pi B_c f} \quad (3.4)$$

where f is magnetic frequency in cycles/mT. The characteristic magnetic field B_c depends on the dephasing rate:

$$(B_c/\varphi_0)^2 = K(2N + \gamma_\phi), \quad (3.5)$$

where K is a geometry-dependent constant and $\varphi_0 = h/e$ is the quantum of flux [Clarke95]. Figure 3.4(c) shows power spectra of $g(B)$ for the $4.0 \mu\text{m}^2$ dot, consistent with Equation 3.4 over three orders of magnitude. A two-parameter fit of Equation 3.4 to power spectra at each temperature gives a $B_c(T)$ which yields $\tau_\phi(T)$ via Equation 3.5, with K chosen as

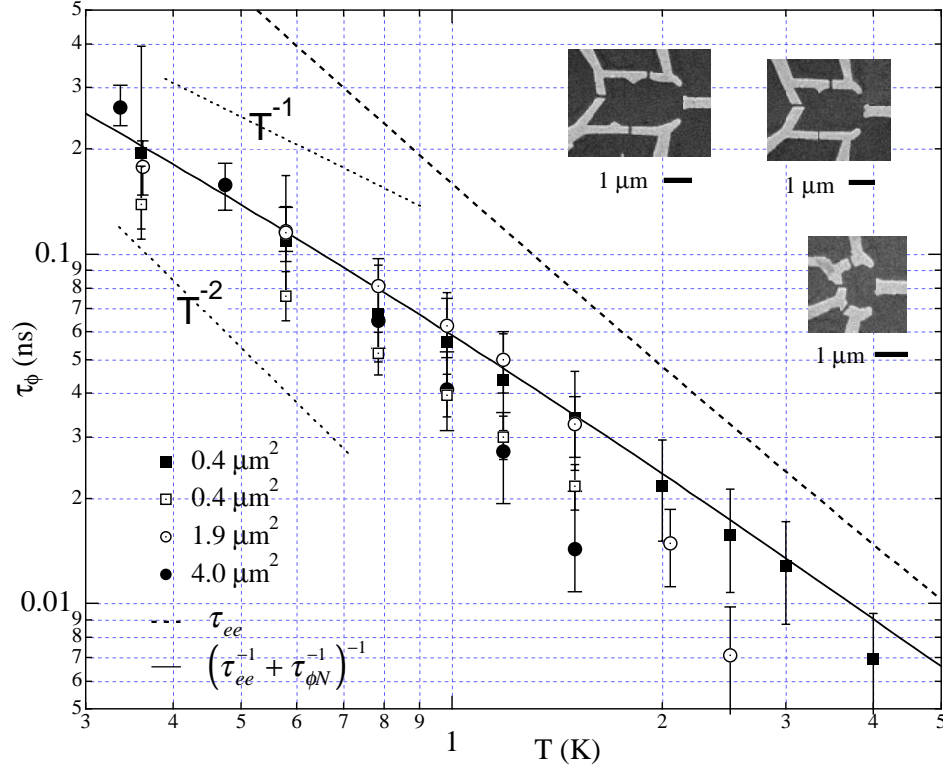


Figure 3.3: Phase coherence time τ_ϕ determined from $N = 1$ weak localization. τ_{ee} from Equation 3.1 (dashed), and $\tau_\phi^{-1} \simeq \tau_{\phi N}^{-1} + \tau_{ee}^{-1}$ for a 2D disordered system with $l_e = 0.25 \mu\text{m}$ (solid) are shown for comparison. Dotted lines indicate slopes corresponding to T^{-1} and T^{-2} , offset for clarity.

a best fit to the $\delta g_{N=1}$ data. Figure 3.4(d) compares $\tau_\phi(T)$ determined from UCF power spectra with that from $\delta g_{N=1}$, showing good agreement over the whole temperature range.

A final comparison is to $\tau_\phi(T)$ extracted from the width of the Lorentzian dip in average conductance around $B = 0$ [Baranger93a, Chan95]

$$\langle g(B) \rangle = \langle g(B) \rangle_{B \neq 0} - \frac{\delta g}{1 + (2B/B_c)^2}. \quad (3.6)$$

Figure 3.4(e) shows traces of shape-averaged $\langle g(B) \rangle$ for the $4.0 \mu\text{m}^2$ dot, along with two-parameter (δg and B_c) fits to Equation 3.6. Values for $\tau_\phi(T)$ in Figure 3.4(f) are extracted from $B_c(T)$ using Equation 3.5, with K chosen to give a best fit to the $\delta g_{N=1}$ results. It is noteworthy that several very different methods of determining $\tau_\phi(T)$ agree to within experimental error.

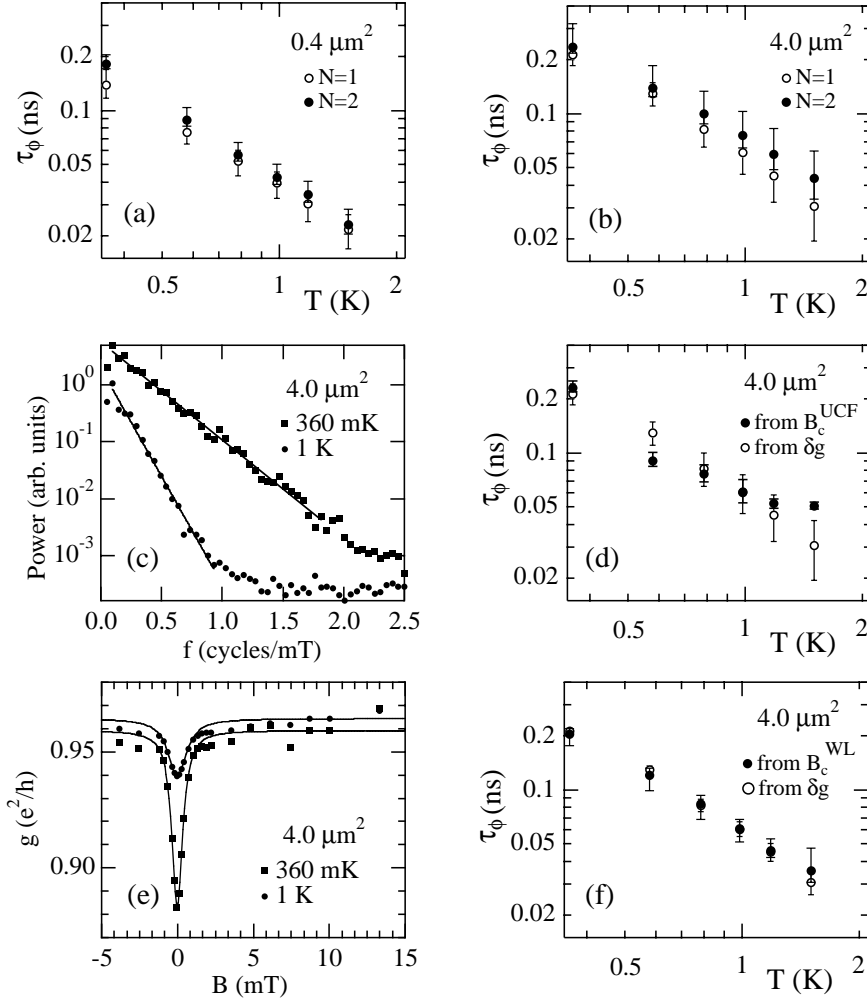


Figure 3.4: (a), (b) Comparison of τ_ϕ extracted from average $N = 1$ and $N = 2$ weak localization amplitude for $0.4 \mu\text{m}^2$ and $4.0 \mu\text{m}^2$ dots. (c) Fit of Eq. 3.4 to power spectral density for $N = 1$ conductance fluctuations and (d) comparison of extracted from the characteristic field scale of UCF and from weak localization amplitude for $4.0 \mu\text{m}^2$ dot. (e) Lorentzian fit (Equation 3.6) to average $N = 1$ weak localization lineshape and (f) comparison of extracted from the weak localization width of the fit, and from weak localization amplitude for $4.0 \mu\text{m}^2$ dot.

3.2 Low Temperature Dephasing and Saturation of τ_ϕ

A second series of low-temperature measurements of the weak localization amplitude was performed. Although the results are consistent with from the dephasing rate dependence observed at higher temperatures, which follows $AT + BT^2$, a saturation of the phase coherence

time τ_φ is observed at temperatures below 100 mK, twice the electronic base temperature of the dilution cryostat. The saturation/roll-off appears to be genuine because in quantum dots, the electron temperature can be accurately determined in situ from either the width of Coulomb blockade (CB) peaks in dots with tunnel leads [Folk96], or from the variance of conductance fluctuations in devices with single or multi-mode leads.

Previous work has reported a similar unexpected saturation of dephasing at low temperatures in a variety of systems [Mohanty97a, Bird95a, Clarke95] and there have been many efforts to explain this phenomenon [Mohanty97b, Khavin98, Altshuler98].

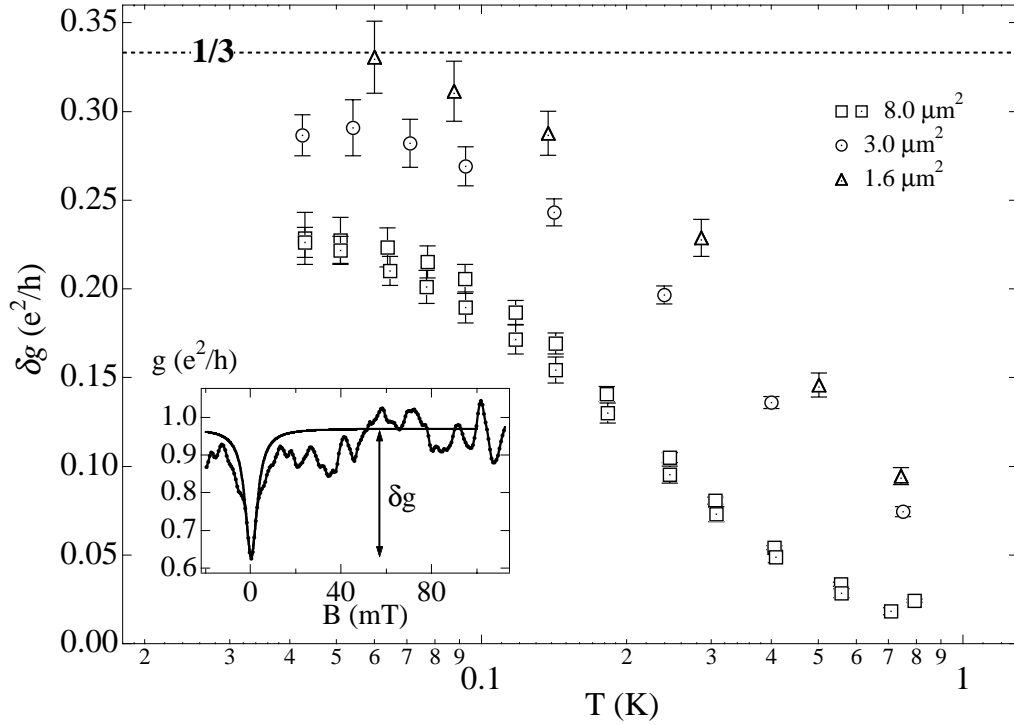


Figure 3.5: Weak localization amplitude δg as a function of temperature in quantum dots with single mode leads and an area A of $1.6 \mu m^2$ (triangles), $3.0 \mu m^2$ (circles), and $8.0 \mu m^2$ (squares). Inset shows average of 20 magneto-conductance traces for $1.0 \mu m^2$ device, clearly showing weak localization along with Lorentzian fit. For reference $\delta g = 0.263$ for $\gamma_\varphi = 1$ and 0.215 for $\gamma_\varphi = 2$.

3.2.1 Experiment

The four two-lead dots investigated in this set of measurements were formed using depletion gates located 90 nm above a two dimensional electron gas (2DEG) present at a

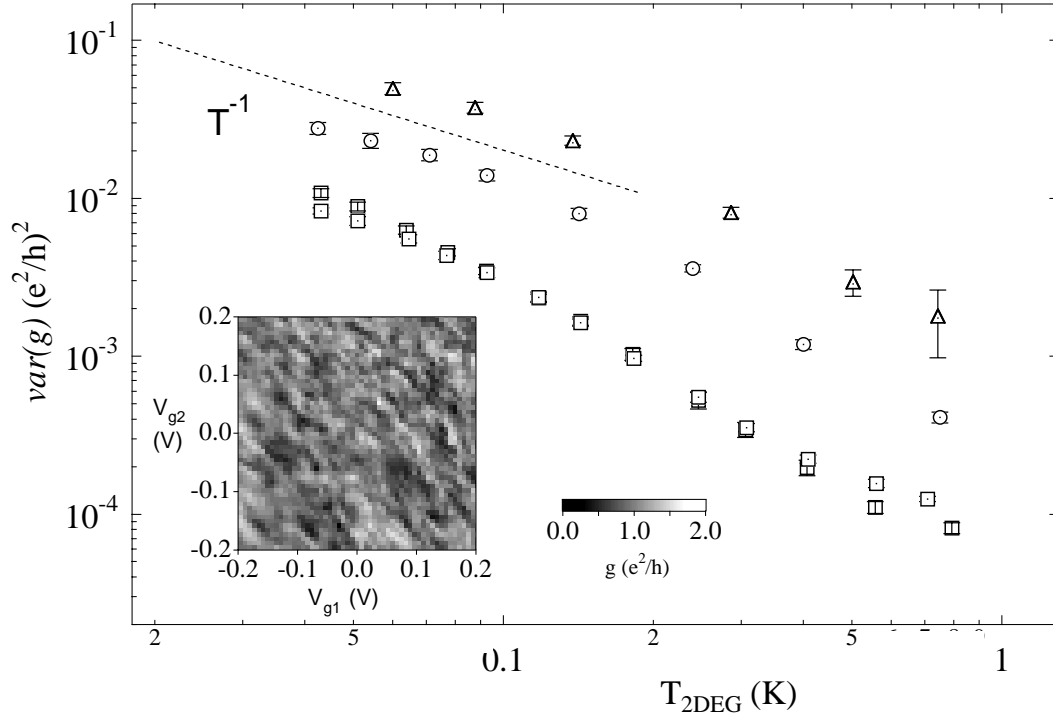


Figure 3.6: Conductance variance as a function of temperature for identical devices. The variance is measured at $B > \Phi_0/A$, where $\Phi_0 = 4.14 \text{ mT}/\mu\text{m}^2$ is the magnetic flux quantum, so that time-reversal symmetry is broken. $T_{2\text{DEG}}$ is actual device electronic temperature measured from the Coulomb blockade peak width in an $8.0 \mu\text{m}^2$ dot. At all but the lowest cryostat temperatures ($< 50 \text{ mK}$) this is identical to the cryostat temperature. Both δg and conductance variance are computed from ensembles with ~ 400 independent conductance points, drawn from conductance landscapes such as that shown in the inset, which is for $B = 30 \text{ mT}$ for the $1.6 \mu\text{m}^2$ device.

GaAs/ $\text{Al}_{0.3}\text{Ga}_{0.7}\text{As}$ hetero-interface. Electron micrographs of e-beam patterned Au/Cr gate electrodes are shown in Figure 3.7, inset, and also in Appendix B (devices C22, C32, C88, C15). With sheet density of $2 \times 10^{11} \text{ cm}^{-2}$ and mobility $1.4 \times 10^5 \text{ cm}^2/\text{Vs}$, transport is ballistic as the elastic mean free path of $1.5 \mu\text{m}$ is comparable to the size of the devices, which have areas of 1.6 , 3.0 , and $8.0 \mu\text{m}^2$ (two devices). In the quantum dots studied in this experiment, electron trajectories are predominantly chaotic, allowing the theory of Chapter 2 to be applied. Corrections due to interactions have been discussed recently [Aleiner98b] and will be addressed shortly. The measurements were performed in a dilution refrigerator with a mixing chamber base temperature of $\sim 28 \text{ mK}$. The electron temperature from this peak width $T_{2\text{DEG}}$ versus the cryostat temperature T (as measured using an RuO_2

resistor) is shown in the inset of Figure 3.7. The electron base temperature in our device was measured to be 45 mK from the CB peak width. This low temperature was achieved with careful filtering of the wiring both at room temperature and on entry to the continuous cold metal shield surrounding the device being measured. In addition, analog lockins with measurement bias voltage $V_{\text{bias}} \simeq 2\mu\text{eV}$ ($< kT/e$) were employed (see Appendix D for measurement setup details).

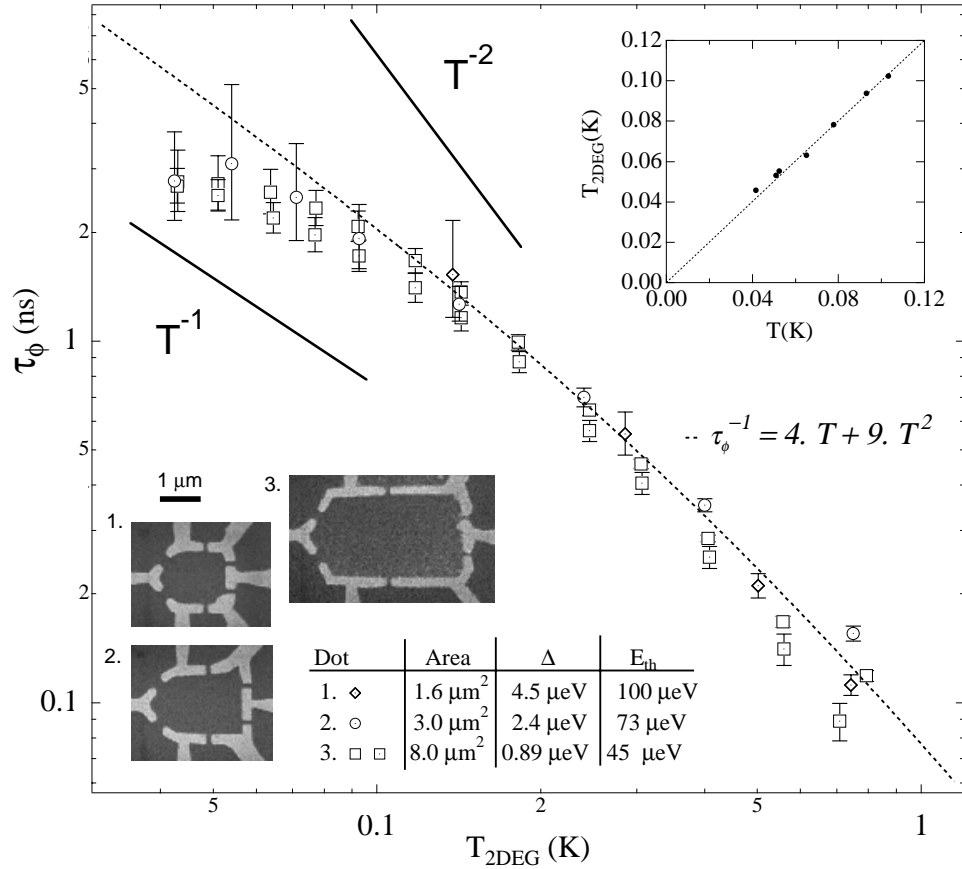


Figure 3.7: Phase coherence time τ_ϕ as a function of temperature as determined from weak localization amplitude for dots with different areas. Dashed line shows dephasing rate with $\tau_\phi^{-1}[\text{ns}^{-1}] = 4.T[\text{K}] + 9.T^2[\text{K}]$ temperature dependence; solid lines are for reference and show slopes for rate proportional to T , T^2 . Onset of saturation is observed below 100 mK. Lower inset are electron micrographs and parameters for devices measured. Upper inset shows measured Coulomb blockade peak width as a function of temperature in the $3.0 \mu\text{m}^2$ device. $E_{\text{th}} = \hbar v_F/L$ is the Thouless energy, where L is the width of the device.

Figure 3.5 shows the weak localization amplitude $\delta g = (\langle g \rangle_{B \neq 0} - \langle g \rangle_{B=0})$ versus electron

temperature. Here $B \neq 0$ denotes broken time-reversal symmetry. In the absence of dephasing and e-e interactions, $\langle g \rangle_{B \neq 0} = N e^2/h$ and $\delta g = \frac{N}{2N+1} e^2/h$ where N is the number of modes supported by each lead [Beenakker97]. The suppression of weak localization due to finite phase coherence time τ_φ can be approximated by (Eq. 2.12):

$$\delta g \simeq \frac{e^2}{h} \frac{N}{2N+1+\gamma_\varphi} \quad (3.7)$$

where the normalized dephasing rate $\gamma_\varphi = 2\pi\hbar/(\tau_\varphi\Delta)$. $\Delta = 2\pi\hbar^2/m^*A_{\text{dot}}$ is the spin-degenerate mean level spacing where A_{dot} is the dot area adjusted for depletion. As seen in Figure 3.5, the $1/3 e^2/h$ value (for $N = 1$) is approached experimentally in smaller devices at low temperatures as γ_φ falls below 1.

Conductance variance $\text{var}(g)$ is related to δg and T ([Baranger95, Huibers98b], also discussed in Sec. 2.5.4). In the case of broken time-reversal symmetry:

$$\text{var}(g) = \frac{\Delta}{6kT} f(\gamma_\varphi), \quad (3.8)$$

where

$$f(\gamma_\varphi) = \frac{2}{2+\gamma_\varphi} \frac{1}{(\sqrt{3}+\gamma_\varphi)^2}. \quad (3.9)$$

f is solely a function of δg for fixed N , via Equation 3.7. Equation 3.8 predicts a T^{-1} dependence for fixed or very small γ_φ . As seen in Figure 3.6, this is observed at low temperatures, where dephasing appears saturated in large dots, and is of negligible effect in small devices due to short dwell time ($\gamma_\varphi \ll 1$). Thus $\text{var}(g)$ acts as a thermometer at low temperature and is consistent with the CB results. For all data shown, the mean and variance of the conductance fluctuations are measured by rastering across the shape and energy conductance landscape of the device using shape-distorting gates, while simultaneously tuning the quantum-point-contact leads to each support $N = 1$ mode, a technique described in Ref. [Huibers98b].

Figure 3.7 shows the dependence of the phase coherence time τ_φ on the electron temperature. As in Fig. 3.5, temperature is measured from the CB peak linewidth. Above 100 mK, the dephasing rate τ_φ^{-1} has an $A T + B T^2$ dependence consistent with the results of [Huibers98a]. Below 100 mK however, the measured τ_φ begins to saturate. A simple explanation for this roll-off would be loss of thermal contact of the electron reservoirs and

the cryostat. However, the consistent electronic temperature measurement using two independent techniques outlined above indicates that the phase coherence roll off is not a saturation of $T_{2\text{DEG}}$.

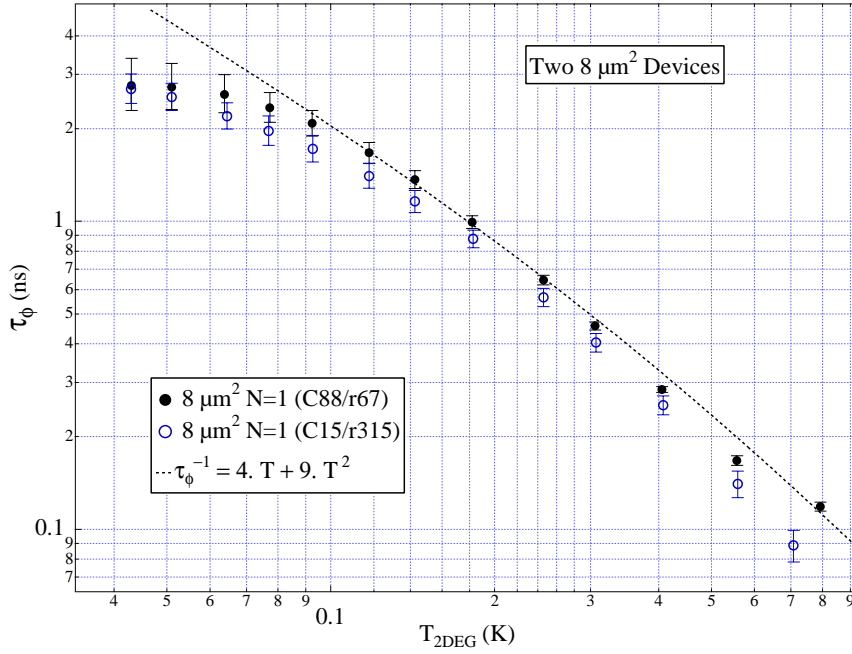


Figure 3.8: Phase coherence time $\tau_\phi(T)$ for 8 μm^2 dots. Larger devices allow more accurate quantification of time $\tau_\phi(T)$ because they show appreciable suppression of weak localization even at base temperature – see also Figure 3.5. The onset of saturation of τ_ϕ is clearly observed below 100 mK.

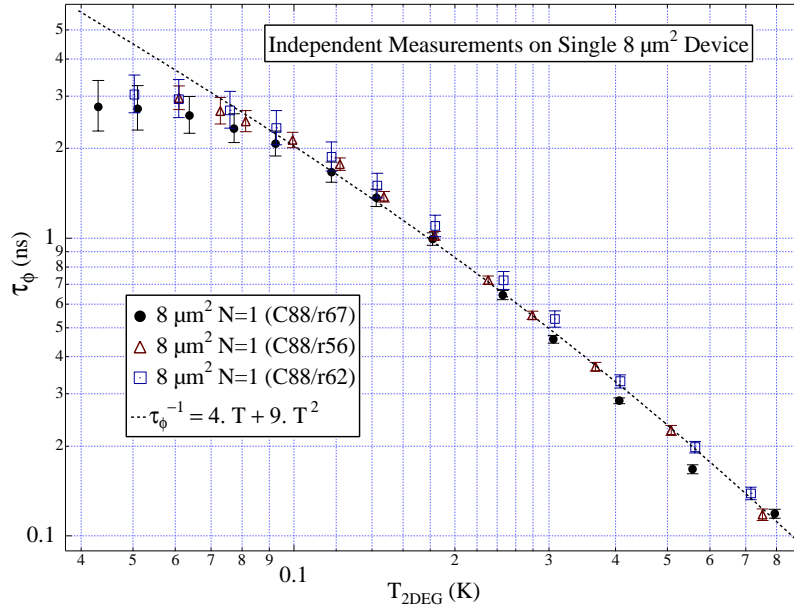


Figure 3.9: Phase coherence time $\tau_\phi(T)$ in a single device (C88) taken different days showing measurement repeatability. Each temperature sweep takes ~ 6 hours.

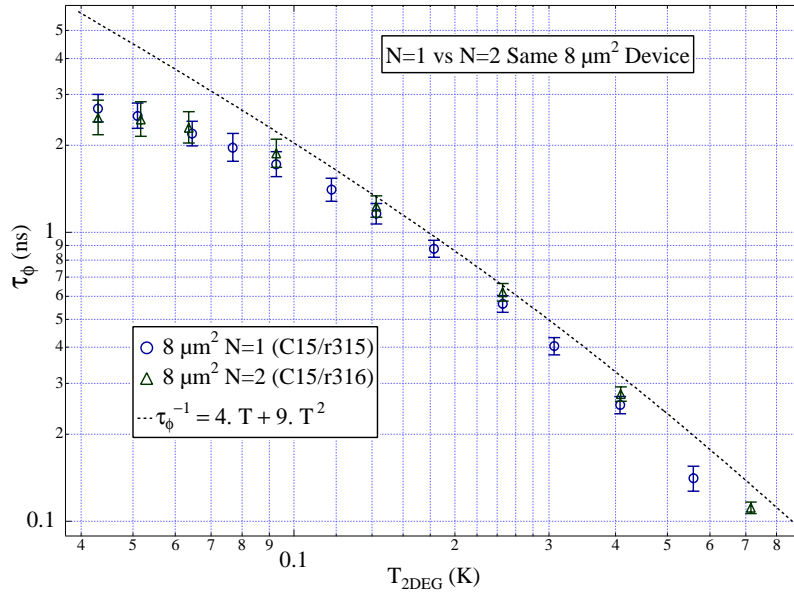


Figure 3.10: Phase coherence time $\tau_\phi(T)$ in a single device (C15) taken for $N = 1$ and $N = 2$ modes per channel. The RMT model used to extract τ_ϕ takes into account the escape rate.

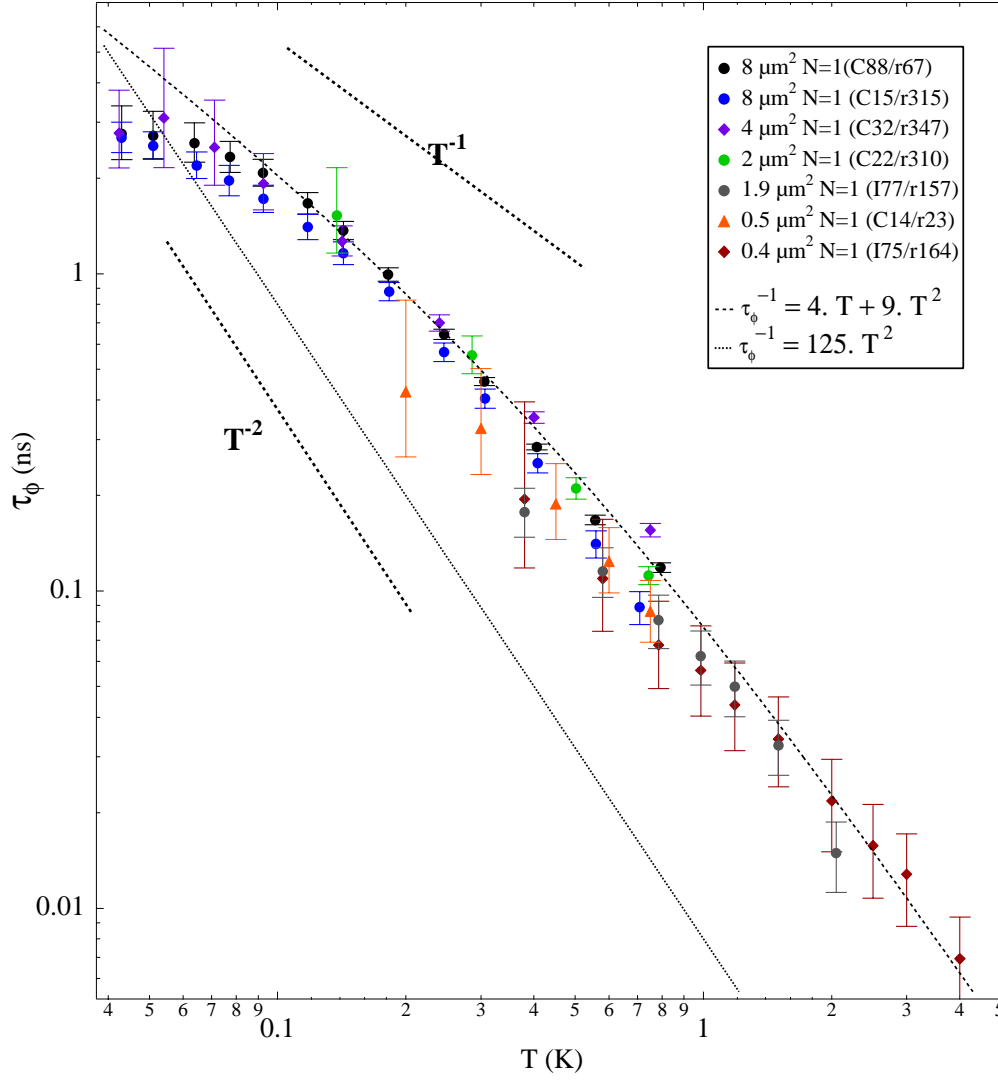


Figure 3.11: Phase coherence time $\tau_\phi(T)$. C devices were measured on dilution refrigerator; I devices were measured on He-3 system. Fit shows combined $T + T^2$ dependence of dephasing rate.

The measurements of τ_ϕ taken in these experiments are quite robust as demonstrated in Figures 3.8 through 3.10:

1. Figure 3.8 displays on a single graph $\tau_\phi(T)$ for two different $8 \mu\text{m}^2$ devices.
2. The data in Figure 3.9 were taken for the *same* device on three sequential days, showing repeatability over time.

3. Figure 3.10 shows for $\tau_\varphi(T)$ for both $N = 1$ and $N = 2$ in the same device. This serves to verify the model being using to extract τ_φ and also indicates that electron-electron interaction effects at $N = 1$ are probably small in this device.

In addition to the consistency shown above, carefully calculated error bars are shown for the data in this chapter to gauge confidence in the data. The errors in *average* quantities (e.g. errors in the estimate of the average conductance) have been determined by resampling the data in subsets that are as distant as possible so as to account for some systematic error. Such systematic error may be caused by imperfect quantum point contacts or non-ergodic transport through the device.

A composite graph of all τ_φ data (low temperature and high temperature) is shown in Figure 3.11. Some variability is observed in the absolute τ_φ magnitude but overall the trend follows the composite rate (the sum of Equations 3.1 and 3.2) for the large-energy-transfer and small-energy-transfer (Nyquist) electron-electron scattering.

The predicted phase coherence time of Sivan *et al.* [Sivan94a] for isolated systems is $\tau_\varphi = 0.0080 T^2$ for energies less than the Thouless energy, E_{th} (see discussion in Section 4.5). This is plotted as a dotted line on Figure 3.11. This theory predicts a much higher rate than is observed, and does not account for the slower than T^2 rate dependance at low temperatures.

3.2.2 Electron-electron interactions

The effect of Coulomb interactions on the results of the preceding sections is worthy of consideration. In the absence of dephasing, Brouwer and Aleiner [Brouwer98] predict an interaction induced enhancement of δg from $\frac{1}{3} e^2/h$ to $(\frac{1}{3} + \sim 0.081 \frac{\Delta}{T}) e^2/h$ at $N = 1$. In an $8.0 \mu\text{m}^2$ dot at the lowest measurement temperature of 45 mK, this is a 5% enhancement. One should note that enhanced δg does not contribute to dephasing rate saturation but rather has the opposite influence. Coulomb interactions are also predicted to increase variance by a factor $1 + \sim 2.0 \frac{\Delta}{kT}$ for the large N limit. The sizes of both of these corrections can be appreciable, however at present there is no theory developed for our experimental situation with single-mode leads and appreciable dephasing.

3.3 Transport Under High Bias

The measurements described up until now have been for a small signal applied to the quantum dot. If the measurement bias voltage is kept below kT , no Joule heating will be observed [Switkes98]. As the measurement bias exceeds kT , “hot” electrons enter the dot and transfer energy to the other electrons in inelastic collisions. The study here of dc source-drain bias will prove useful in Chapter 5, when ac bias due to radiation is considered.

3.3.1 Detailed balance model

If the inelastic collision time is shorter than the dwell time, the electrons in the quantum dot reach a pseudo-equilibrium temperature. If the leads are balanced, the Fermi energy of the dot will be midway between the Fermi energies of the two reservoirs.

The total energy flowing into the dot via transport electrons must equal the total energy flowing out of the dot:

$$\begin{aligned} \int EF_{dot}(E)(1 - F_{left}(E)) + EF_{dot}(E)(1 - F_{right}(E))dE = \\ \int EF_{left}(E)(1 - F_{dot}(E)) + EF_{right}(E)(1 - F_{dot}(E))dE \end{aligned} \quad (3.10)$$

where F_{left} and F_{right} are Fermi functions with temperature T_{res} and $E_F = +V/2$ and $-V/2$ respectively. F_{dot} is a Fermi function with temperature T_{dot} and $E_F = 0$.

Given the above information, one can solve the integrals in Equation 3.10 to obtain T_{dot} given bias V and reservoir electron temperature T_{res} . The result is:

$$\begin{aligned} (kT_{dot})^2 &= (kT_{res})^2 + \frac{3}{4\pi^2}(eV)^2 \\ T_{dot} &= \sqrt{T_{res}^2 + \frac{3}{4k^2\pi^2}(eV)^2} \end{aligned} \quad (3.11)$$

Equation 3.11 is the equivalent of the Wiedemann-Franz law for quantum dots. Figure 3.12 shows the energy distributions of electrons in the reservoirs and the quantum dot.

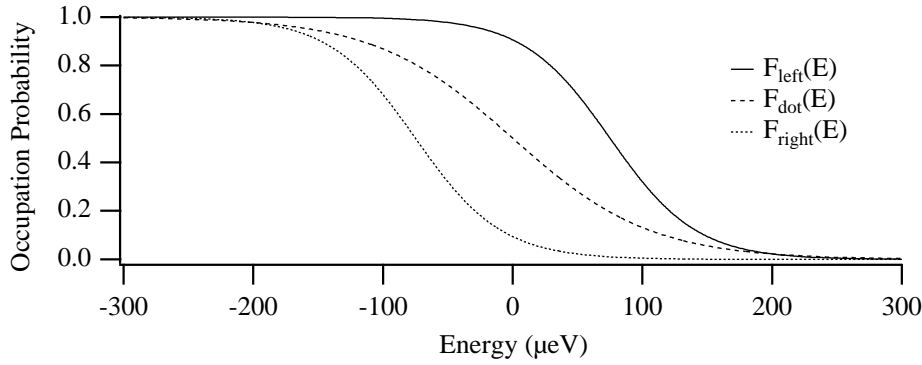


Figure 3.12: Electron energy distributions in the two reservoirs (leads) and the dot for reservoir temperature 385 mK = 33.1 μeV and a bias of 150 μeV . The equilibrium temperature in the dot $T_{\text{dot}} = 616$ mK = 53.0 μeV .

3.3.2 Experimental results

Single magneto-conductance traces for different measurement voltage biases are shown in Figure 3.13 in the 4.0 μm^2 dot (I74). These are fingerprints of the transport in the device. One observes that the trace for $T = 600$ mK can be reproduced with trace at lower temperature (385 mK) but with finite bias (165 μV).

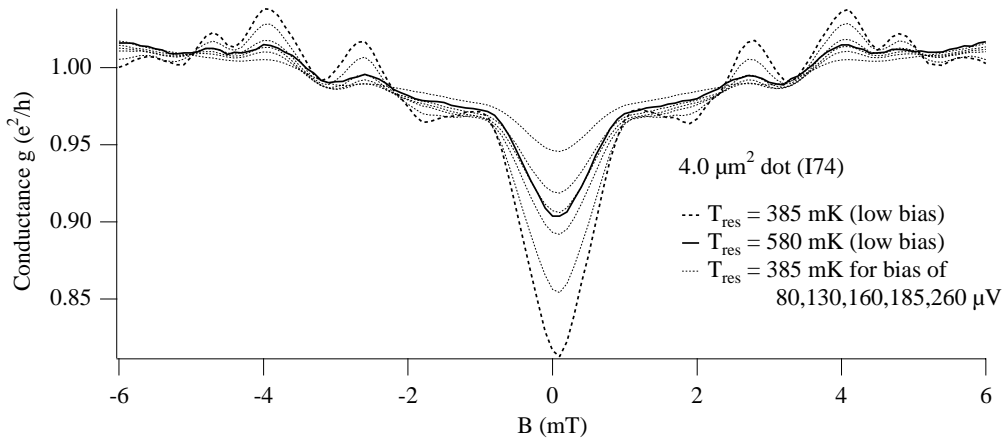


Figure 3.13: Thick traces show low-bias magneto-conductance curves at temperatures of 385 mK and 600 mK. Thin dotted traces are magneto-conductance curves for a reservoir temperatures of 385 mK and increased measurement bias, as indicated.

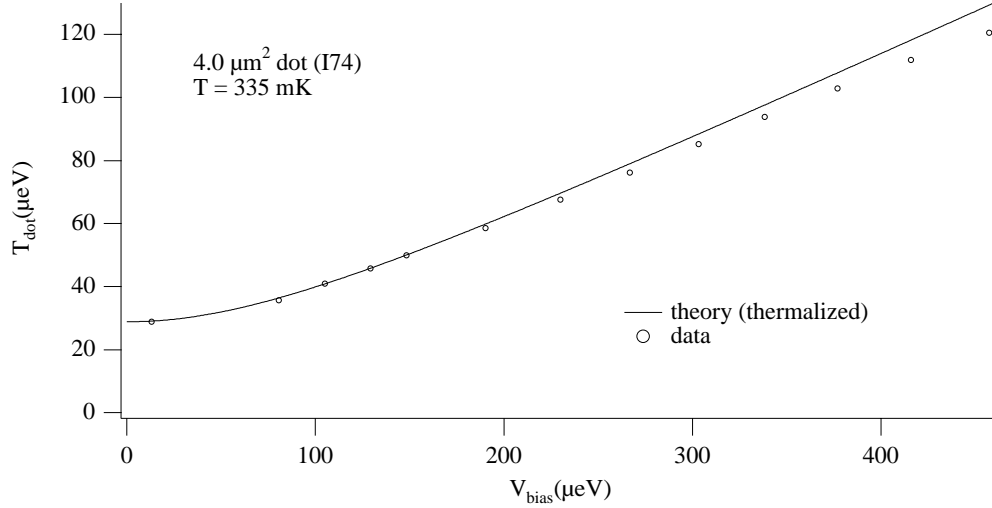


Figure 3.14: Equivalent temperature in the dot T_{dot} shown as a function of voltage bias for reservoir temperature $T_{\text{res}} = 385\text{mK} = 33.1\mu\text{eV}$. The experimental data are plotted along with the expected result as calculated from Equation 3.11.

If the single traces for different temperatures are matched to traces for biases at a fixed temperature, one can test the expression of Equation 3.11, which has no adjustable parameters. Experimental results are shown in Figure 3.14 - one sees that the agreement is excellent.

A somewhat different presentation of this data in the context of using a quantum dot as a magnetometer is developed in [Switkes98].

3.4 Coulomb Blockade at $N = 1$

The discussion and theories of transport in Chapter 2 assume that charging (Coulomb-blockade) is absent in open quantum dots, normally defined as connected to the environment with at least one lead supporting one or more quantum modes. The effect of mean electron-electron interactions was considered in Sec. 3.2.2. These effects, although potentially very large in small cold devices, have not been isolated experimentally.

In the present case of the quantum dot is connected to reservoirs with *two* leads *each* supporting a single mode. Remnant Coulomb charging effects, however, are observed as shown in Figures 3.15 and 3.16. Since both the amplitude and voltage-scale of the Coulomb-blockade-like charging are small compared to the conductance fluctuations, this effect is easy

to miss. Mesoscopic charging is a topic of ongoing investigation – specifically the “frying-pan” mode, where transport is studied in a quantum dot with one $N = 1$ lead and one tunnel lead [Matveev95, Aleiner96, Cronenwett98].

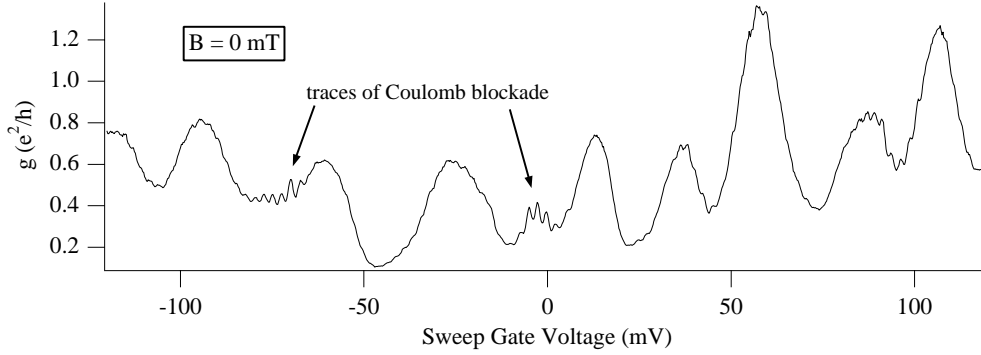


Figure 3.15: Find scale pin scan showing traces of Coulomb blockade in $2.0 \mu\text{m}^2$ dot (C2) at $B = 0$ mT.

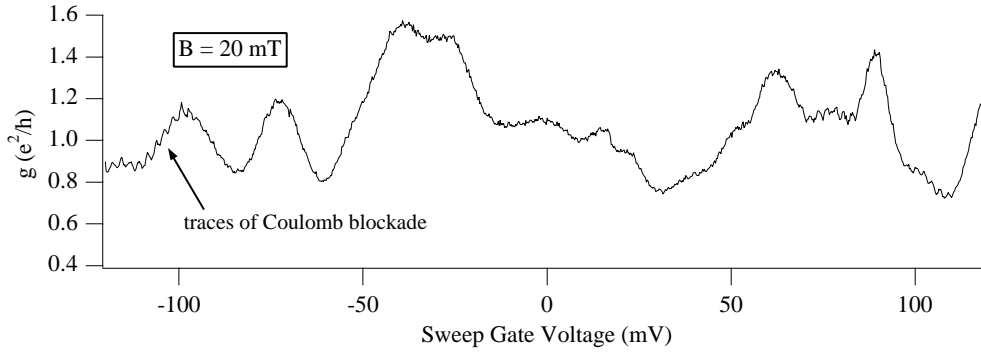


Figure 3.16: Find scale pin scan showing traces of Coulomb blockade in $2.0 \mu\text{m}^2$ dot (C2) at $B = 20$ mT.

Chapter 4

Dephasing and Interaction Mechanisms

4.1 Loss of Phase Coherence

Decoherence is the process by which the quantum mechanical properties of a microscopic system are transformed into the familiar classical behavior seen in macroscopic objects.

Semiconductor quantum dots are one of the most direct probes of quantum coherence available. As seen in the preceding chapters, a quantum dot with two leads is an interferometer: if electrons interact during the time period bounded by their entry into and exit from the dot, and scatter into new quasiparticle states, interference patterns and other effects that require quantum coherence (such as weak localization) are attenuated.

The key time scale of for the loss of coherence is the phase coherence time, τ_φ , which determines the energy and length scales at which quantum behavior is seen. Considerable theoretical [Altshuler85, Sivan94a, Blanter96, Imry94] and experimental [Echternach93, Lin86, Choi87, Kurdak92, Reulet95, Yacoby94, Clarke95, Bird95a] study has been directed toward understanding phase loss mechanisms and their dependence on temperature, dimensionality, and disorder.

In this chapter we review many dephasing and interaction mechanisms that are relevant to transport in mesoscopic nanostructures including quantum dots. It should be noted that the parameterization of all dephasing phenomena with a dephasing time τ_φ (rate τ_φ^{-1}) is an approximation, albeit a good one. τ_φ is not, strictly speaking, a relaxation time but rather a typical time scale. In other words, dephasing rates from multiple sources do not strictly

add; dephasing processes can be interrupted by other processes in a non-linear way. See [Echternach93, Lin86] or [Altshuler85, p. 70] for further discussion.

4.2 Electron-electron scattering (T^2)

Electron-electron scattering is analogous to four-wave mixing in non-linear optics, where two waves couple to two other waves within matching constraints. Although one can think of scattering “events” one can visualize a continuous process: the scattering rate quantifies the transition from one quantum state (set of states) to another.

In nonlinear optics, charges fixed at atomic sites couple photon waves, but here the waves themselves carry charge. For an electron gas with a Fermi distribution, the e-e scattering rate is dependent on the energy of the electron engaged in scattering E and the temperature of the gas T . The result to first order is

$$\tau_{ee}^{-1} = C_1 E^2 + C_2 (k_B T)^2 \quad (4.1)$$

The squared power-law dependence can be supported with a state-counting argument. Figure 4.1 show the Fermi k-space diagram for a 2D electron gas. An electron-electron scattering transition/event involves two electrons with conservation of energy and momentum. In the Figure, an electron with momentum $\hbar \mathbf{k}_1$ scatters with an electron (with momentum $\hbar \mathbf{k}_2$) in the zero-temperature Fermi gas. Two new states must have the same center of momentum (labeled “CM”) and obey energy conservation, which constrains them to the shaded region. These combined constraints combine to limit the destination momentum states to a pair of arcs (not shown) in the grey area, symmetric about CM, and each with length proportional to E . Since the areal state density is uniform, this leads to an $E \times E = E^2$ rate dependence.

Experiments by Yacoby and coworkers in GaAs/AlGaAs 2DEGs have observed a square-law τ_{ee} dependence with a two-arm interferometer both as a function of electron energy [Yacoby91] and temperature [Yacoby94]. Murphy *et al.* have seen a near- T^2 dependence in measurements of tunneling rates between *two* 2DEGs [Murphy95]. An E^2 dependence in quantum wires has also observed by [Linke97a].

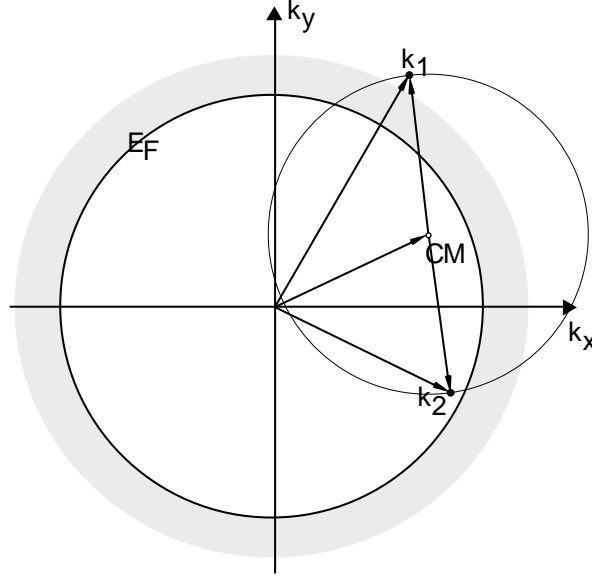


Figure 4.1: Fermi surface and k vectors.

Using a perturbative approach for small kT/E_F , based on the random phase approximation, Giuliani and Quinn have derived a classic result for τ_{ee} for a 2D system: [Giuliani82]:

$$\tau_{ee}^{-1} = \frac{1}{2\pi} \frac{(kT)^2}{\hbar E_F} \left[\ln \frac{E_F}{kT} + 1 + \ln \left(\frac{2q_{TF}}{k_F} \right) \right] \quad (4.2)$$

where $q_{TF} = 2me^2/\epsilon\hbar^2$ (ϵ is the dielectric constant) is the Thomas-Fermi screening wave vector. This result is widely quoted in experimental work [Murphy95].

Zheng and Das Sarma [Zheng96], pointing out inadequacies in the Giuliani-Quinn theory (which are fairly subtle from an experimentalist perspective) have rederived τ_{ee} in a 2D electron gas (2DEG) as:

$$\tau_{ee}^{-1} = \frac{\pi}{4} \frac{(kT)^2}{\hbar E_F} \ln \frac{E_F}{kT} \quad (4.3)$$

for $kT \ll E_F$ where E_F is the Fermi energy.

4.3 High Frequency Electric Fields

In Altshuler *et al.*'s groundbreaking 1981 paper [Altshuler81] dephasing due to high frequency electric fields (frequency of the same order as the dynamic times scale) is considered.

The phase uncertainty $\langle \delta\phi^2 \rangle$ calculated over frequency Ω is:

$$\langle \delta\phi^2 \rangle = \langle \int d\Omega \alpha(\Omega) f(\Omega t) \rangle \quad (4.4)$$

where

$$f(x) = x \left[1 + \frac{\sin 2x}{2x} - 2 \frac{\sin^2 x}{x^2} \right] \quad (4.5)$$

and

$$\alpha(\Omega) = \frac{2e^2 D E^2}{\hbar^2 \Omega^3} \quad (4.6)$$

Note that

$$\begin{aligned} f(x) &= x & x \gg 1 \\ f(x) &= \frac{2x^5}{45} & x \ll 1 \end{aligned}$$

When $\langle \delta\phi^2 \rangle \sim 1$ there is a suppression of coherence.

For single-frequency excitation,

$$\langle \delta\phi^2 \rangle = \frac{2e^2 D E^2}{\hbar^2 \Omega^3} f(\Omega t)$$

The time t when this quantity becomes ~ 1 is the dephasing time τ_φ resulting from E-field dephasing. This time is:

$$\begin{aligned} \tau_\varphi &= \frac{1}{\Omega} \left(\frac{45}{2\alpha(\Omega)} \right)^{\frac{1}{5}} & \alpha \gg 1 \\ \tau_\varphi &= \frac{1}{\Omega \alpha(\Omega)} & \alpha \ll 1 \end{aligned}$$

These power dependencies have not been observed consistently in practice, which is likely due to the presence of heating [Wang87, Vitkalov88, Liu91, Webb98].

In the radiation experiments in Chapter 5 we will see that heating and the resulting broadening of the Fermi function is the dominant effect of electric fields applied in a non-specific manner to quantum dots: coupling to the source-drain reservoirs is much more important in this case than the modification of the electron's environment by the dynamic electric field itself.

4.4 Nyquist mechanism

The expectation value of the variance of the electric fields produced by a sea of thermal electrons (the Nyquist field) is:

$$\langle E^2 \rangle \sim \frac{kT}{\sigma[l(t)]^d} \quad (4.7)$$

where d is the system dimensionality, $l(t) = \sqrt{Dt}$ and conductivity $\sigma = e^2 D \nu a^{3-d}$.

In the low power limit, Equation (4.4) becomes:

$$\langle \delta\phi^2 \rangle \sim \langle \alpha(\Omega) \rangle \Omega$$

$$\sim \frac{T e^2}{\sigma \hbar^2} D^{1-d/2} t^{2-d/2}$$

which approaches 1 at time:

$$\tau_\varphi \sim \left(\frac{\hbar^2 D^{d/2} \nu a^{3-d}}{T} \right)^{\frac{2}{4-d}} \quad (4.8)$$

a is a transverse dimension.

With proper units and so forth [Altshuler85] in a disordered 2DEG the Nyquist dephasing rate is

$$\tau_{\varphi N}^{-1} = \frac{kT}{2\pi\hbar} \frac{\lambda_F}{l_e} \ln \frac{\pi l_e}{\lambda_F} \quad (4.9)$$

where λ_F is the Fermi wavelength and l_e is the elastic mean free path.

4.5 Quantum Dot Quasiparticle Lifetime

Using a Golden Rule approach for a finite sized system, Sivan *et al.* [Sivan94a] find a dephasing rate for $kT < E_{th}$ of

$$\tau_\varphi^{-1} = \frac{32\Delta}{\pi} \Xi \left(\frac{kT}{E_{th}} \right)^2 \quad (4.10)$$

where E_{th} is the Thouless energy, i.e. inverse crossing time, which is $\frac{\pi^2 D}{L^2}$ in a diffusive system, and can be presumably taken as $\hbar v_F / \sqrt{A}$ for a ballistic system. For a ballistic device, $\Xi = \frac{9}{4}$ [Clarke95]. Note that for ballistic systems, the rate given by Equation 4.10 is independent of dot area since $\Delta \propto 1/A$.

In the high temperature limit,

$$\tau_\varphi^{-1} = 35\Delta \left(\frac{kT}{E_{th}} \right)^{\frac{3}{2}} \quad (4.11)$$

which is equivalent to the Nyquist rate in 3D (the description of Nyquist dephasing in Section 4.4 applies only to 1D and 2D systems – a full treatment may be found in [Altshuler85]).

The dephasing rates of Equations 4.10 and 4.11 are a result of interaction processes with small momentum transfer, as compared to the large momentum and energy transfer process of Section 4.2, and can be thought of as scattering due to the density fluctuations that exist within the confined dot environment (fluctuation wavelength comparable dot size).

This formulation is for closed systems and is applied to the present regime (open quantum dots) with caution. Experimentally, we observe a strong departure from a T^2 dephasing rate at low temperatures, as was seen in Section 3.2.1.

In closed systems, the quasiparticle lifetime is predicted to diverge sharply at low energies (temperatures) as the number of accessible single and multi-particle states becomes limited [Altshuler97].

4.6 Intrinsic Dephasing

It has been recently proposed that zero-point fluctuation of the electromagnetic environment result in an upper limit on τ_φ in electronic systems of τ_0 :

$$\tau_0 = \left(\frac{e^2 d^2 R m^* D^{3/2}}{4\pi \hbar^2 L} \right)^2 \quad (4.12)$$

where d is the dimensionality, R is the sample resistance, m^* is the effective mass, D is the diffusion constant and L is the length of the sample. This formula is so far valid only for 1D disordered films [Mohanty97a, Mohanty97b].

The validity of this theory has been challenged by Altshuler and coworkers [Altshuler98] who argue that small quantities of radiation leaking into the experiment must cause observed saturation. Although Equation 4.12 seems to give a reasonable prediction of saturation of the data presented in [Mohanty97a, Mohanty97b], experiments performed with 1D conductors in a regime of high-disorder [Khavin98] do not observe the predicted saturation. The prospect of there being some sort of intrinsic dephasing is an active subject of debate. Other possibilities for saturation effects include switching noise as a result of quantum tunneling.

4.7 Electron-phonon Scattering

In semiconductors there are interactions between the electrons and excited modes of the charged lattice. At low temperatures electron-phonon scattering rates are small compared to electron-electron scattering rates and have a rate proportional to T^3 , which has been observed experimentally in GaAs/AlGaAs 2DEGs. Using a dilution refrigerator, Mittal and coworkers observed that $\tau_{e-ph} = 5$ ns at 1K [Mittal96]. This rate is too low to have an effect in the experiments here.

4.8 Spin-orbit Scattering

The spin-orbit scattering time in AlGaAs is expected to exceed the measured τ_φ by at least an order of magnitude over the temperature range studied [Millo90, Dresselhaus92]. Significant spin-orbit scattering would lead to a local maximum of conductance at $B = 0$, which is not observed. This is seen in Figure 4.2, which shows weak localization curves at low *electron* temperature, along with expected fit (Equation 3.6) .

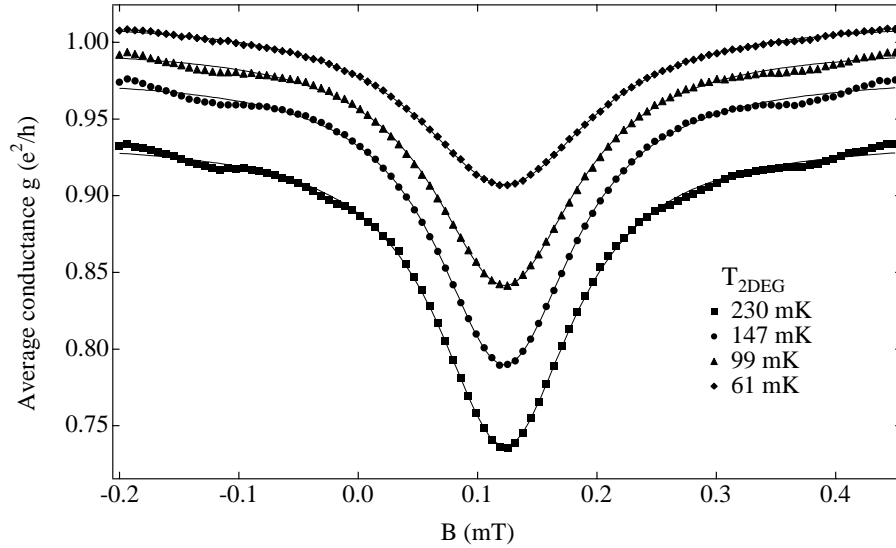


Figure 4.2: Weak localization curves for different temperatures along with Lorentzian fit.

4.9 Summary

Over the temperature range of the experiments described in this thesis, electron-electron interactions are believed to be the dominant dephasing mechanism.

Experimentally as seen in Chapter 3 (see for example Figure 3.11), we observe a slower-than- T^2 temperature dependence for the dephasing rate. Surprisingly, the measured dephasing rates in quantum dots agree very well quantitatively with the rates expected for disordered 2D systems, where dephasing is a sum of contributions from electron-electron scattering and from Nyquist interactions. This indicates that some type of Nyquist dephasing may be taking place in our open dot system that is different from that calculated by Sivan *et al.* [Sivan94b].

Chapter 5

Microwave Excitation of Quantum Dots

5.1 Introduction

In order to investigate the role of electromagnetic coupling to the dot's environment on dephasing, we have deliberately applied a microwave electromagnetic field over a broad power level and frequency range. We observe that the microwave field increases the dephasing rate, and that the increase can be fully attributed to heating of the transport electrons, which can be independently measured. The effect of the microwave field can be modeled as a voltage bias on the source and drain reservoirs, with transport electrons heated in a manner analogous to Joule heating. Nonlinear Coulomb blockade measurements show rectification and support this picture. Since the electromagnetic coupling observed produces dephasing commensurate with the observed heating, the existence of background microwave-frequency electromagnetic fields is not a satisfactory explanation for the rolloff in phase coherence time for electron temperatures below 100 mK or the observed sub- T^2 dephasing rate, which remain unexplained. Previous work investigating the effect of microwaves on transport in metal films [Liu91, Wang87], wires [Webb98] and in silicon MOS structures [Vitkalov88] have observed the reduction of phase coherence with radiation, but the relative importance of Joule heating versus a truly ac effect is unclear.

In order to investigate the saturation of the temperature dependence, microwave fields were deliberately coupled into the quantum dot devices. The coupling geometry is shown in the Figure 5.1 inset: a 1.5 mm coaxial waveguide is attached to an open biaxial antenna

segment of width and length ~ 7 mm which is positioned 4 mm above the sample. Note that since the electromagnetic wavelength ($1 \text{ GHz} = 30 \text{ cm}$) is much larger than the geometrical dimensions of the apparatus, the radiation is near-field.

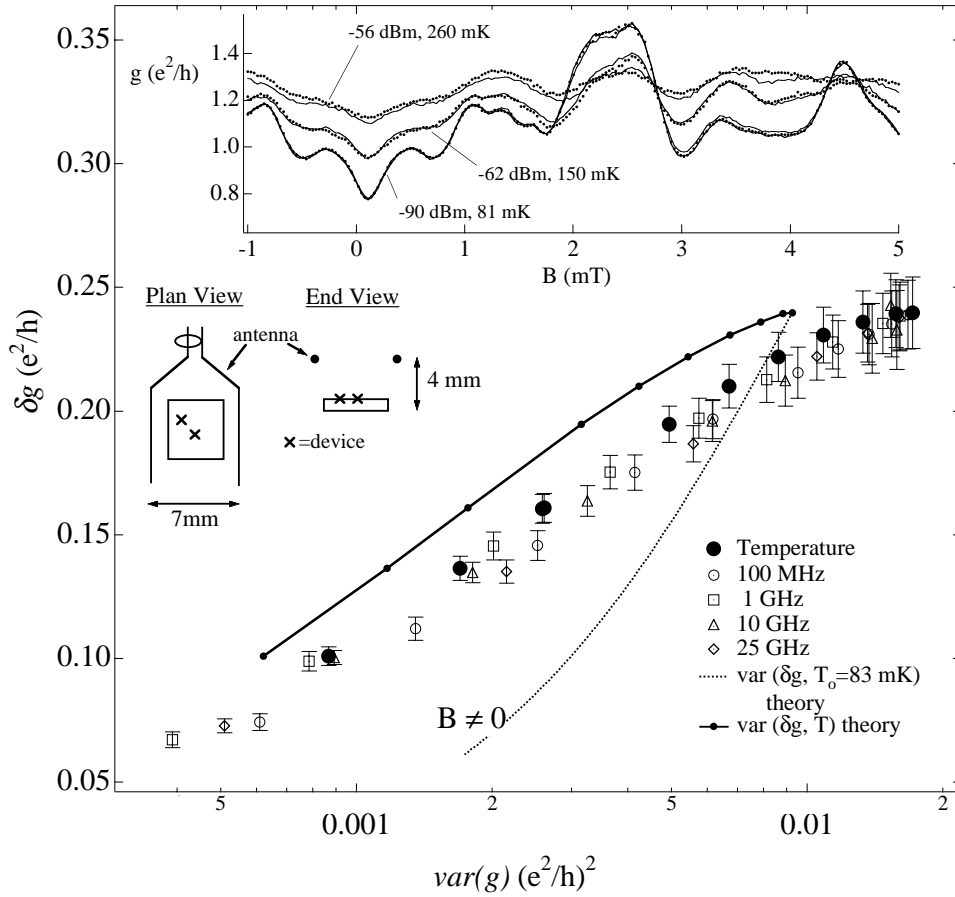


Figure 5.1: Main axes: weak localization amplitude δg versus conductance variance for $3.0 \mu\text{m}^2$ quantum dot, for temperatures between 83 mK (upper right) and 400 mK (lower left), along with measurements taken at the electronic base temperature of 83 mK (cold metal shield partly removed) and a range of microwave powers at four different frequencies. Connected lines show theoretical δg , $\text{var}(g)$ relationship calculated for the case of reservoir temperature fixed at $T_{\text{res}} = 83 \text{ mK}$ (dashed), and for the case of changing reservoir temperature (solid). For changing reservoir temperature, $T_{\text{res}}(\delta g)$ is obtained from temperature series data. Inset compares single magnetoconductance traces at different microwave power levels at 700 MHz for $T = 83 \text{ mK}$ (dots) with traces taken for increasing electron temperature (lines).

5.2 Measurements

In Figure 5.1, δg is plotted versus $\text{var}(g)$ in order to compare measurements made at increasing temperature (solid circles) with increasing microwave power levels (open symbols). The two data sets are seen to have the same parametric dependence to within experimental error. We investigate the data with two theoretical cases using Equation 3.8, where δg is directly related to γ_φ by the relation $\delta g \simeq \frac{e^2}{h} \frac{1}{2N+1+\gamma_\varphi}$ (Equation 2.12).

The first case is for variable dephasing and fixed temperature (*no electron heating*). T is held fixed at 83 mK, the measured base temperature of the devices during the microwave measurements with some shielding removed. For this case, δg is a parametric function of $\text{var}(g)$ only, and the theoretical δg versus $\text{var}(g)$ is plotted on Figure 5.1 as a dashed line.

The second case is dephasing *due to electron heating*. Therefore T is derived from the experimentally measured curve $T(\delta g)$, for no applied microwave field. The solid line in Figure 5.1 shows the resulting $\text{var}(g)$.

The good agreement of the temperature dependence of the experimental data with this solid line, and the overall indistinguishability of microwave radiation data and data taken with direct heating of the cryostat, indicates that the primary effect of the microwave electromagnetic field is to heat the electrons. This conclusion is further supported by the observation that single magneto-conductance traces for cryostat temperatures of 150 mK and 260 mK (plotted in Figure 5.1 inset) are nearly identical to traces at base cryostat temperature and appropriate microwave power levels.

The magnetoconductance data of the inset of Figure 5.1 is shown in expanded form in Figure 5.2 for a large range of power levels and temperatures. Again the thermal and microwave power traces are nearly identical. Note that the -90 dB measurement is done twice, once at the beginning of the measurement data set and once at the end, and that the two resulting curves are nearly identical. Thus there is not significant drift over the curve measurements. Such drift occurs due to charge switching (see Appendix B). In general, radiation did not appear to affect “switching noise” in the devices.

We explore these thermal and radiation-modified magnetoconductance “fingerprints” further in Figures 5.3, 5.4 and 5.5. In Figure 5.3 we see a case in which the trace for increased temperature (solid line, 100 mK) does not exactly coincide with the microwave traces, which are grouped together. This small amount of deviation could possibly be accounted for by the difference in electronic energy distribution between the pure thermal

(Fermi distributed) and microwave-excited (sinusoidal smear) cases. Close inspection of curves at two different frequencies shows detectable differences between frequencies, as seen in Figure 5.4. To amplify the difference between traces taken for different frequencies, Figure 5.5 shows the residual magnetoconductance after the average over five different frequencies has been subtracted off. It is very interesting that low and high frequencies group together: these differences are small, but indicate the presence of an effect with definite time scales.

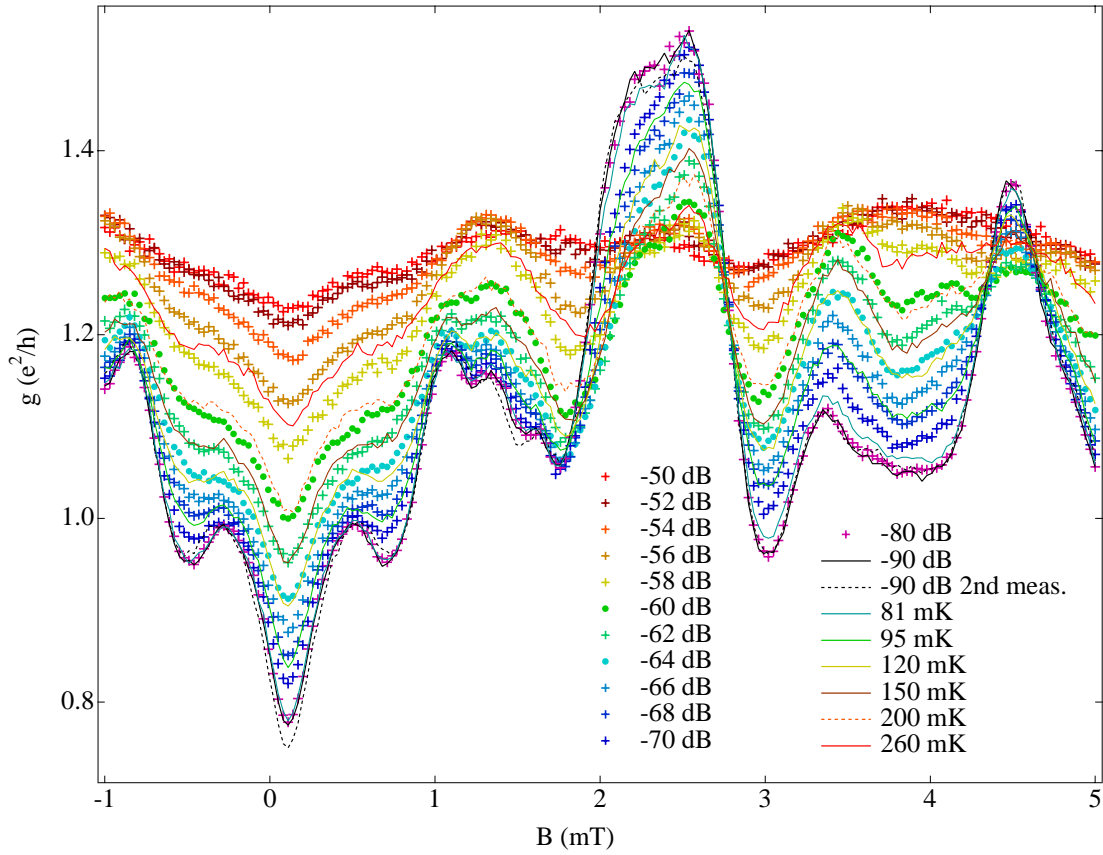


Figure 5.2: Magneto-conductance curves for incremental radiative power levels at 700 MHz (symbols) match well with curves taken at elevated temperature.

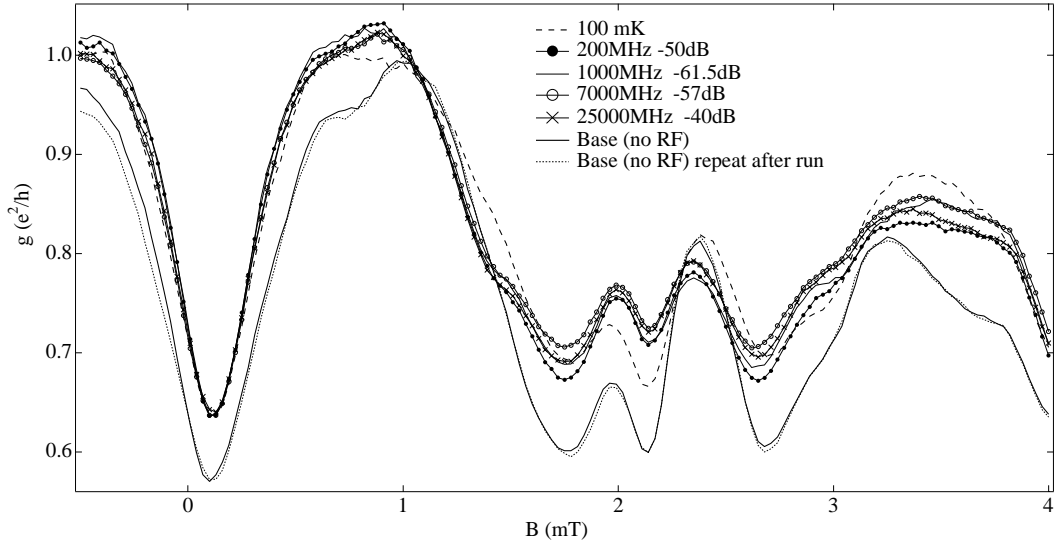


Figure 5.3: Similar graph as above; temperature and radiation curves are distinguishable. Given temperature and scale however results are consistent with the scans above. Repeated scan at base temperature shows repeatability of dot measurement over time scale of measurement (1 hour).

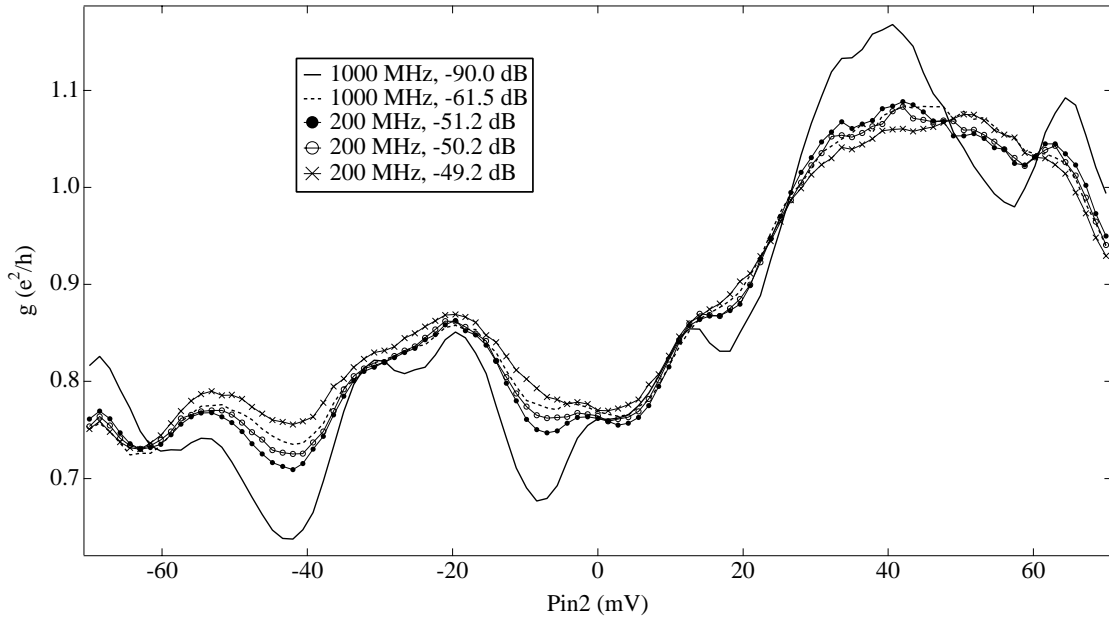


Figure 5.4: Attempt to match $g(V)$ curves at 200 MHz to reference curve at 1 GHz, -61.5 dB by varying the 200 MHz power. Although the match is good, it is not perfect, indicating that different frequencies cause *slightly* different behavior.

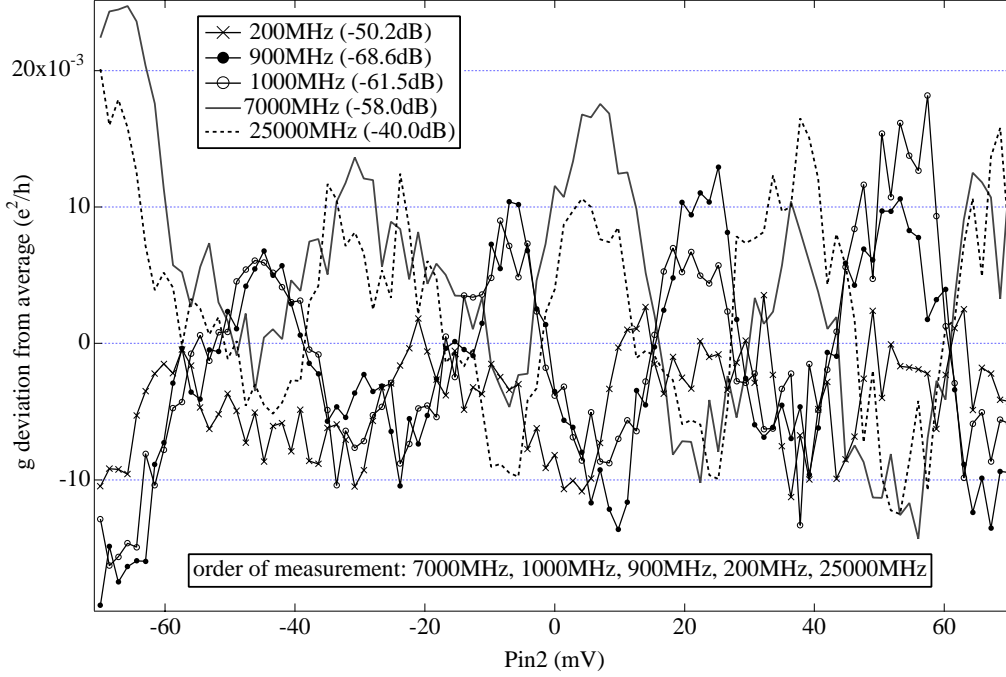


Figure 5.5: Same data as Figure 5.4, but best match to reference $g(V)$ curve has been found at each of several frequencies, and the average $g(V)$ has been subtracted. Note the discernable clustering of high and low frequency measurements.

5.2.1 Joule heating

Fixed source-drain bias held across a quantum dot will heat the electrons in the device as described in Sec. 3.3 and Ref. [Switkes98]. If the electron energies are Fermi distributed, the degree of heating can be calculated using an adaptation of the Wiedemann-Franz law. The relation between dot equilibrium temperature T_{dot} , reservoir temperature T_{res} , and bias V_{SD} is $T_{\text{dot}}^2 = T_{\text{res}}^2 + \frac{3\pi^2}{4k^2e^2} V_{\text{SD}}^2$ (Equation 3.11). Given T_{res} , V_{SD} can be calculated from the above relation if we estimate T_{dot} from conductance measurements. T_{dot} for $N = 1$ data is estimated by matching δg , $\text{var}(g)$ measurements (figure 5.1) for increasing microwave powers with those for increasing temperature. For the Coulomb blockade data, T_{dot} can be determined directly from the CB peak width, which is shown for different power levels in Figure 5.6.

Estimated bias voltage versus microwave power for both CB and $N = 1$ for four different frequencies (100 MHz to 25 GHz) is shown in Figure 5.7. The dependance of V_{SD} on microwave power closely follows a $P \propto V^2$ relation (dashed line) over more than an order of

magnitude. This is strong evidence that microwave coupling to the device Joule heats the device primarily through source-drain fluctuations.

It is clear that even though the slopes are identical for the data in Figure 5.7, the absolute coupling at different frequencies varies widely. This coupling seems to be predominantly frequency dependent—the heating for CB and $N = 1$ are highly correlated, and is likely due to the coupling of the antenna to the quantum dot structures. To get a third measurement of coupling, the effect of the microwave radiation on three of the quantum point contacts was studied for different frequencies as shown in Figure 5.8. For a given frequency, it is seen that the microwaves heat/couple to the different QPCs about equally, indicating that the effect is classical. Note that the CB and $N = 1$ data were taken on two different devices, however, these were located only ~ 0.9 mm apart from other on the same substrate.

The rigid coax connecting the microwave generator to the antenna attenuates as expected without any significant resonances up to 15 GHz as seen in Figure 5.9. Coupling differences for frequencies below 15 GHz are likely due to antenna and dilution fridge cavity geometry.

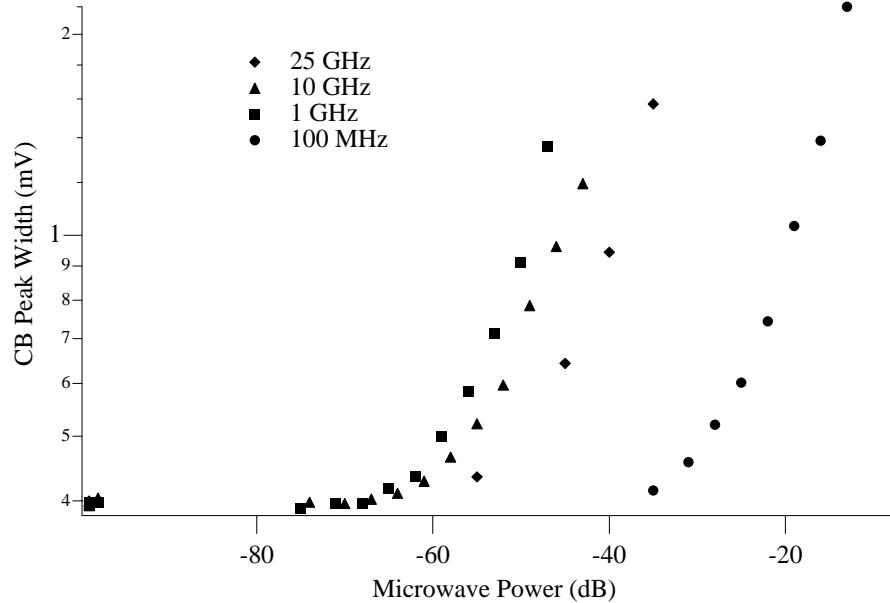


Figure 5.6: Coulomb blockade peak width in $1 \mu\text{m}^2$ dot vs microwave power. The very highest microwave powers actually heat the cryostat as label on the graph, however, base temperature is restored within a few minutes.

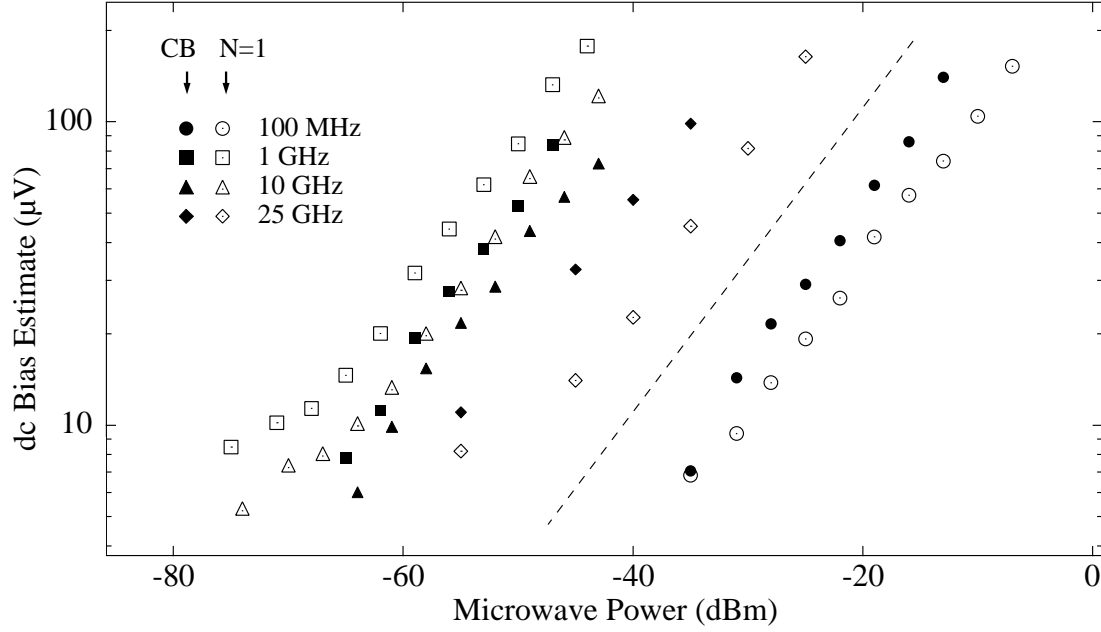


Figure 5.7: dc source-drain voltage required to produce the heating effect observed in measurements of the Coulomb blockade peak width (solid symbols) in the $1.0 \mu\text{m}^2$ devices and of weak localization in the $3.0 \mu\text{m}^2$ device with $N = 1$ mode per lead (open symbols). This voltage is calculated from the effective temperature of the device as described in the text, and is shown versus increasing microwave power for four different microwave frequencies. Dashed line shows one decade in voltage = 20 dB in power i.e. $P = V^2/R$. This is convincing evidence that reservoir coupling is the most important manifestation of radiative coupling into the system.

freq	QPC1 on 1 μm^2 dot	QPC1 on 3 μm^2 dot	QPC2 on 3 μm^2 dot
200 MHz	-25 dB	-23 dB	-21 dB
900 MHz	-50 dB	-49 dB	-48 dB
1 GHz	-36 dB	-36 dB	-36 dB
7 GHz	-44 dB	-43 dB	-40 dB
25 GHz	-33 dB	-24 dB	-20 dB

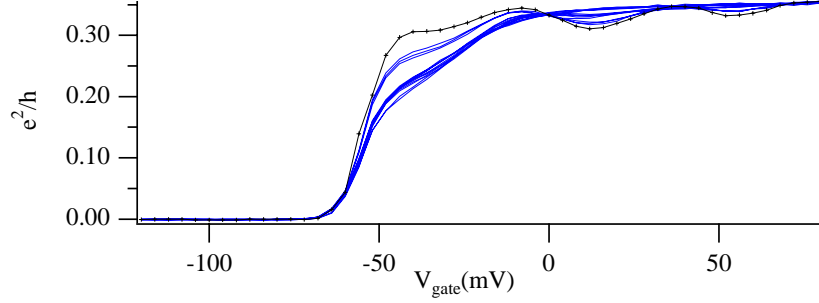


Figure 5.8: QPC comparison – powers required to create equivalent QPC trace washout in the two devices studied. Representative raw QPC data shown at bottom. QPCs are relatively robust to energy smearing and high equivalent temperatures ~ 1 K must be reached to have smearing.

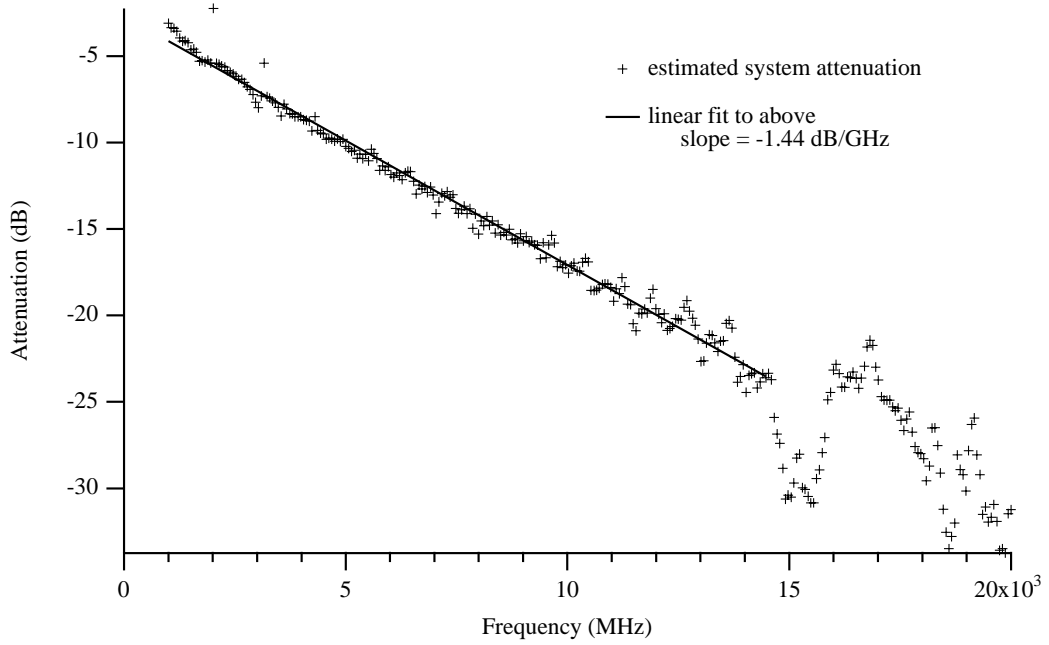


Figure 5.9: Attenuation of microwave power as a function of frequencies for rigid coax installed in dilution refrigerator. Attenuation is between microwave source and antenna connection.

5.2.2 Non-linear Coulomb blockade

The picture of Joule heating by reservoir fluctuations is consistent with data taken in the non-linear Coulomb blockade regime with microwave fields present. A detailed description of non-linear Coulomb blockade can be found in [Stewart99]. Figure 5.10 shows the differential conductance through the $1.0 \mu\text{m}^2$ device as a function of the voltage applied to a side gate (energy) and the source-drain voltage. For measurements taken at fixed temperature, with no microwave field applied, there is no electron flow through the device for $V_{\text{SD}} = 0$ as seen in the top row of plots. When microwave fields are applied with the accompanying source-drain fluctuations, the Coulomb blocked dot rectifies the fluctuations as a function of V_{gate} for $V_{\text{SD}} = 0$ (bottom row). Figures 5.10(c) and (f) show simulations of the effect of a temperature of 280 mK and of a $25 \mu\text{V}$ peak sinusoidal source. The latter is accomplished via a convolution with a sinusoidal V_{SD} drive.

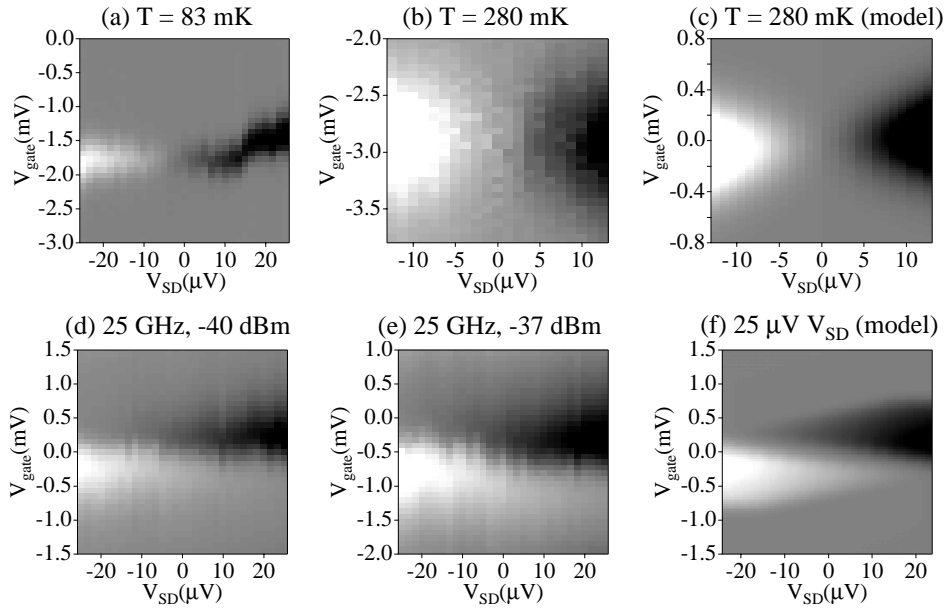


Figure 5.10: Non-linear Coulomb blockade plots of conductance as a function of drain-source voltage V_{SD} and gate voltage V_{gate} for (a) base temperature and no microwaves (b) $T = 280 \text{ mK}$ (c) $T = 280 \text{ mK}$ simulated (d) base temperature with -40 dBm at 25 GHz coupled to antenna (e) base temperature with -37 dBm at 25 GHz coupled to antenna (f) simulated ac source-drain fluctuations with rms amplitude of $30 \mu\text{V}$.

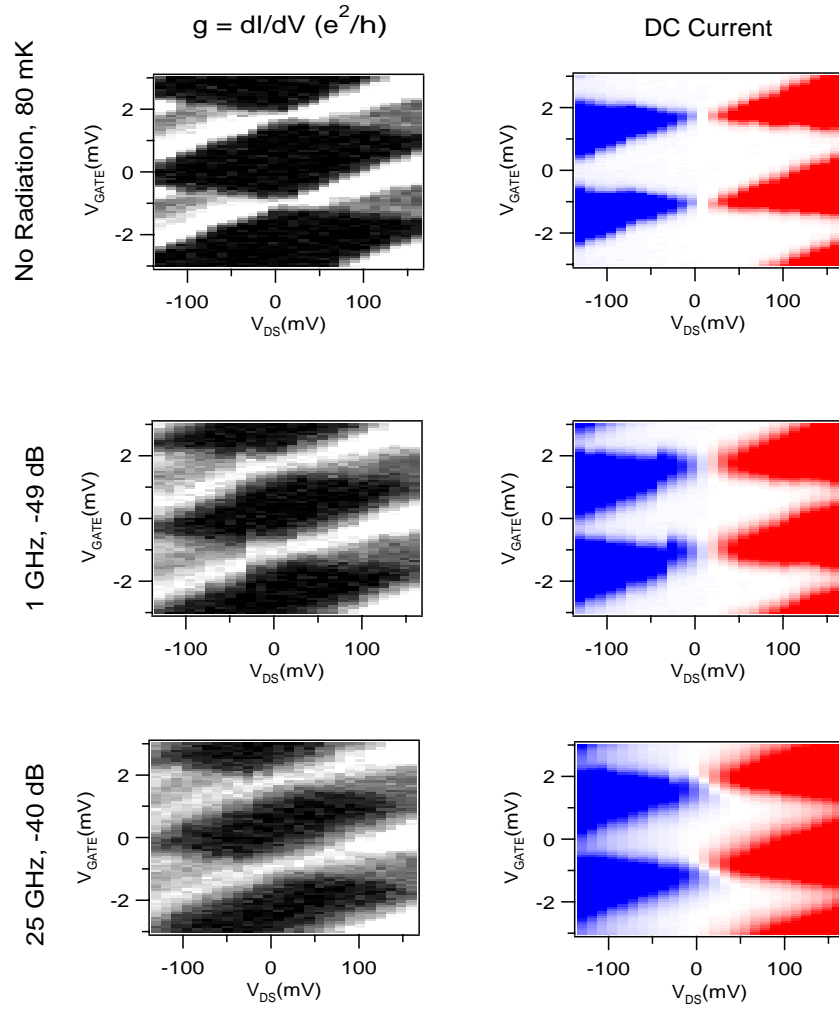


Figure 5.11: Differential conductance (left, greyscale) and dc current (right, color) through the Coulomb blocked dot for no radiation, radiation at 1 GHz and radiation at 25 GHz with approximately the same heating power (see Figure 5.7).

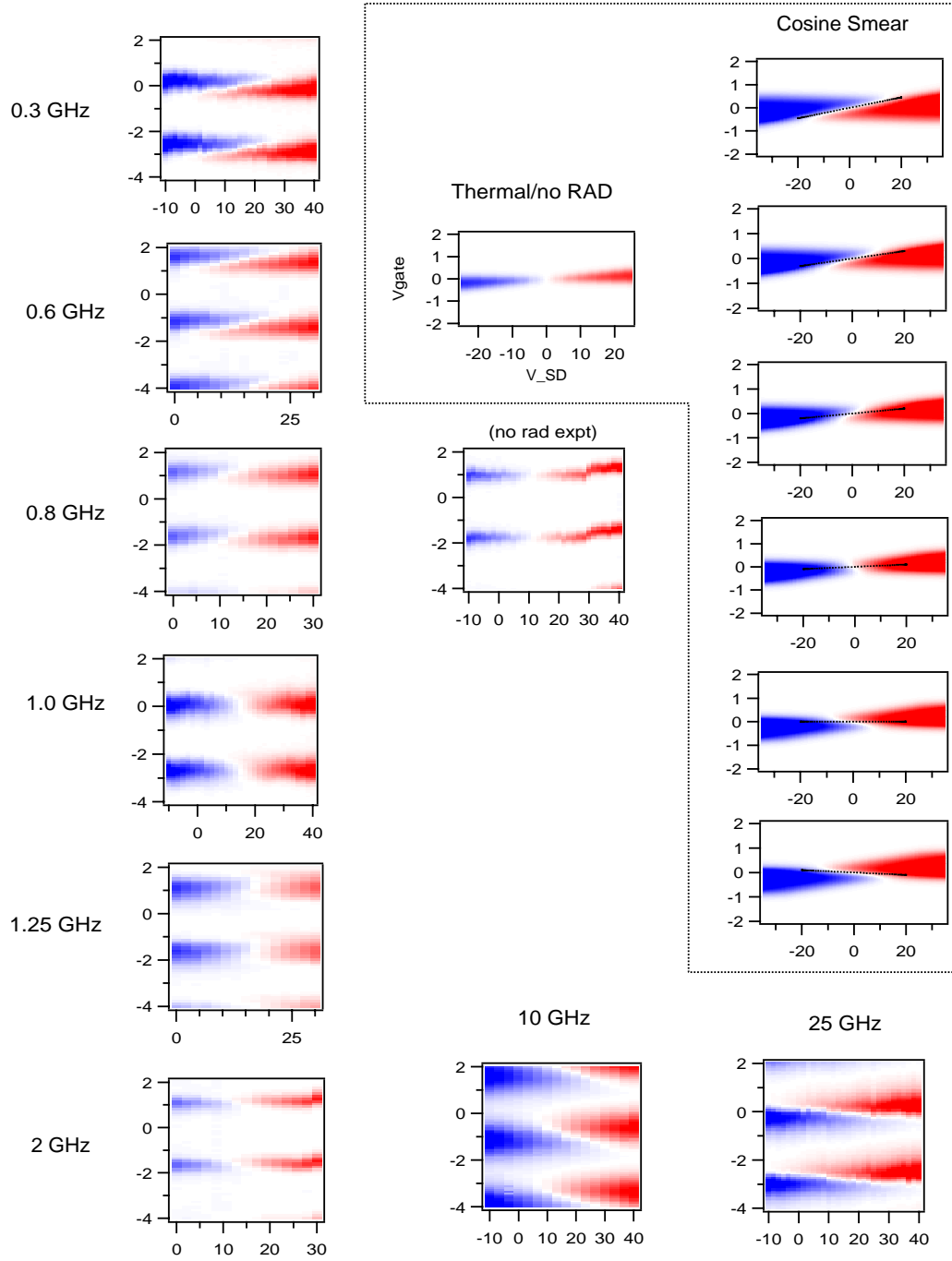


Figure 5.12: Current through the $1 \mu\text{m}^2$ dot in Coulomb blockade mode vs. gate voltage and source-drain voltage. The plots inside the dashed lines are a model (see Appendix E), which shows possible source-drain smearing convolution consistent with measured current maps.

Both conductance (proportional to dc current) and differential conductance, where individual quantum energy eigenstates become resolved, are shown in Figure 5.11 at two different frequencies. The two frequencies clearly have different effects. This is explored further in the series of measurements shown in Figure 5.12 for frequencies ranging from 300 MHz to 25 GHz, where we see a clear evolution. A possible explanation for the observed evolution is that both the gate voltages as well as the source-drain bias are fluctuating due to the microwave excitation, and that the relative phase of these excitations is changing with frequency. This is explored with a model, shown in the area of Figure 5.12 separated by a dashed boundary, in which we are able to emulate the measurements by changing the phase and amplitude of the gate voltage excitation while keeping the source-drain amplitude constant. The model used to generate the simulations is described in Appendix E.

5.3 Discussion

Up to frequencies $E_{th}/\hbar \simeq 100$ GHz electrons within the quantum dot will screen electric fields in the plane of the 2DEG. Such fields can penetrate only of the order of the Fermi wavelength into the dot at the perimeter and therefore have only a $1/\sqrt{M}$ effect on the dot potential, where M is the number of electrons in the dot. Experimentally, the correlation scale of conductance fluctuations in gate voltage is several mV (see inset Figure 3.5), while the dc source-drain voltage necessary to perturb the dot at low temperatures is much smaller (of order Δ/e – a few μV for our device areas) [Linke97c, Switkes98]. Thus the near field (capacitive) coupling to the quantum dot occurs primarily through the source and drain reservoirs. As seen in Figure 5.7, only 10's of μV of source-drain bias are required to cause substantial heating in the device.

The effect of the magnetic component of the EM field on the dot transport is tiny: 1 mA through a wire produces a magnetic field of $0.2 \mu\text{T}$ at 1 mm radius. This is much larger the current that is present in our antenna at the highest power levels (dBm). The motors in the basement produce low frequency (60 Hz) magnetic fields that penetrate the cryostat. However, the on-axis magnetic field 3 meters away from a 100-turn 5-cm radius solenoid with 1 Amp current running through it is only $2 \cdot 10^{-9}$ T.

Environmental electromagnetic fluctuations couple primarily into the devices studied through the reservoirs. In open measurements this is manifest as decrease in the weak localization amplitude along with any decrease in variance. To sum up, for a microwave field

deliberately applied to the device, we find that over all powers and frequencies measured the principal effect is simply to heat the device through modulation of the source-drain voltage. The equivalent temperature achieved with increasing levels of radiation can be described with a simple voltage bias model. Therefore, microwave coupling does not serve to explain the dephasing temperature behavior.

Chapter 6

Discussion and Conclusions

6.1 Research Context and Philosophy

This research constitutes a “second generation” of quantum dot experiments, which capitalizes on early efforts to understand dot transport including the experiments described in [Marcus92, Bird94a, Chan95, Clarke95]. The experiments in this thesis are intentionally quantitative, and are conducted in a regime (e.g. single mode point contacts, chaotic transport) where many of the transport characteristics of the devices should be well understood and quantitatively predictable at a statistical level. The main quantity of interest, the phase coherence time τ_φ , is extracted from the measurements with a high degree of confidence in the applicability the theoretical tools used [Beenakker97, Efetov97], many of which have been only available recently.

To the extent possible, the experiments in this thesis were conducted with care. Although it is impossible to build perfect devices, dots with significantly scarred trajectories and quantum point contacts with resonances were rejected and not measured. Attention was paid to measure devices of the appropriate size so that the results of interest (e.g. distribution asymmetry, or dephasing rate) could be extracted with the least amount of uncertainty, and also to cover a large area of measurement phase space (including dot area, lead open-ness, and source-drain bias) in order to test our understanding of quantum transport. Multiple devices were expected to and did in practice yield consistent results, even when the devices were based on different 2D electron gas substrates. Finally, good electronics practice, with attention paid to filtering, grounding, and noise was maintained throughout the measurements.

6.2 Summary of Accomplishments and Results

Full distributions of conductance through quantum dots with single-mode leads have been measured for both broken and unbroken time-reversal symmetry using large ensembles of shape-deformable chaotic GaAs quantum dots. Accurate control of lead conductance and low temperature allow for the observation of non-gaussian conductance distributions. This provides a stringent test of statistical theories of mesoscopic conductance fluctuations, specifically allowing nontrivial predictions of random matrix theory to be observed.

Conductance distributions are observed to agree well with RMT calculations that account for a finite dephasing time, τ_φ , once broadening due to finite temperature T is also included. Some features however, in particular the ratio of variances $\text{Var } g_{\beta=1}/\text{Var } g_{\beta=2}$, are inconsistent with the present model and remain unresolved. Full distributions of the derivatives of conductance with respect to gate voltage $P(dg/dV_g)$ were also investigated, though there is no theory for their evolution with temperature and dephasing at present.

In this thesis, shape-averaged magneto-conductance (weak localization) is also used for the first time to obtain the electron phase coherence time $\tau_\varphi(T)$ in open ballistic GaAs quantum dots. Values for τ_φ in the range of temperature T from 45 mK to 4 K are found to be independent of dot area, and above 100 mK the dephasing rate τ_φ^{-1} is seen to follow a $A T + B T^2$ temperature dependence. Surprisingly, this agrees quantitatively with the predicted dephasing time for disordered two-dimensional electron systems with effective mean free path on the order of the device size. This suggests that perhaps some Nyquist-type dephasing mechanism is effective in open dots. Measurements of phase coherence times using the weak-localization method for single mode leads were compared and found to be consistent with measurements of $\tau_\phi(T)$ using three other techniques: $\tau_\phi(T)$ obtained from weak localization amplitude at $N = 2$, $\tau_\phi(T)$ extracted from power spectra of UCF, and $\tau_\phi(T)$ extracted from the width of the Lorentzian dip in average conductance around $B = 0$.

Below 100 mK, roll-off from the $A T + B T^2$ dependence is observed. This saturation is not due to inadequate measurement of the electronic temperature, since the device temperature is measured directly from CB peak linewidth and conductance variance.

One possible cause of saturation effects is background radiation in the device environment. To explore this possibility, microwave electromagnetic fields were deliberately coupled to the devices. For several mesoscopic phenomena, including conductance fluctuations, their statistical averages, as well as Coulomb blockade resonance widths, the radiation was shown

to be equivalent to increased cryostat temperature over all powers and frequencies measured. Non-linear Coulomb blockade measurements indicate that the microwave field causes fluctuations of the source-drain voltage, and that the accompanying increase in dephasing is due to Joule heating of transport electrons.

Therefore, microwave coupling does not serve to explain the saturation of the phase coherence time τ_φ at temperatures below 100 mK, twice the electronic base temperature. The saturation of τ_φ remains unexplained.

6.3 Future Directions

This thesis has investigated both the quantum structure and the dephasing properties of open semiconductor quantum dots. These devices have given experimentalists access to a surprisingly rich set of physics and are far from exhausted – future studies may include work in mesoscopic charging [Cronenwett98] and the entanglement and interaction of nearby electron systems [Buks98].

New technologies, such as nanotube growth and scanning probe techniques, will keep advancing our ability to control condensed matter systems at smaller scales. The limit of this work will be the ability to create systems with arbitrary selection of atomic constituents, provided the whole is energetically stable. Smaller size scales will increase quantum level spacings and systems will become more immune to thermal coupling and exhibit long coherence times. The electronic systems studied in this thesis have a fairly short coherence time of a few nanoseconds. Though long enough for interference experiments, more interesting quantum measurement and manipulation experiments are challenging. Although we observe the apparent saturation of dephasing, i.e. maximum phase coherence time in quantum dots, this seems more likely to be an environmental issue than a fundamental issue: to improve coherence, all interactions other than those of interest must be eliminated. Even vacuum fluctuations (and spontaneous emission), the subject of much recent debate in the mesoscopic community, can be suppressed through cavity engineering techniques practiced in the atomic optics and bandgap engineering communities.

Besides electronic wavefunctions, other isolated quantum states in condensed matter systems are electron spin and nuclear spin. The latter states can have very long coherence times, and have led to implementable quantum computing using NMR in naturally occurring molecules [Chuang98]. The ability to make quantum computing useful seems to hinge on

the accessibility of artificial solid state quantum computation, with arbitrary control of huge numbers of deliberately configured quantum states.

In sum, the study of coherence, quantum interaction and quantum measurement in artificial systems is extremely compelling and important. Fortunately it is experimentally accessible— this bodes well for an exciting future for the field.

Appendix A

Nanofabrication

A.1 Fabrication Introduction

Starting with a molecular beam epitaxy (MBE) grown wafer, the basic fabrication procedure developed by myself and by my research group to fabricate quantum dot devices is the following:

1. Cleave small ($\sim 36\mu\text{ m}^2$) peice from wafer.
2. Lithographically pattern and etch mesas to provide inter-device isolation.
3. Pattern and deposit ohmic contacts using optical lithography followed by liftoff and annealing.
4. Pattern gates defining device using multi-stage e-beam lithography.
5. Pattern and deposit bondpads using optical lithography followed by liftoff.
6. Glue chip into chip carrier and bond to devices of interest.

Since our basic process is already very familiar to mesoscopic device community, I won't give an exhaustive process flow here, and will instead describe sub-processes in detail. Samples were fabricated in a small cleanroom “the Microfab” at Ginzton Laboratory, Stanford University.

A.2 Photomask and e-Beam Designs

Figure A.1 shows the patterns that are used to define each step of the fabrication process as outlined above. In our third generation design each device is built on a $800\text{ }\mu\text{m} \times 500\text{ }\mu\text{m}$ mesa, so typically 30-50 devices can be made on a small chip. A photograph of a device in the array is shown in Figure A.2.

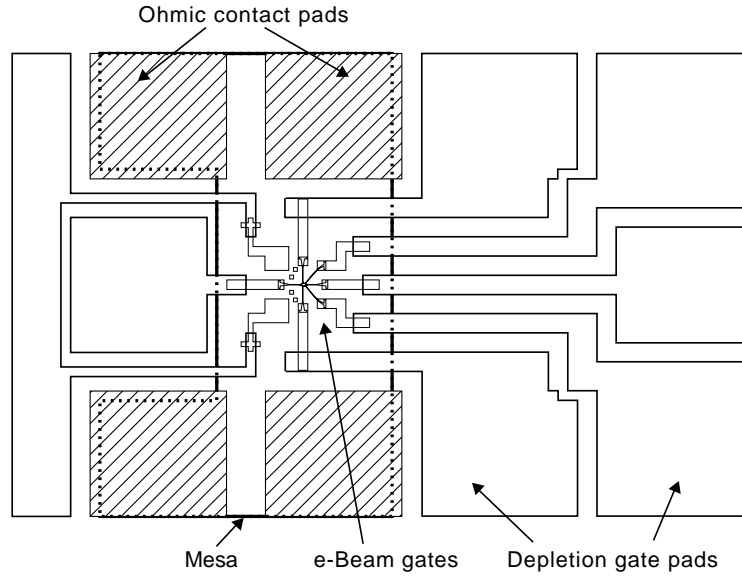


Figure A.1: Design for mesa, ohmic contact and gate patterns superimposed. The order of fabrication is: (1) etch mesa (2) make ohmic contacts (3) make e-beam gates (4) make pads. Electron micrograph of the above as realized on a GaAs/AlGaAs substrate. Mesa footprint is $800\text{ }\mu\text{m} \times 500\text{ }\mu\text{m}$.

A.3 Photolithography

The basic photolithography process is presented below. This process is optimized to be robust and yield an outstanding lip for liftoff. The penalty is a minimum feature size of about $3\text{ }\mu\text{m}$, but this is not important since we do all of the fine metal patterning in the e-beam lithography step (next section). If the develop time is increased past the baseline 1.25 minutes, one can get good patterns all the way to the edge of very small substrates (5-8 mm edge length), without any edge bead removal steps, and with only a slight additional penalty in resolution.

There is a reason liftoff is not often used in industrial fabrication processes: it is not

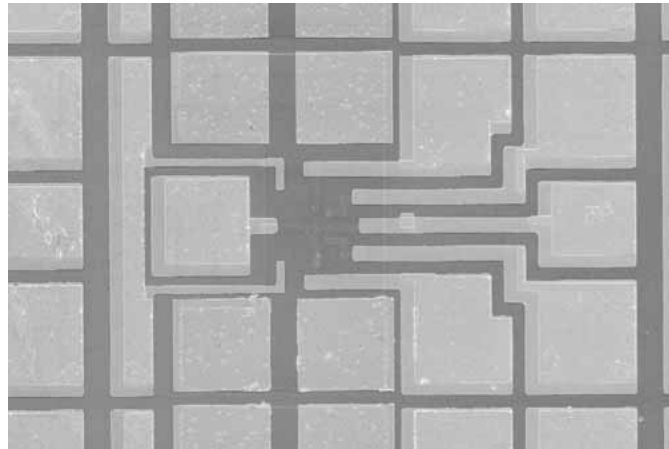


Figure A.2: Electron micrograph of device in Figure A.1 as realized on a GaAs/AlGaAs substrate. Mesa footprint is $800\text{ }\mu\text{m} \times 500\text{ }\mu\text{m}$.

as reliable as deposit-and-etch methods, since there can be poor adhesion of the metal to the substrate and/or tearing. The advantages of liftoff are that no separate etch step is required, and for certain desirable materials, specifically gold where no etch exists that will not damage the GaAs, liftoff is the only method available.

Photolithography Process:

1. Clean chips well with 3-solvent clean: typically boroethane (environmentally safe replacement for TCA and TCE), then acetone, and then methanol, for 5 minutes each, with ultrasound if possible (not always desirable on final bondpad metal process due to sensitive e-beam features).
2. Singe chip on hot plate, or in oven ($120\text{ }^{\circ}\text{C}$) for 5 minutes.
3. Spin Shipley 1813 standard photoresist at 7000 RPM for 30 seconds.
4. Bake at $90\text{ }^{\circ}\text{C}$ on hotplate for 20 minutes.
5. Soak in Chlorobenzene for 15 minutes (this step may be skipped if liftoff is not required, i.e. for the mesa lithography).
6. Bake at $90\text{ }^{\circ}\text{C}$ on hotplate for 5 minutes (may be skipped if liftoff lip is not required).
7. Expose on Karl Süss MB-3 mask aligner for 24 seconds (Power = 16.4) in soft contact mode.

8. Develop using Microposit concentrated developer diluted 1:1 with DI water, for 50 seconds, then in fresh developer for 25 seconds (1:15 total).
9. Oxygen plasma descum (at Ginzton, 50% power, 0.08 seconds).
10. HF dip 20:1 for 15 seconds, then place in N₂ bag and transport to evaporators (at Stanford these are in a separate building).
11. Metal evaporations using Edwards thermal evaporator:
 - (a) Gate metal:
 - 200Å Cr (1 Å/s)
 - 2500Å Au (1-2 Å/s for first 200 Å, then 5-6 Å/s)
 - (b) Ohmic contact metal
 - 50Å Ni (1 Å/s)
 - 1200Å AuGe eutectic (12% Ge by weight)
 - 250Å Ni
 - 1500Å Au
12. Liftoff in acetone; ultrasound should not be required.

A.4 Electron Beam Lithography

There are many variations possible on e-beam lift-off processing, and below is a baseline process. In my final fab iteration (May 1997) I tried both single and double layer PMMA, however with the PMMA weights I used (950K over 495K PMMA) the undercut is not significant, and one effectively has a single layer process. Successful liftoff is achieved by virtue of using a very thin metalization (145Å total) which is perfect adequate for depletion gates (metal resistivity is $\sim 3\Omega/\text{square}$). Using a very low weight PMMA (200K or below) as a lower layer would certainly be an improvement, although this was not tried. On the suggestion of a visiting student from Delft, our group did try using PMMA/MMA co-polymer as a lower layer, which resulted in a huge undercut, of up to $1\mu\text{m}$ as determined by “donut” patterns, and although liftoff is good, problems including shorting between gates and deformation of the patterns were extremely painful and forced us to abandon the co-polymer

process.

e-Beam Lithography Process:

1. Clean chips well with 3-solvent clean (same as for optical steps).
2. Singe on hot plate at 180 C for 2 minutes.
3. Single layer:
 - (a) Spin on 1200Å of 950K PMMA.
 - (b) Bake on hotplate for 30 minutes (+) at 180 C.
4. Double layer:
 - (a) Spin on 550Å of 495K PMMA.
 - (b) Bake on hotplate for 30 minutes at 180 C.
 - (c) Spin on 1100Å of 950K PMMA.
 - (d) Bake on hotplate for 30 minutes (+) at 180 C.
5. Expose at $\sim 240 \mu\text{C}/\text{cm}^2$ with e-beam.
6. Single layer: develop 50 sec in IPA:MIBK 3:1 with 1.3% MEK.
7. Double layer: develop 35 sec in IPA:MIBK 3:1 with 1.3% MEK.
8. Metal evaporation: 25Å Cr, followed by 120Å Au.
9. Liftoff in acetone.

NOTES:

1. The single layer option of the above process shows some proximity effect; this goes away by shortening the develop time at the expense of some tearing.
2. Ultrasound (10 seconds while holding the chip with tweezers in the ultrasound bath) may be used to clear clingy thin metal without damaging features.
3. An HF dip as is customary after optical lithography is not required to achieve good adhesion and leads to a “black halo”, which can’t be good.

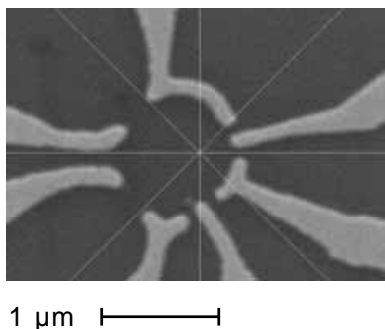


Figure A.3: Example of the e-beam lithography capabilities of the LEO/Nabity system.

A typical quantum dot fabricated with the above process and our converted SEM is shown above in Figure A.3. Since the 2D electron gas is usually at least 100 nm below the surface of the substrate, the lithographic linewidth of ~ 50 nm that we can achieve was adequate. Under the best possible conditions, using a short SEM focal length and perfect exposure dose, we have fabricated 30 nm gold lines.

A LEO/Leica Stereoscan 440 in the Ginzton Microfab (purchased in 1993 for about \$200K) was used to write our e-beam patterns, in conjunction with the Nabity Pattern Generator Systems (or “NPGS”, \sim \$30K, available from J.C. Nabity Lithography Systems). The LEO is a great SEM for taking micrographs, but a rather poor lithography tool when compared to the \sim \$2M Hitachi machine next door at the NSF-funded Stanford Nanofabrication Facility. The main problems with the LEO are poor beam current (exposure dose) control, focus drift, and poor stage resolution (typically 5-10 μ m). I have followed the following procedure to accomodate these deficiencies:

1. The stage is moved sequentially to the writing location for each device as determined by the optical patterns (mesa and ohmics) deposited in previous steps, and the focus is set at the wafer surface. Since the chip is not perfectly flat, the surface plane is calculated from three reference points near the chip corners.
2. At each stage position, the fine patterns for the devices are exposed at high magnification (4400X) and low beam current (typically 60 pA), starting with the outer-most patterns and working in, so that when the actual gates that form the dot are being written, the stage has completely stopped drifting.
3. Finally, a second pass through all of the device positions is made, and large patterns

that connect the fine device lines to the optical bondpads are written at low magnification (400X) and high beam current (10 nA). The high beam current reduced exposure time at the expense of resolution.

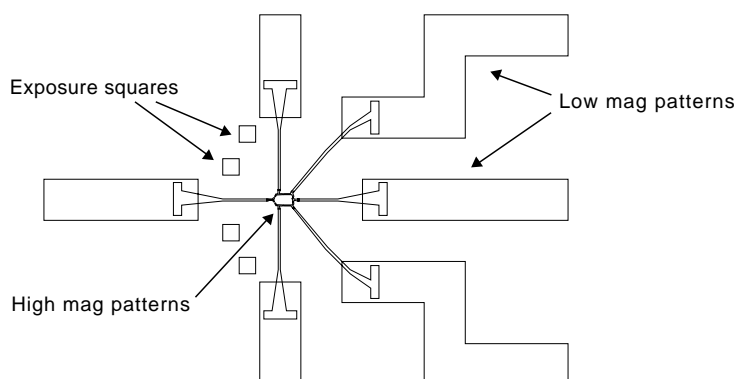


Figure A.4: e-beam patterns. The inner (high magnification) and outer (low magnification) patterns are written in the first and second stage passes respectively.

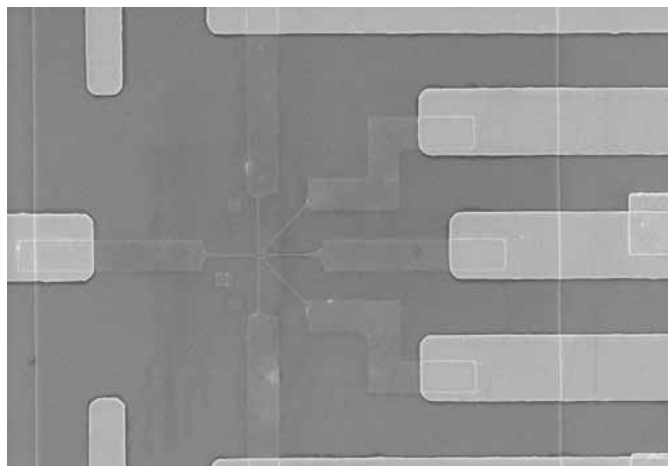


Figure A.5: Electron micrograph of the device showing alignment of optical and e-beam patterns. The mesa width is $150\ \mu\text{m}$.

Figure A.4 shows all of the e-beam patterns written for the typical device; it is an enlargement of the center portion of Figure A.1. Note the set of exposure squares: these were four squares with increasing exposure used to confirm e-beam exposure level. For a normal exposure, two of the squares “clear out” and two remain filled with PMMA. If the beam exposure was significantly too high or low, as indicated by the squares, the PMMA can be rinsed off and lithography repeated before the irreversible metal deposition step.

I wrote special-purpose software to calculate the stage and focus positions, and send the appropriate commands to the SEM via an RS-232 link and issue commands to the NPGS. The Nabity software controls the exposure of each device using two 16-bit D-to-A converters connected to the SEM's deflection plates, and also controls the beak blander. The Nabity system is quite good, and we have very few complaints about it. It would be convenient if the software ran under a more modern operating system than MS-DOS to facilitate networking, and also if it handled GDS Stream input files without conversion. This would allow us to use L-Edit (Tanner Research) to generate all of our lithography patterns, which is superior to the Design CAD program supported by Nabity.

A.5 Ohmic Contacts

The metalization for our ohmic contacts conform to a standard Au-Ni-Ge process with the exact layers given above in section A.2. An Accupulse 410 Rapid Thermal Annealer (RTA) at the Ginzton Microfab is used to anneal the ohmic contacts. The typical temperature and duration of the thermal cycle for good ohmic contacts was 410C for 40 seconds. Typical contact resistances were less than $5k\Omega$ at room temperature, and less than $1k\Omega$ at liquid Helium temperatures.

A.6 Mesa Etching

We use a simple room temperature phosphoric acid wet etch to etch the mesas. Typically about 45 seconds is required to etch down to a 2DEG hetero-interface 100 nm underneath the surface. The exact etch we use is 1 : 8 : 240 ratio mixture of H_2SO_4 : H_2O_2 : H_2O in an ice bath (0C). It is an extremely good idea to use a test peice of GaAs to calibrate the etch exactly each time.

A.7 Packaging and Wire Bonding

We glue the chips into 28-pin ceramic chip carriers, which are non-magnetic (Jade Corp., part 28M270J060U064). Initially, we used silver paint as the "glue" because it is probably a good thermal and electrical conductor to the gold backplane of the chip carrier. This really isn't necessary, however, and recently we have begun to use PMMA since it is much easier to remove (with acetone).

Our wire bonder is a West-Bond Model 5416 ultrasonic wedge bonder. We use 25 μm gold wire (99.99% Au) and a chuck temperature of 140 C.

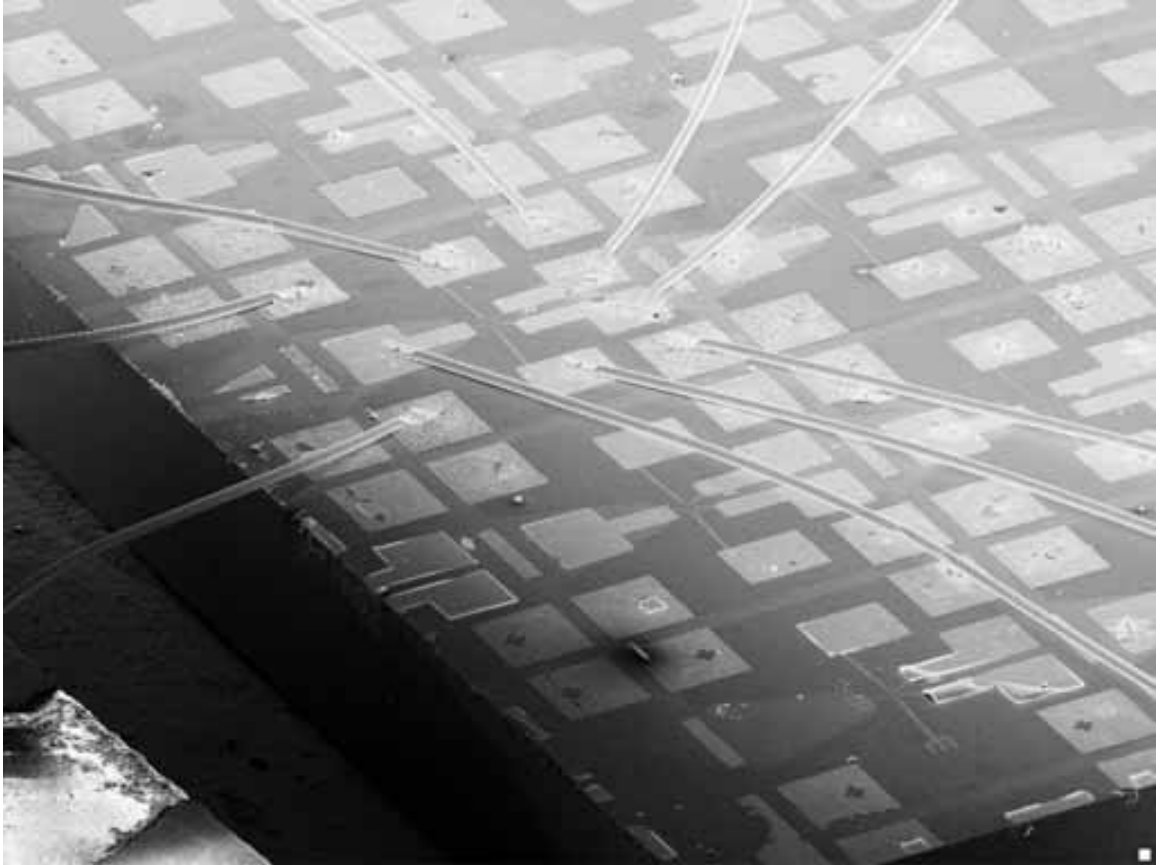


Figure A.6: SEM image of bonded device.

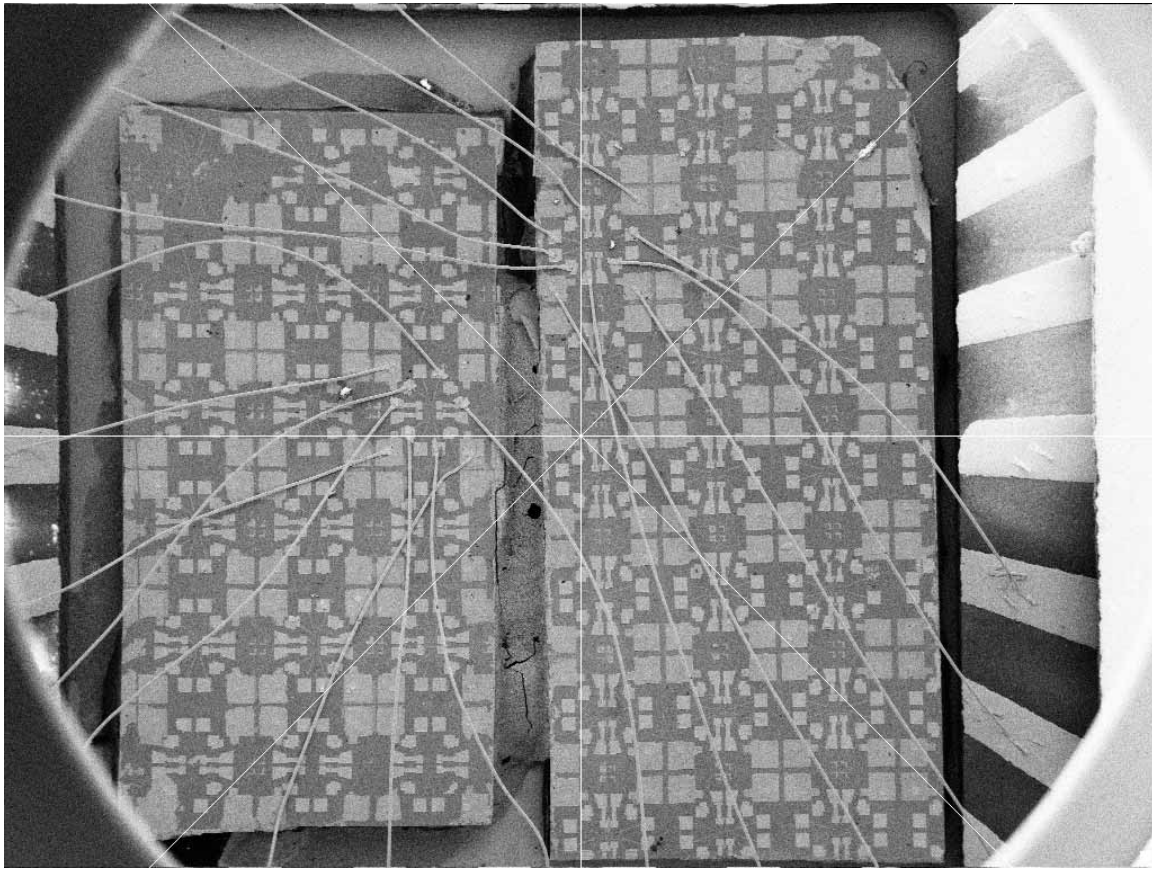


Figure A.7: SEM image of two chips side by side in the ceramic chip carrier cavity with devices wire-bonded. The width of the cavity is 6.85 mm. The circular bounding aperture is the final objective of the SEM.

Appendix B

2D Electron Gases and Devices

B.1 Two-dimensional electron gases

The preferred substrate for most ballistic mesoscopic experiments is a two dimension electron gas (2DEG) formed in a potential well created at a GaAs/Al_xGa_{1-x}As heterointerface. For a range of doping values (typically 1-10¹¹) only the first sub-band (in the z direction) is occupied, and one has a true 2D system. Since GaAs and AlAs have the same crystal structure with almost the exact same lattice constant (GaAs = 5.65Å and AlAs = 5.66Å), an interface with almost no defects may be created when the crystal layers are grown sequentially using molecular beam epitaxy (MBE). In an MBE a flux of the atomic constituents is directed in an ultra-high vacuum ($\simeq 10^{-12}$ torr) at a heated polished substrate. Transport mean free paths of carriers in the 2DEGs exceeding 100 microns have been reported by several groups if the (disordered) dopants are placed away from the interface. For Al composition fraction x less than 0.4, the conduction band minima is in the Γ valley, and there are no conduction subbands. Also, in this regime the band offset is roughly proportional to the mixture ratio x . The effective mass of carriers in the 2DEG's conduction band is $m_* = 0.067 m_e$.

We have fabricated our devices on various substrates from several sources. Of the 16 or so 2DEGs we have tried, only 3 to 4 have worked well for quantum dot devices; two of these were used to make the quantum dots studied in this dissertation. A fundamental problem is switching noise, which can result in a jump in the position of a coulomb blockade peak, or a switch in a coherent conductance level in an open device.

The switching effect is presumably due to thermally activated switching centers. Other

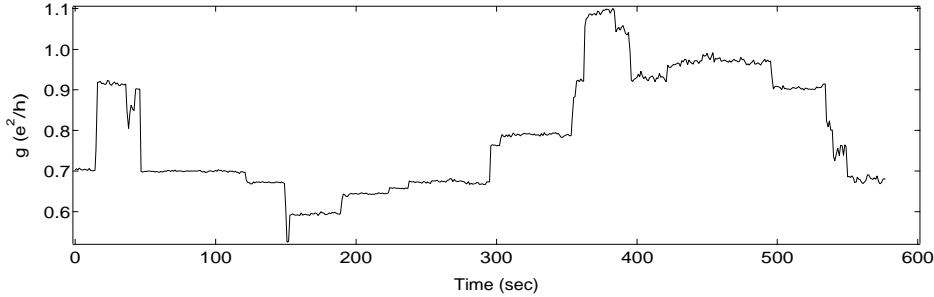


Figure B.1: An example of the effect of a “switcher” on the conductance through a quantum dot which has been biased to support approximately one mode in each quantum point contact.

secondary failure mechanisms include poor ohmic contacts, and low mobility (and thus bad quantum point contacts) resulting from crystal defects, and non-uniform 2DEG density.

GaAs/AlGaAs substrates containing 2DEGs grown by many different groups share similar design characteristics. A superlattice smoothes substrates defects, and traps impurities. This is followed by a GaAs buffer layer, followed by the GaAs/Al_xGa_{1-x}As layer. The 2DEG is formed between these two layers. After this more GaAs/Al_xGa_{1-x}As containing silicon (n-type) dopants is deposited, followed by a cap layer of GaAs is used as a passivation layer (AlGaAs will oxidize in air). A diagram of the entire structure is shown in Figure B.2.

One usually wishes to make the 2DEG as close to the surface as possible so that it may be more finely controlled with surface depletion gates, however to keep the mobility high the 2DEG must be substantially separated from the doping layer. A detailed review of these types of considerations may be found in [Melloch93].

B.1.1 Wafer CEM2385

This substrate was grown by Cem Duruöz, a member of the Harris group at Stanford University. The growth profile for the wafer is shown below. The doping is uniform in the upper AlGaAs layer (rather than delta-doped, where all of the dopants are placed in one layer). The carrier density measured with a Hall bar was $2.0 \times 10^{11} \text{ cm}^{-2}$. I measured the cyclotron radius with the QPCs very open (5-6 channels) and estimate the density to be $2.8 \times 10^{11} \text{ cm}^{-2}$ in device C1. It is interesting to note that Yacoby *et al.* also reported a Fermi energy (proportional to density) using focusing measurements that was higher than that found using Shubnikov-de Haas measurements. The mobility was measured to be $140,000 \text{ cm}^2 \text{ Vs}$.

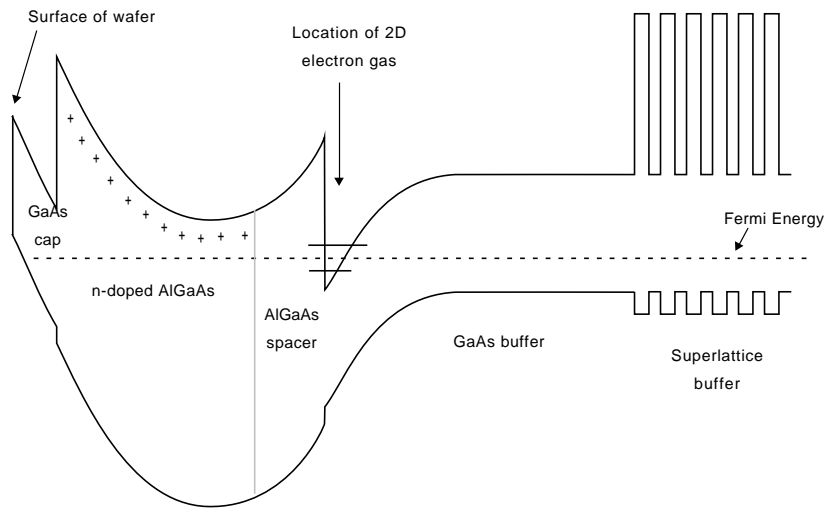


Figure B.2: Substrate band diagram showing layers and position of 2DEG.

100Å	GaAs
400Å	$\text{Al}_x\text{Ga}_{1-x}\text{As}$ $x = 0.34$ $n(\text{Si}) = 1.0 \times 10^{18} \text{cm}^{-3}$
400Å	$\text{Al}_x\text{Ga}_{1-x}\text{As}$ $x = 0.34$
10000Å	GaAs
500Å	$\text{Al}_x\text{Ga}_{1-x}\text{As}$ $x = 0.34$
13000Å	Superlattice: 100Å $\text{Al}_x\text{Ga}_{1-x}\text{As}$ & 30Å GaAs, $x = 0.34$, 100 periods
3000Å	GaAs
substrate is semi-insulating GaAs	

B.1.2 Wafer 940708A

This substrate was grown by Ken Campman, with Art Gossard's group at UCSB. This 2DEG was grown at 640 C.

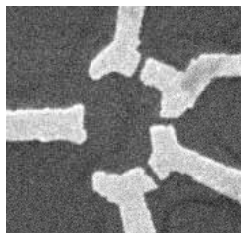
This 2DEG is located 160 nm below the surface of a GaAs/Al_{0.3}Ga_{0.7}As heterostructure with sheet density $n = 1.8 \times 10^{11} \text{cm}^{-2}$, mobility $\mu = 1.0 \times 10^6 \text{cm}^2 \text{Vs}$, Fermi wavelength $\lambda_F = 60 \text{nm}$ and Fermi energy $E_F = 6.4 \text{meV}$.

100Å	GaAs
1000Å	$\text{Al}_x\text{Ga}_{1-x}\text{As}$ $x = 0.30$
	delta dopant layer, Si: $2.5 \times 10^{12}\text{cm}^{-2}$
500Å	$\text{Al}_x\text{Ga}_{1-x}\text{As}$ $x = 0.30$
8000Å	GaAs
3000Å	Superlattice: $\text{Al}_x\text{Ga}_{1-x}\text{As}$ / GaAs, $x = 0.30$
3000Å	GaAs
	substrate is semi-insulating GaAs

B.2 Device Inventory

The following devices “passed the test” and produced published data during this research:

B.2.1 Dots I613, I75

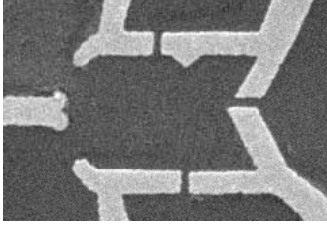


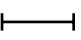
1 μm 

Area = $0.4 \mu\text{m}^2$

2DEG = 940708A

Experiment = He-3 Dephasing (both dots)

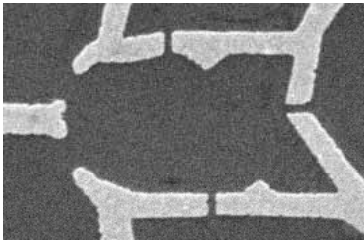
B.2.2 Dot I77

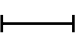
1 μm 

Area = $1.9 \mu\text{m}^2$

2DEG = 940708A

Experiment = He-3 Dephasing

B.2.3 Dot I74

1 μm 

Area = $4.0 \mu\text{m}^2$

2DEG = 940708A

Experiment = He-3 Dephasing

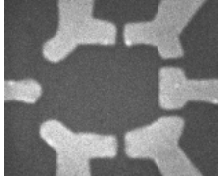
B.2.4 Dot C14

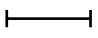
For picture, see Figure 2.2 (right device).

Area = $0.5 \mu\text{m}^2$

2DEG = CEM2385

Experiment = Dilution fridge distributions

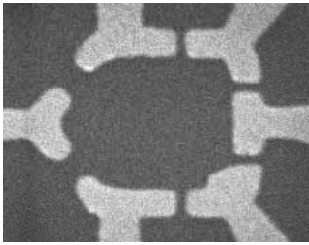
B.2.5 Dot C79, C63

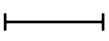
1 μm 

Area = $1.0 \mu\text{m}^2$

2DEG = CEM2385

Experiment = Dilution fridge distributions (C79), CB Radiation (C63)

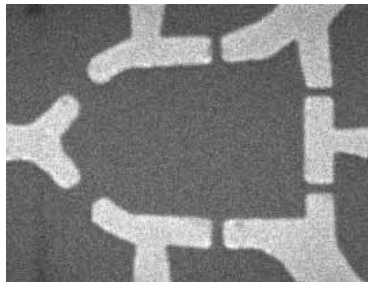
B.2.6 Dot C22

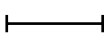
1 μm 

Area = $1.6 \mu\text{m}^2$

2DEG = CEM2385

Experiment = Dilution fridge dephasing

B.2.7 Dots C32, C70

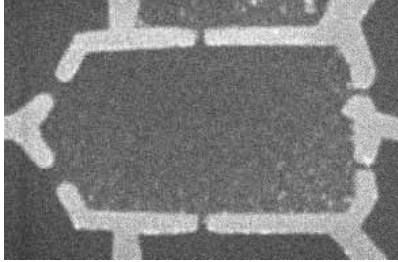
1 μm 


Area = $3.0 \mu\text{m}^2$

2DEG = CEM2385

Experiment = Dilution fridge dephasing (both dots), N=1 Radiation (C70)

B.2.8 Dots C88, C15



1 μm 

Area = $8.0 \mu\text{m}^2$

2DEG = CEM2385

Experiment = Dilution fridge dephasing

Appendix C

Cold Filter

C.1 Motivation

There is much research activity focused on measuring the electronic properties of artificial devices at low temperatures. Typically a dilution refrigerator, capable of reaching temperatures down to ~ 10 mK, is employed to cool the devices and associated wiring. Unfortunately, the effective temperature of the electrons traveling through the device never reaches the temperature of the coldest portion of the dilution refrigerator (the mixing chamber base plate). This can be due to the coupling of environmental radiation into the device under test and also imperfect thermal sinking of the wiring.

We have constructed a cryogenic filter which aims to eliminate these sources of heating by running all electrical wiring going to the sample through a cold low-pass filter. The filter and accompanying shielding provide good thermal sinking as well as protection from the external electromagnetic environment (environmental radiation).

On a Kelvinox dilution refrigerator with a base temperature of 25 mK, the filter is capable of reducing the electron temperature from 95 mK (no shielding) to approximately 42 mK, as measured in our GaAs/AlGaAs devices.

C.2 Technical Description

The filter unit is attached to the base plate of the refrigerator. The sample wiring (we use standard 40-gauge copper magnet wire) is first wrapped around a solid copper spindle to provide an initial thermal anchor, and then enters the filter through a pair of connectors

with gold-plated pins (see Figure C.1). The wiring in the enclosed filter cavity is extremely thin: we use 20 micron thick wire with 5 micron thick insulation (California Fine Wire Co., Stableohm 800A). Approximately 13 feet of this wire is wrapped non-inductively in the cavity, which is then back-filled with conductive epoxy containing silver powder (Epoxy Technology, #410E). Somewhat amazingly, there are very few shorts to the epoxy with wire from this vendor. We did however have many wires break for unknown reasons, and it is good to have spares. It is also a good idea to have very deliberate plans for handling the fine wire when assembling the filter unit. Steve Grossman (who worked many late nights on the filter during summer 1997) and I ended up soldering and then silver-painting (tin-lead solder superconducts at low temperatures) the fine wire to the connectors and then wrapping the thin wire, silver-painted together into a single cable, around a copper spool that we placed in the filter cavity prior to epoxy backfill. The filter has been thermally cycled about 30 times with few new breaks or shorts; apparently there are no severe thermal expansion mismatch issues!

The filter housing is machined from a solid block of copper, which is connected to the mixing chamber base plate with a copper L-bracket. Clean copper surfaces screwed together tightly insure a good thermal connection. RF leaks due to connector air gaps are filled with indium gaskets.

The thin wires strung through the epoxy make an excellent distributed low pass RC filter, with a roll-off at ~ 500 kHz. Below the filter, all wiring and the device under test is fully encapsulated by gold-plated copper or bronze shielding.

C.3 Advantages over other methods

Presently most research groups involved in cryogenic electronics research have employed “copper powder” filters. These filters, in which the leads traverse through a cell filled with epoxy containing surface-oxidized copper particles, absorb high frequency radiation by virtue of the large effective surface area of the copper particles and the short skin depth. These filters are described by [Martinis87]. However, even with multiple stages, the lowest claimed electronic temperatures are about ~ 60 mK on the typical dilution refrigerator setup.

The only additional filtering in our system is a simple RC filter (with a typical low-pass roll-off of 10 Hz) following the D-to-A converters for the gates and also “ π ” filters (Spectrum Controls Inc., part #SCI-56-705-001, with a ~ 50 MHz roll-off), placed inline with respect

to the sample wiring as it enters the cryostat. The π filters are standard parts used to eliminate unwanted RF noise from communications circuits.

The filter system described about is presently being implemented by other research labs.

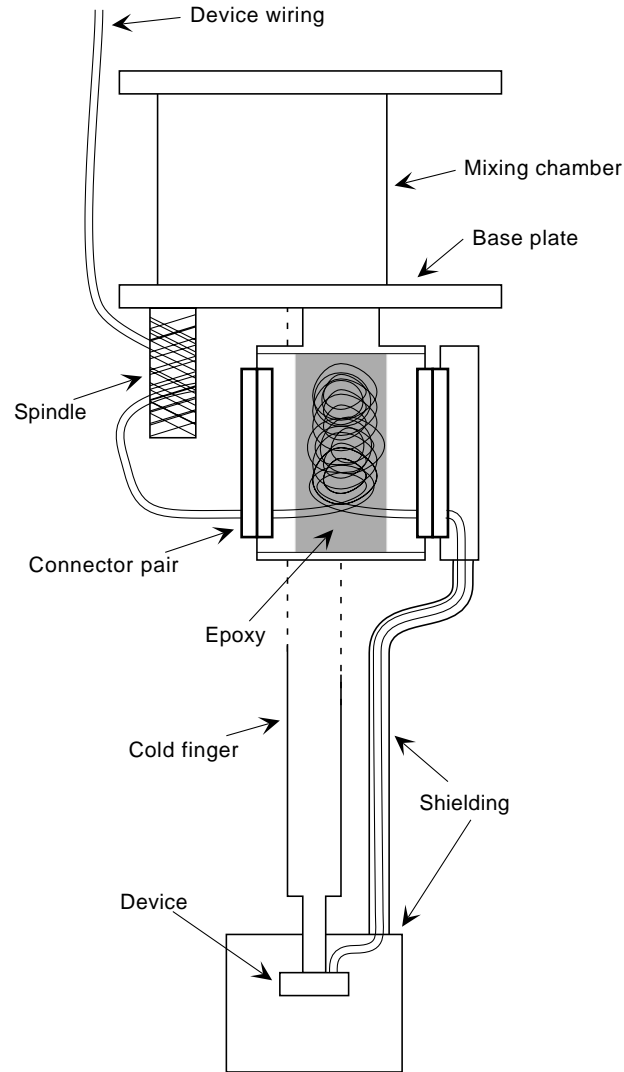


Figure C.1: Filter unit and cold finger of dilution refrigerator.

Appendix D

Measurement System

D.1 Cryostats

Sorption-pumped ^3He and dilution refrigerator cryostats were used to perform the measurements in this thesis. Both of these systems are located in the Varian Building Room 153 (Physics Department, Stanford University). A detailed description of these systems which are both fairly new (purchased in 1993 and 1994) can be found in the Oxford Instruments documentation.

The “high temperature” measurements of Chapter 3 were performed using an Oxford Instruments Heliox 2^{VL} ^3He sorption-pumped insert, which has a base temperature of approximately 300 mK. No special electrical filtering, except for inline “ π ” filters (Spectrum Controls Inc., part #SCI-56-705-001, ~ 50 MHz roll-off) was used in the experiment wiring. The single-sorption-pump design often made it difficult to do temperature sweeps due to the poor feedback control and the limited lifetime of the ^3He pot, but it was adequate. On our Heliox system, the temperature controller was initially measuring the system RuO_2 resistor with too high of a probe current, heating it. This is a lesson that one should fully understand the equipment one is using even if it bought packaged from a vendor.

The dilution refrigerator used for low temperature measurements in this thesis was an Oxford Instruments Kelvinox with a base temperature of ~ 28 mK measured using an RuO_2 resistor, and an electronic base temperature of ~ 45 mK. The special filtering effort that went into the wiring on this cryostat are described in Appendix C. The dilution refrigerator was operated in a shielded room although opening and closing the door to the shielded room was never observed to have any effect.

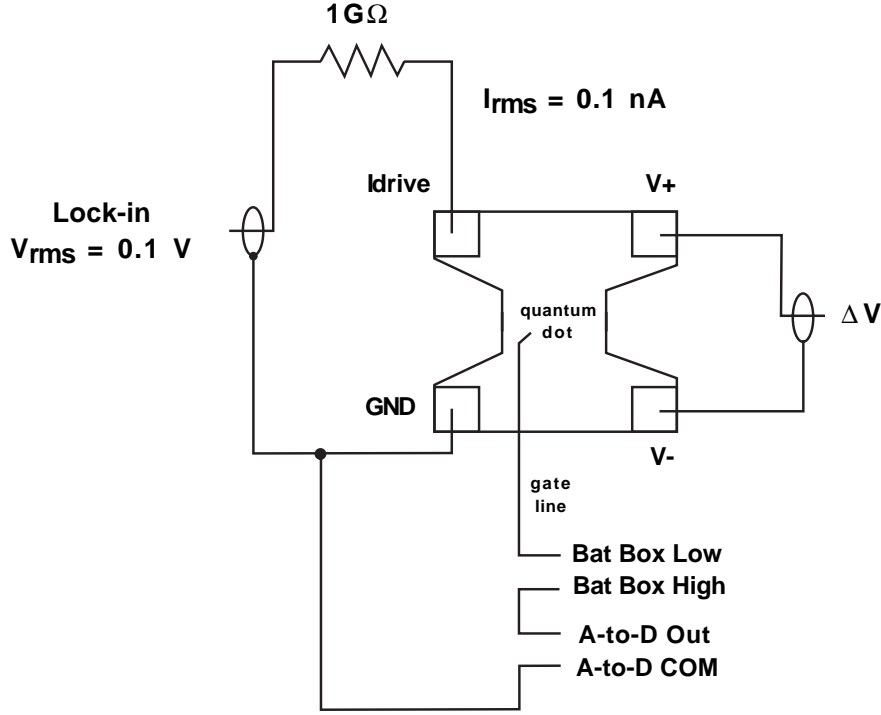


Figure D.1: Connection diagram for four-wire current bias mode of operation.

D.2 Measurement Configurations

The most common configuration for the measurements performed in this thesis was the four-wire constant-current bias configuration shown in Figure D.1. Given that a known constant current is passing through the quantum dot, the voltage across the device precisely determines the resistance and conductance. Typically the resistance of the device is near or below $\sim 25 \text{ K}\Omega$ (average conductance e^2/h and above). A potential problem with this configuration is that if the resistance becomes very high (due to for example destructive quantum interference), the voltage across the device rises potentially heating the device and changing the conductance. This is the case for distribution measurements, where a different type of 4-wire measurement was used, shown in Figure D.5. However, in most measurements, there is enough thermal smearing and/or dephasing that the resistance remains near the average. As long as the source-drain drive voltage is within $\sim 2 \text{ kT}$, heating is minimal (see Section 3.3).

As indicated in Figure D.1, each gate is driven in by a battery-powered bias box and an

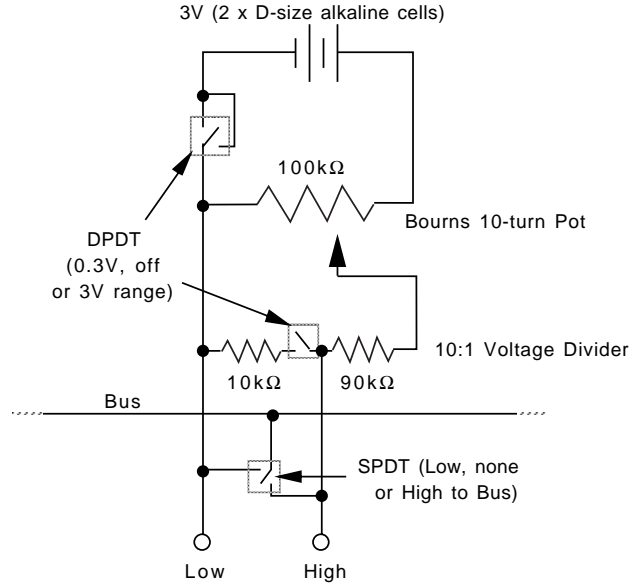


Figure D.2: Battery box circuit (drawing by Ian Chan).

A-to-D converter channel in series. The battery-operated voltage source is a simple circuit based on a potentiometer, as shown in Figure D.2.

Typically, an A-to-D converter (a National Instruments 10-bit 6-channel AO6 board was used) is also placed in line to allow computer control. In these experiments connecting the computer A-to-D lines to the experiment was never observed to change noise or ground properties of the system. The A-to-D lines are filtered with a low pass RC filter. A differential amplifier between the computer and the experiment (shown in Figure D.3) was installed to reduce grounding problems. The electronics described in this section was used in both cryostats.

D.3 General Observations

Several approaches that constitute good measurement practice were followed in these experiments and are enumerated here.

1. A spectrum analyzer was connected to the output of all pre-amps to check for noise source (60 Hz and harmonics are the usual suspects) and to make sure that there is a low noise floor at the measurement frequency.

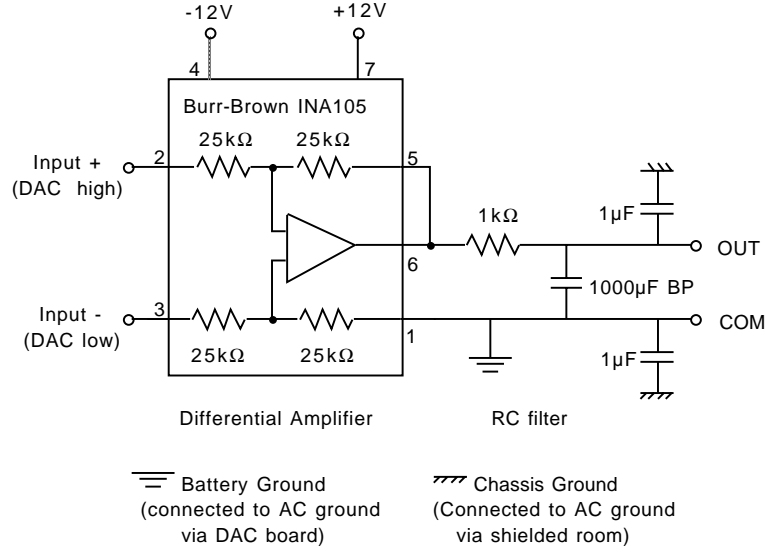


Figure D.3: Differential amplifier circuit (drawing by Ian Chan).

2. All computer connections were disconnected to determine their effect on noise and on measurement.
3. The grounding configuration and the possibility of ground loops was considered. For example, the shield of the output of the lock-in amplifiers used (PAR 124A's) is actually not at ground but is oscillating at a few μV .
4. Inline resistors of at least 350Ω seemed to prevent electrostatic destruction of the devices due to influx of charge onto gates.

D.4 High-resistance Measurements

For high-resistance Coulomb blockade measurements, the standard measurement configuration is shown in Figure D.4. The lock-in now provides a constant voltage source and the current is measured to determine conductance. The current pre-amplifier used is an Ithaco Model 1211. The voltage is always below a known maximum level which prevents heating.

In order to measure the conductance accurately for the configuration of Figure D.4, a set of voltage probes is added to the configuration, so that there is an independent measure of both current and voltage, as seen in Figure D.5. This capability enabled measurement

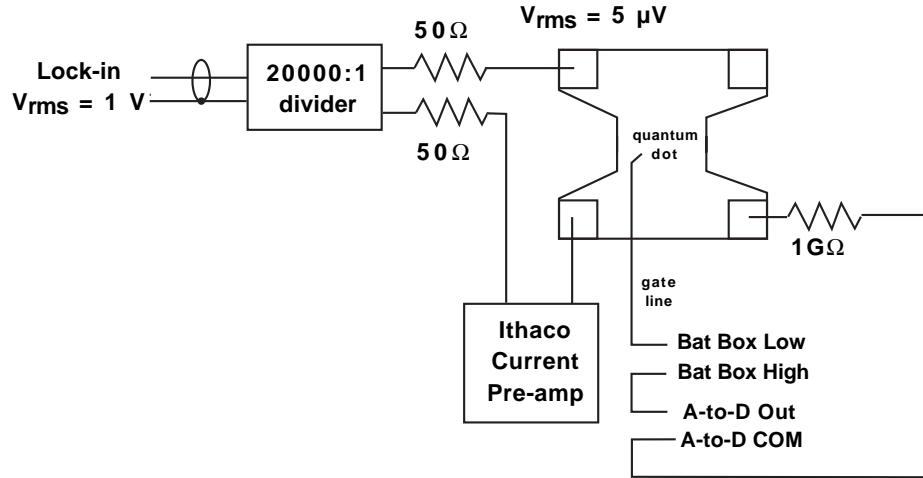


Figure D.4: Connection diagram for voltage bias mode of operation.

of conductance distributions for $N = 1$ quantum dots.

D.4.1 Combined AC/DC Measurements

For the nonlinear Coulomb blockade measurements, it was necessary to measure the small signal ac response of the device on top of a changing dc bias. In this case, the dc source was an AO6 channel with a voltage divider, and the ac signal of the lock-in is coupled on top of the dc using a passive network (a resistor and two capacitors) with appropriate values. Active electronics could also be used but could result in along noise and grounding problems.

D.5 Software

Igor Pro from Wavemetrics, Inc. (<http://www.wavemetrics.com>) was the software core of the measurement system. Igor is a fantastic program for scientific data analysis, graphing and also data acquisition. Historically it has run only on the Mac but recently you one also get a very nice version for MS Windows machines.

Using low-level software modules written by myself and other students that interface to a GPIB card and dual 6-channel 10-bit programmable-range D-to-A cards (National Instruments AO6), Igor is able to do all data acquisition functions for an experiment. The user interface is command-line driven, but the interpreted programming environment

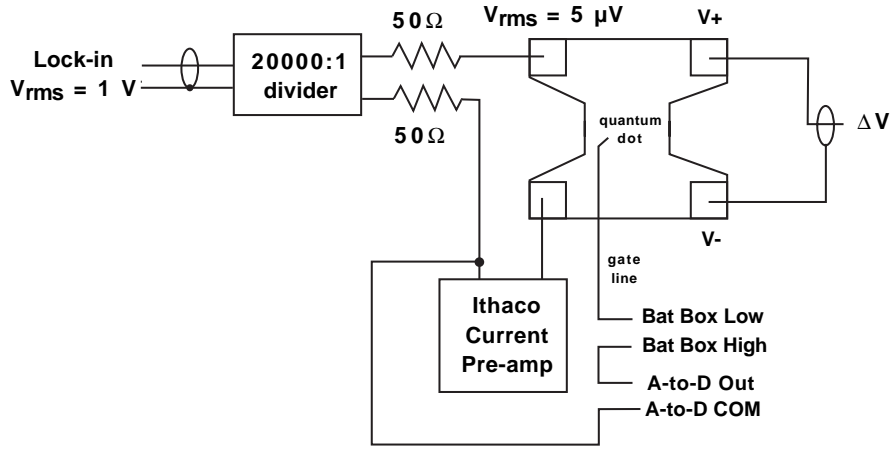


Figure D.5: Connection diagram for voltage bias, V and I measuring mode.

is easy to use. The ability to quickly make and manipulate very sophisticated graphs immediately after data-acquisition makes Igor very useful. The graphical output, including 3D visualization, is up to scientific publication requirements. My only criticism of the Igor system is its restriction that all working data is loaded in memory, as opposed to stored on disk in a database. Perhaps this will be improved in a future version.

Appendix E

Non-linear Coulomb Blockade Model

E.1 Description

In order to better understand the effect of source-drain fluctuations on the non-linear response of a quantum dot in Coulomb blockade, a short simulation was coded in Igor. The basic idea is that the ideal thermal non-linear CB diamonds are smeared (convolved) with an arbitrary trajectory in $V_{\text{gate}} - V_{\text{SD}}$ space. The trajectory may simply be a sinusoidally changing V_{SD} , representing pure source-drain fluctuations, or a combined effect, where V_{gate} is also fluctuating at the same or even a harmonic frequency, with a possible phase lag.

In designing the model I have attempted to follow good numerical recipe practice and have slightly over-quantized. Non-linear responses which are shifted in $V_{\text{gate}} - V_{\text{SD}}$ space are linearly interpolated from (0,0). The approach is a reasonable compromise between taking too long and getting the wrong answer, but one has to be attentive to the level of discretization.

Figure E.1 shows an effort to match at experimentally measure Coulomb blockade diamond with a simulation in which the source-drain and gate voltages are driven at harmonic frequencies (black dots show drive "trajectory").

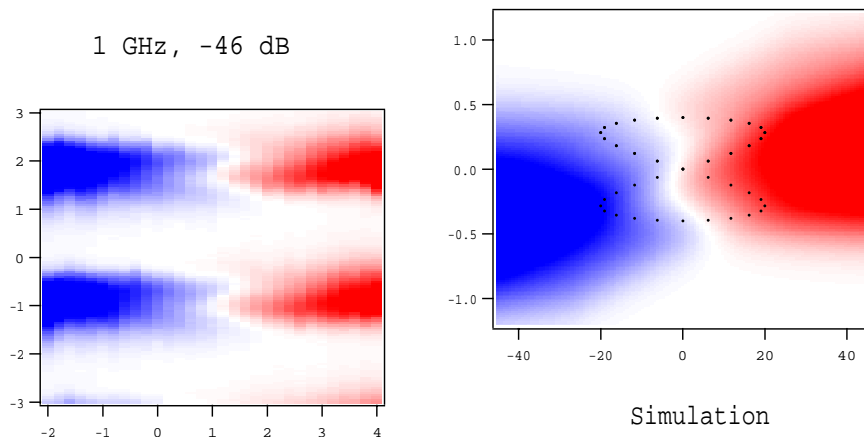


Figure E.1: Measured non-linear Coulomb blockade diamonds and example simulation.

E.2 Source Code

A version of the source code is reproduced below. Feel free to contact the author by e-mail (andy@alumni.princeton.edu) with any questions.

```
// function for zero temp CB diamonds
function cbzero(vg,vsd)
    variable vg,vsd
    variable i,j,k,x,y,vl,vr

    variable al = -300
    variable ar = 120
    variable delta = 40

    variable mod = -1
    if (vsd<0)
        vsd *= -1
        vg *= -1
        mod = 1
    endif
    vl = vsd-al*vg
    vr = vsd-ar*vg
```

```

        if ((vl>0) %& (vr>0))
            return mod*(floor(vl/(delta*(-al)/ar))
                        +floor(vr/delta)+2)
        endif
    return 0
end

// convolves cbgrid into cbsmear to simulate radiation drive
macro cbadd(magvsg,magvg)
    variable magvsg,magvg
    silent 1;pauseupdate
    make/o /n=60 wavesd,waveg
    variable n = numpnts(wavesd)

    waveg = magvg*sin(6*pi*p/n) //+0.3*magvg*cos(2*pi*p/n)
    wavesd =magvsg*sin(6*pi*p/n)

    duplicate /o cbgrid cbsmear
    variable i = 0
    do
        cbsmear += cbgrid(wavesd[i]+x)(waveg[i]+y)
        i+=1
    while (i<n)
    cbsmear *= 1/n
end

// generates finite temp CB diamonds in array cbgrid
function cbgen(temp)
    variable temp
    variable vg,vsg
    variable i,j,k,x,y,vl,vr

    variable al = -160
    variable ar = 80
    variable delta = 7.046 / 1.6
    variable mod = -1

    WAVE cbgrid=cbgrid
    WAVE twave=twave
    cbgrid = 0
    redimension /n=(dimsize(cbgrid,1)) twave
    make /o/n=(dimsize(cbgrid,1)) cbrow

```

```

print dimsize(cbgrid,0),dimsize(cbgrid,1)

SetScale/I x -10,10,"", twave
// thermal weighting function
twave = 1 / ( Cosh( (p-150)/3/temp )^2 )
rotate 150,twave
wavestats /q twave
twave /= numpnts(twave)*V_avg*2

j = 0
do
    vsd = dimoffset(cbgrid,0)+j* dimdelta(cbgrid,0)
    i=0;  cbrow = 0
    do
        vg = dimoffset(cbgrid,1)+i* dimdelta(cbgrid,1)
            //-vgoffset
        mod = 1
        if (vsd<0)
            mod = -1
        endif
        vl = mod*(vsd-al*vg)
        vr = mod*(vsd-ar*vg)
        if ((vl>0) %& (vr>0))
            cbrow[i] =-mod*(floor(vl/(delta*(-al)/ar))
                +floor(vr/delta)+2)
        endif
        i+=1
    while (i<dimsize(cbgrid,1))
    convolve /c twave,cbrow
    cbgrid[j][]=cbrow[q]
    j+=1
while (j<dimsize(cbgrid,0))
end

```


Bibliography

- [Akis97] R. Akis, D. K. Ferry, and J. P. Bird, “Wave function scarring effects in open stadium shaped quantum dots,” *Phys. Rev. Lett.*, **79**, 123-6 (1997).
- [Aleiner96] I. L. Aleiner and L. Glazman, “Quantum Coulomb Blockade in Chaotic Systems,” preprint cond-mat/9612138 (1996).
- [Aleiner97] I. L. Aleiner, Ned S. Wingreen, and Yigal Meir “Dephasing and the Orthogonality Catastrophe in Tunneling through a Quantum Dot: The ‘Which Path?’ Interferometer,” *Phys. Rev. Lett.* **79**, 3740 (1997).
- [Aleiner98a] I. Aleiner and L. Glazman, “Mesoscopic charge quantization,” *Phys. Rev. B* **57**, 9608 (1998).
- [Aleiner98b] I.L. Aleiner, B.L. Altshuler, and M.E. Gershenson, “Interaction effects and phase relaxation in disordered systems”, cond-mat/9808053 (1998).
- [Altshuler81] B. L. Altshuler, A. G. Aronov, and D. E. Khmelnitsky, “Suppression of Localization Effects by the High Frequency Field and the Nyquist Noise,” *Solid State Comm.* **39**, 619 (1981).
- [Altshuler82] B. L. Altshuler, A. G. Aronov, and D. E. Khmelnitsky, “Effect of Electron-Electron Collisions with Small Energy Transfer on Quantum Localization,” *J. Phys. C* **15**, 7367 (1982).
- [Altshuler85] B. L. Altshuler and A. G. Aronov, “Electron-Electron Interaction in Disordered Conductors,” in *Electron-Electron Interaction in Disordered Systems*, edited by A. L. Efros and M. Pollak (Elsevier, Amsterdam, 1985).
- [Altshuler95] B. L. Altshuler and B. D. Simons, “Universalities: From Anderson Localization to Quantum Chaos,” in *Mesoscopic Quantum Physics*, edited by G. M. E. Akkermans, J.-L. Pichard and J. Zinn-Justin (Elsevier, Amsterdam, 1995).

- [Altshuler97] B. Altshuler, Y. Gefen, A. Kamenenev, and L. Levitov, "Quasiparticle Lifetime in a Finite System: A Nonperturbative Approach," *Phys. Rev. Lett.* **78**, 2803 (1997).
- [Altshuler98] B.L. Altshuler, M.E. Gershenson, and I.L. Aleiner, "Phase Relaxation of Electrons in Disordered Conductors", *cond-mat/9803125* (1998).
- [Andreev96] A. V. Andreev, O. Agam, B. D. Simons, and B. L. Altshuler, "Quantum Chaos, Irreversible Classical Dynamics, and Random Matrix Theory," *Phys. Rev. Lett.* **76**, 3947 (1996).
- [Argaman93] N. Argaman, Y. Imry, and U. Smilansky, "Semiclassical analysis of spectral correlations in mesoscopic systems," *Phys. Rev. B* **47**, 4440 (1993).
- [Baranger92] H. U. Baranger, R. A. Jalabert, and A. D. Stone, "Quantum Interference in Ballistic Cavities: Conductance Fluctuations and Weak Localization," in *Transport Phenomena in Mesoscopic Systems*, edited by H. Fukuyama and T. Ando (Springer-Verlag, New York, 1992).
- [Baranger93a] H. U. Baranger, R. A. Jalabert, and A. D. Stone, "Weak Localization and Integrability in Ballistic Cavities," *Phys. Rev. Lett.* **70**, 3876 (1993).
- [Baranger93b] H. U. Baranger, R. A. Jalabert, and A. D. Stone, "Quantum-chaotic scattering effects in semiconductor microstructures," *Chaos* **3**, 665 (1993).
- [Baranger93c] H. U. Baranger, R. A. Jalabert, and A. D. Stone, "Quantum Conductance of Ballistic Cavities: Weak-Localization, Conductance Fluctuations, and Chaos," *Surf. Sci.* (1993).
- [Baranger94a] H. U. Baranger and P. A. Mello, "Mesoscopic Transport Through Ballistic Cavities: A Random S-Matrix Theory Approach," *Phys. Rev. Lett.* **73**, 142 (1994).
- [Baranger94b] H. U. Baranger and P. A. Mello, "How phase-breaking affects quantum transport through chaotic cavities," *Phys. Rev. B* **51**, 4703 (1994).
- [Baranger95] H. U. Baranger and P. A. Mello, "Effect of phase breaking on quantum transport through chaotic cavities", *Phys. Rev. B* **51**, 4703 (1995).
- [Baranger96a] H. U. Baranger and P. A. Mello, "Short paths and information theory in quantum chaotic scattering: transport through quantum dots," *Europhysics Lett.* **33**, 465 (1996).
- [Baranger96b] H. U. Baranger and P. A. Mello, "Reflection symmetric ballistic microstructures: quantum transport properties," *Phys. Rev. B* **54**, R14297 (1996).

- [Beenakker90] C. W. J. Beenakker and H. van Houten, "Semi-classical Theory of Magnetoresistance Anomalies in Ballistic Multi-probe Conductors," in *Electronic Properties of Multilayer and Low-Dimensional Semiconductor Structures*, edited by L. E. a. J. C. P. J. M. Chamberlain (Plenum, London, 1990).
- [Beenakker91a] C. W. J. Beenakker and H. van Houten, "Quantum Transport in Semiconductor Nanostructures," in *Solid State Physics*, vol. 44, edited by H. Turnbull (Academic Press, San Diego, 1991).
- [Beenakker91b] C. W. J. Beenakker and H. van Houten, "Semiclassical theory of shot noise and its suppression in a conductor with deterministic scattering," *Phys. Rev. B* **43**, 12066 (1991).
- [Beenakker91c] C. W. J. Beenakker, "Theory of Coulomb-blockade oscillations in the conductance of a quantum dot," *Phys. Rev. B* **44**, 1646 (1991).
- [Beenakker92a] C. W. J. Beenakker and A. A. M. Staring, "Theory of the thermopower of a quantum dot," *Phys. Rev. B* **46**, 9667 (1992).
- [Beenakker92b] C. W. J. Beenakker and M. Büttiker, "Suppression of shot noise in metallic diffusive conductors," *Phys. Rev. B* **46**, 1889 (1992).
- [Beenakker92c] C. W. J. Beenakker and M. Büttiker, "Suppression of shot noise in metallic diffusive conductors," *Phys. Rev. B* **46**, 1889 (1992).
- [Beenakker93a] C. W. J. Beenakker, "Random-matrix theory of mesoscopic fluctuations in conductors and superconductors," *Phys. Rev. B* **47**, 15763 (1993).
- [Beenakker93b] C. W. J. Beenakker, "Brownian-motion model for parametric correlations in the spectra of disordered metals," *Phys. Rev. Lett.* **70**, 4126 (1993).
- [Beenakker93c] C. W. J. Beenakker, "Universality in the Random-Matrix Theory of Quantum Transport," *Phys. Rev. Lett.* **70**, 1155 (1993).
- [Beenakker94a] C. W. J. Beenakker and B. Rejaei, "Exact solution for the distribution of transmission eigenvalues in a disordered wire and comparison with random-matrix theory," *Phys. Rev. B* **49**, 7499 (1994).
- [Beenakker94b] C. W. J. Beenakker, "Universality of weak localization in disordered wires," *Phys. Rev. B* **49**, 2205 (1994).
- [Beenakker94c] C. W. J. Beenakker and B. Rejaei, "Random-matrix theory of parametric correlations in the spectra of disordered metals and chaotic billiards," *Physica A* **203**, 61 (1994).
- [Beenakker97] C. W. J. Beenakker, "Random-Matrix Theory of Quantum Transport," *Rev. Mod. Phys.* **69**, 741 (1997).

- [Bird90] J. P. Bird, A. D. C. Grassie, M. Lakrimi, K. M. Hutchings, J. J. Harris, and C. T. Foxon, "Conductance fluctuations and non-diffusive motion in GaAs/AlGaAs heterojunction wires," *J. Phys. Cond. Matter* **2**, 7847 (1990).
- [Bird92] J. P. Bird, A. D. C. Grassie, M. Lakrimi, K. M. Hutchings, P. Meeson, J. J. Harris, and C. T. Foxon, "Coherence limiting length scale in ultra high mobility GaAs/AlGaAs heterojunction wires," *Surface Science* **267**, p. 277 (1992).
- [Bird94a] J. P. Bird, K. Ishibashi, Y. Aoyagi, T. Sugano, and Y. Ochiai, "Spectral characteristics of conductance fluctuations in ballistic quantum dots," *Phys. Rev. B* **50**, p. 18678 (1994).
- [Bird94b] J. P. Bird, K. Ishibashi, Y. Aoyagi, and T. Sugano, "Giant backscattering resonances in the magneto-resistance of GaAs/AlGaAs quantum dots," *Superlattices and Microstructures* **16** 161 (1994).
- [Bird94c] J. P. Bird, K. Ishibashi, M. Stopa, Y. Aoyagi, and T. Sugano, "Coulomb blockade of the Ahronov-Bohm effect in GaAs/Al/sub x/Ga/sub 1-x/As quantum dots," *Phys. Rev. B* **50**, p. 14983 (1994).
- [Bird94d] J. P. Bird, K. Ishibashi, Y. Aoyagi, and T. Sugano, "Observation of Aharonov-Bohm oscillations in the magnetoresistance of a GaAs/AlGaAs quantum dot," *Japanese Journal of Applied Physics, Part 1 (Regular Papers & Short Notes)* **33**, p. 2509 (1994).
- [Bird94e] J. P. Bird, K. Ishibashi, M. Stopa, R. P. Taylor, Y. Aoyagi, and T. Sugano, "Magneto-Coulomb oscillations," *Phys. Rev. B* **49**, p. 11488 (1994).
- [Bird95a] J. P. Bird, K. Ishibashi, D. K. Ferry, Y. Ochiai, Y. Aoyagi, and T. Sugano, "Phase breaking in ballistic quantum dots: transition from two- to zero-dimensional behavior," *Phys. Rev. B* **51**, 18037 (1995).
- [Bird95b] J. P. Bird, D. M. Olatona, R. Newbury, R. P. Taylor, K. Ishibashi, M. Stopa, Y. Aoyagi, Y. Sugano, and Y. Ochiai, "Lead induced transition to chaos in ballistic mesoscopic billiards," *Phys. Rev. B* **52**, R14336 (1995).
- [Bird95c] J. P. Bird, K. Ishibashi, D. K. Ferry, Y. Ochiai, Y. Aoyagi, and T. Sugano, "Spectral characteristics of conductance fluctuations in ballistic quantum dots: the influence of finite magnetic field and temperature," *Phys. Rev. B* **52**, 8295 (1995).
- [Bird95d] J. P. Bird, K. Ishibashi, Y. Ochiai, Y. Aoyagi, and T. Sugano, "The magnetic field dependent characteristics of conductance fluctuations in ballistic quantum dots," *Japanese Journal of Applied Physics, Part 1 (Regular Papers & Short Notes)* **34**, p. 4342 (1995).

- [Bird96a] J. P. Bird, K. Ishibashi, Y. Aoyagi, and T. Sugano, "Precise period doubling of the Aharonov-Bohm effect in a quantum dot at high magnetic fields," *Phys. Rev. B* **53**, p. 3642 (1996).
- [Bird96b] J. P. Bird, K. Ishibashi, D. K. Ferry, R. Newbury, D. M. Olatnta, Y. Ochiai, Y. Aoyagi, and T. Sugano, "Phase breaking in ballistic quantum dots: a correlation field analysis," *Surface Science*, **361-362**, 730 (1997).
- [Blanter96] Y. M. Blanter, "Electron-electron scattering rate in disordered mesoscopic systems," *Phys. Rev. B* **54**, 12807 (1996).
- [Brouwer95a] P. W. Brouwer and C. W. J. Beenakker, "Effect of a voltage probe on the phase-coherent conductance of a ballistic chaotic cavity," *Physical Review B* **51**, 7739 (1995).
- [Brouwer95b] P. W. Brouwer and C. W. J. Beenakker, "Conductance distribution of a quantum dot with nonideal single-channel leads," *Physical Review B* **50**, 11263 (1995).
- [Brouwer96] P. W. Brouwer, private communication.
- [Brouwer97a] P. W. Brouwer and C. W. J. Beenakker, "Voltage-probe and imaginary-potential models for dephasing in a chaotic quantum dot," *Phys. Rev. B* **55**, 4695 (1997).
- [Brouwer97b] P. W. Brouwer, K. M. Frahm, and C. W. J. Beenakker, "Quantum Mechanical Time-Delay Matrix in Chaotic Scattering," *Phys. Rev. Lett.* **78** 4737 (1997).
- [Brouwer97c] P. W. Brouwer, S. A. van Langen, K. M. Frahm, M. Buttiker, and C. W. J. Beenakker, "Distribution of Parametric Conductance Derivatives of a Quantum Dot," *Phys. Rev. Lett.* **79** 913 (1997).
- [Brouwer97e] P. Brouwer, Ph.D. Thesis, Leiden University, 1997.
- [Brouwer98] P. W. Brouwer and I. L. Aleiner, "Effects of electron-electron interaction on the conductance of open quantum dots" *cond-mat/9807304* (1998).
- [Buks98] E. Buks, A. Schuster, M. Heiblum, D. Mahalu, and V. Umansky, "Dephasing in electron interference by a which-path detector," *Nature*, **391**, 871 (1998).
- [Buttiker86a] M. Büttiker, "Role of quantum coherence in series resistors," *Phys. Rev. B* **33**, 3020 (1986).
- [Buttiker93] M. Buttiker, "Capacitance, admittance, and rectification properties of small conductors", *Journal of Physics: Condensed Matter* **5**, 9361 (1993).

- [Chan95] I. H. Chan, R. M. Clarke, C. M. Marcus, K. Campman, and A. C. Gossard, "Ballistic Conductance Fluctuations in Shape Space," *Phys. Rev. Lett.* **74**, 3876 (1995).
- [Chang94] A. M. Chang, H. U. Baranger, L. N. Pfeiffer, and K. W. West, "Weak-Localization in Chaotic versus Non-chaotic Cavities: A Striking Difference in the Line Shape," *Phys. Rev. Lett.* **73**, 2111 (1994).
- [Choi87] K. K. Choi, D. C. Tsui, and K. Alavi, "Dephasing time and one-dimensional localization of two-dimensional electrons in GaAs/AlGaAs heterostructures," *Phys. Rev. B* **36**, 7551 (1987).
- [Chuang98] I. L. Chuang, L. Vandersypen, X. Zhou, D. Leung, S. Lloyd, "Experimental realization of a quantum algorithm," *Nature* **393**, 143 (1998).
- [Clarke95] R. M. Clarke, I. H. Chan, C. M. Marcus, C. I. Duruöz, J. S. Harris, K. Campman, and A. C. Gossard, "Temperature Dependence of Phase Breaking in Ballistic Quantum Dots," *Phys. Rev. B* **52**, 2656 (1995).
- [Cronenwett97] S. M. Cronenwett, S. R. Patel, C. M. Marcus, K. Campman, and A. C. Gossard, "Mesoscopic Fluctuations of Elastic Cotunneling in Coulomb Blockaded Quantum Dots," *Phys. Rev. Lett.* **79**, 2312 (1997).
- [Cronenwett98] S. M. Cronenwett, et al. "Mesoscopic Coulomb Blockade in Open-channel Quantum Dots," to be published (1998).
- [Datta95] S. Datta, *Electronic Transport in Mesoscopic Systems* (Cambridge Univ. Press, Cambridge, 1995)
- [Dresselhaus92] P.D. Dresselhaus, C.M.A. Papavassiliou, R.G. Wheeler, and R.N. Sacks, "Observation of spin precession in GaAs inversion layers using antilocalization," *Phys. Rev. Lett.* **68**, 106 (1992).
- [Echternach93] P. M. Echternach, M. E. Gershenson, and H. M. Bozler, "Nyquist phase relaxation in one-dimensional metal films," *Phys. Rev. B* **48**, 11516 (1993).
- [Efetov95] K. B. Efetov, "Temperature effects in quantum dots in the regime of chaotic dynamics," *Phys. Rev. Lett.* **74**, 2299 (1995).
- [Efetov97] K. Efetov, *Supersymmetry in Disorder and Chaos* (Cambridge Univ. Press, Cambridge, 1997).
- [Ferry97] D. K. Ferry, *Transport in Nanostructures* (Cambridge Univ. Press, Cambridge, 1997).
- [Feynman65] R. P. Feynman, *The Path Integral Approach to Quantum Mechanics*, McGraw-Hill, 1965.

- [Folk96] J. A. Folk et al., “Fluctuations Statistics and Parametric Correlations of Coulomb Blockade,” *Phys. Rev. Lett.* **76**, 1699 (1996).
- [Fukuyama83] H. Fukuyama and E. Abrahams, “Inelastic scattering time in two-dimensional disordered metals,” *Phys. Rev. B* **27**, 5976 (1983).
- [Furusaki95a] A. Furusaki and K. Matveev, “Coulomb blockade oscillations of conductance in the regime of strong tunneling,” *Phys. Rev. Lett.* **75**, p. 709 (1995).
- [Giuliani82] G. F. Giuliani and J.J. Quinn, J.J., “Lifetime of a quasiparticle in a two-dimensional electron gas,” *Phys. Rev. B* **26**, 4421 (1982)
- [Huibers98a] A.G. Huibers, M. Switkes, C. M. Marcus, K. Campman, A.C. Gossard, “Dephasing in open quantum dots”, *Phys. Rev. Lett.* **81**, 200 (1998).
- [Huibers98b] A.G. Huibers, S.R.Patel, C.M.Marcus, P.W. Brouwer, C.I. Duruoz, J.S.Harris, Jr., “Distributions of the conductance and its parametric derivatives in quantum dots”, *Phys. Rev. Lett.* **81**, 1917 (1998).
- [Huibers98c] A.G. Huibers, M. Switkes, C. M. Marcus, K. Campman, A.C. Gossard, “Dephasing in open quantum dots”, *Physica B* **249-251**, 348 (1998).
- [Imry86] Y. Imry, “Active Transmission Channels and Universal Conductance Fluctuations,” *Europhysics Lett.* **1**, 249 (1986).
- [Imry94] Y. Imry and A. Stern, “Dephasing by coupling with the environment, application to Coulomb electron-electron interactions in metals,” *Semicond. Sci. Technol.* **9**, 1879 (1994).
- [Imry97] Y. Imry, *Introduction to Mesoscopic Physics* (Oxford Univ. Press, Oxford, 1997).
- [Jalabert90] R. A. Jalabert, H. U. Baranger, and A. D. Stone, “Conductance Fluctuations in the Ballistic Regime: A Probe of Quantum Chaos?,” *Phys. Rev. Lett.* **65**, 2442 (1990).
- [Jalabert94] R. A. Jalabert, J.-L. Pichard, and C. W. J. Beenakker, “Universal quantum signatures of chaos in ballistic microstructures,” *Europhys. Lett.* **27**, 255 (1994).
- [Jungwirth96] T. Jungwirth, T. and A. H. MacDonald, “Electron-electron interactions and two-dimensional-two-dimensional tunneling,” *Phys. Rev. B* **53**, 7403 (1996).
- [Katine98] J.A. Katine, M.J. Berry, and R.M. Westervelt, “Determination of the electronic phase coherence time in one-dimensional channels,” *Phys. Rev. B* **57** 1698 (1998).

- [Khavin98] Yu.B. Khavin, M.E. Gershenson, A.L. Bogdanov, "Decoherence and the Thouless crossover in one-dimensional conductors", *Phys. Rev. Lett.* **81**, 1066 (1998).
- [Kouwenhoven97] L.P. Kouwenhoven, C.M. Marcus, P.L. McEuen, S. Tarucha, R.M. Westervelt, and N.S. Wingreen "Electron Transport in Quantum Dots, " in *Nato ASI conference proceedings* ed. By L. P. Kouwenhoven, G. Schön, L.L. Sohn (Kluwer, Dordrecht, 1997).
- [Kurdak92] C. Kurdak, A. M. Chang, A. Chin, and T. Y. Chang, "Quantum interference and spin-orbit interactions in quasi-one-dimensional wires and rings," *Phys. Rev. B* **46**, 6846 (1992).
- [Lee97] Y. Lee, G. Faini, and D. Mailly, "Shape-averaged weak localization in chaotic and integrable ballistic cavities," *Chaos, Solitons & Fractals* **8**, 1325 (1997).
- [Lewenkopf92] C. H. Lewenkopf, A. Müller, and E. Doron, "Microwave scattering in an irregularly shaped cavity: random-matrix analysis," *Phys. Rev. A* **45**, 2635 (1992).
- [Lin86] J. J. Lin and N. Giordano, "Observation of the Nyquist phase-coherence time in thin Au-Pd wires," *Phys. Rev. B* **33**, 1519 (1986).
- [Lin87] J. J. Lin and N. Giordano, "Localization and electron-electron interaction effects in thin Au-Pd films and wires," *Phys. Rev. B* **35**, 545 (1987).
- [Linke97a] H. Linke, P. Omling, Xu Hongqi, and P.E. Lindelof, "Electron-electron interaction in a narrow, disordered electron gas in nonequilibrium" *Phys. Rev. B* **55**, 4061 (1997).
- [Linke97b] H. Linke, L. Christensson, P. Omling, and P.E. Lindelof, "Stability of classical electron orbits in triangular electron billiards," *Phys. Rev. B* **56**, 1440 (1997).
- [Linke97c] H. Linke, J. P. Bird, J. Cooper, P. Omling, Y. Aoyagi and T. Sugano, "Phase breaking of nonequilibrium electrons in a ballistic quantum dot", *Phys. Rev. B* **56**, 14937 (1997).
- [Liu91] J. Liu and N. Giordano, "Weak localization, electron-electron interactions, and Joule heating in the presence of a microwave electric field in thin metal films," *Phys. Rev. B* **43**, 1385 (1991).
- [Liu92] J. Liu and N. Giordano, "Weak localization in the presence of combined magnetic and electric fields," *Phys. Rev. B* **46**, 7027 (1992).

- [Marcus92] C. M. Marcus, A. J. Rimberg, R. M. Westervelt, P. F. Hopkins, and A. C. Gossard, "Conductance Fluctuations and Chaotic Scattering in Ballistic Microstructures," *Phys. Rev. Lett.* **69**, 506 (1992).
- [Marcus93a] C. M. Marcus, R. M. Westervelt, P. F. Hopkins, and A. C. Gossard, "Phase breaking in ballistic quantum dots: Experiment and analysis based on chaotic scattering," *Phys. Rev. B* **48**, 2460 (1993).
- [Marcus93b] C. M. Marcus, R. M. Westervelt, P. F. Hopkins, and A. C. Gossard, "Conductance Fluctuations as Chaotic Scattering," in *Quantum Dynamics of Chaotic Systems*, edited by G. M. Z. J.-M. Yuan (Gordon and Breach, Philadelphia, 1993).
- [Marcus93c] C. M. Marcus, R. M. Westervelt, P. F. Hopkins, and A. C. Gossard, "Conductance fluctuations and quantum chaotic scattering in semiconductor microstructures," *Chaos* **3**, 634 (1993).
- [Marcus94a] C. M. Marcus, R. M. Westervelt, P. F. Hopkins, and A. C. Gossard, "Conductance fluctuations in a quantum dot in the tunneling regime: crossover from aperiodic to regular behavior," *Surf. Sci.* **305**, 480 (1994).
- [Marcus94b] C. M. Marcus, R. M. Clarke, I. H. Chan, C. I. Duruöz, and J. S. Harris, "Phase-Breaking Rates from Conductance Fluctuations in a Quantum Dot," *Semicond. Sci. Technol.* **9**, 1897 (1994).
- [Marcus95] C. M. Marcus, I. H. Chan, R. M. Clarke, K. Campman, and A. C. Gossard, "Statistics of Conductance Fluctuations in Quantum Dots", in *Quantum Dynamics of Submicron Structures*, edited by H. Cerdeira and B. Kramer (Kluwer, Netherlands, 1995).
- [Marcus97a] C. M. Marcus, "Fluctuations in Tunneling and Cotunneling," in *Proceedings from the Curacao Mesoscopics Workshop* (in press), edited by L. Kouwenhoven (1997).
- [Marcus97b] C. M. Marcus, S. R. Patel, A. G. Huibers, S. M. Cronenwett, M. Switkes, I. H. Chan, R. M. Clarke, J. A. Folk, S. F. Godijn, K. Campman and A. C. Gossard, "Quantum Chaos in Open versus Closed Quantum Dots: Signatures of Interacting Particles," *Chaos, Solitons & Fractals* **8**, 1261 (1997).
- [Martinis87] J. Martinis, M. Devoret, and J. Clarke, *Phys. Rev. B* **35**, 4682 (1987).
- [Matveev95] K. A. Matveev, "Coulomb blockade at almost perfect transmission," *Phys. Rev. B* **51**, 1743 (1995).
- [McCann97] E. McCann and I. V. Lerner, "Effect of dephasing on mesoscopic conductance fluctuations in quantum dots with single channel leads," preprint cond-mat/9712160 (1997).

- [Mesoscopic95] Mesoscopic Quantum Physics, edited by G. M. E. Akkermans, J.-L. Pichard and J. Zinn-Justin (Elsevier, Amsterdam, 1995).
- [Millo90] O. Millo, S.J. Klepper, M.W. Keller, D.E. Prober, D.E., S. Xiong, A. D. Stone, R.N. Sacks, "Reduction of the mesoscopic conductance-fluctuation amplitude in GaAs/AlGaAs heterojunctions due to spin-orbit scattering," Phys. Rev. Lett. **65** 1494 (1990).
- [Mittal96] A. Mittal, R. G. Wheeler, M. W. Keller, D. E. Prober, and R. N. Sacks, "Electron-Phonon scattering rates in GaAs/AlGaAs 2DEG samples below 0.5 K," Surf. Sci. **361/362**, 537 (1996).
- [Mohanty97a] P. Mohanty, E. M. Q. Jariwala, and R. A. Webb, "Decoherence and quantum fluctuations," Phys. Rev. Lett. **78** 3366 (1997).
- [Mohanty97b] P. Mohanty and R. A. Webb, "Intrinsic Decoherence in Mesoscopic Systems," Phys. Rev. B. **55** R13452 (1997).
- [Murphy95] S. Q. Murphy, J. P. Eisenstein, L. N. Pfeiffer, and K. W. West, "Lifetime of 2D electrons measured by tunneling spectroscopy," Phys. Rev. B **52**, 14825 (1995).
- [Patel97] S. R. Patel, S. M. Cronenwett, A. G. Huibers, M. Switkes, J. A. Folk, C. M. Marcus, K. Campman and A. C. Gossard, "Universal Fluctuations of Coulomb Blockade Peaks in Quantum Dots," Superlattices and Microstructures **21** 43 (1997).
- [Patel98a] S. R. Patel, S. M. Cronenwett, D. R. Stewart, A. G. Huibers, C. M. Marcus, C. I. Duruz, J. S. Harris, K. Campman, A. C. Gossard, "Statistics of Peak Spacing Fluctuations," Phys. Rev. Lett. **80**, 4522 (1998).
- [Patel98a] S. R. Patel, D. R. Stewart, C. M. Marcus, M. Gokcedag, Y. Alhassid, A. D. Stone, C. I. Duruoz, J. S. Harris Jr, "Changing the Electronic Spectrum of a Quantum Dot by Adding Electrons," Phys. Rev. Lett. **81**, 5900 (1998).
- [Pines96] D. Pines and P. Nozières, The Theory of Quantum Liquids Vol. 1 (Addison-Wesley, New York, 1966).
- [Reulet95] B. Reulet, H. Bouchiat, and D. Mailly, "Magnetoeconductance, weak localization and electron-electron interactions in semi-ballistic quantum wires," Europhys. Lett. **31**, 305 (1995).
- [Simmel97] F. Simmel, T. Heinzel and D. A. Wharam, "Statistics of conductance oscillations of a quantum dot in the Coulomb-blockade regime," Europhys. Lett. **38** 123 (1997).

- [Sivan94a] U. Sivan, Y. Imry, and A. G. Aronov, "Quasi-Particle Lifetime in a Quantum Dot," *Europhys. Lett.* **28**, 115 (1994).
- [Sivan94b] U. Sivan et al., "Spectroscopy, electron-electron interaction, and level statistics in a disordered quantum dot," *Europhys. Lett.* **25**, 605 (1994).
- [Sivan96] U. Sivan, R. Berkovits, Y. Aloni, O. Prus, A. Auerbach, and G. Ben-Yoseph, "Mesoscopic Fluctuations in the Ground State Energy of Disordered Quantum Dots," *Phys. Rev. Lett.* **77**, 1123 (1996).
- [Stewart97] D. R. Stewart, D. Sprinzak, C. M. Marcus, C. I. Duruöz, J. S. Harris, "Correlation Between Ground and Excited State Spectra of a Quantum Dot," *Science* **278**, 1784 (1997).
- [Stewart99] D. R. Stewart, Ph.D. Thesis, Stanford University, 1999.
- [Switkes98] M. Switkes, A. G. Huibers, C. M. Marcus, K. Campman, and A. C. Gosard, "High Bias Transport and Magnetometer Design in Open Quantum Dots," *Appl. Phys. Lett.* **72**, 471 (1998).
- [Tarucha96] S. Tarucha, D. G. Austing, T. Honda, R. J. van der Hage, and L.P. Kouwenhoven, "Shell filling and spin effects in a few electron quantum dot," *Phys. Rev. Lett.* **77**, 3613 (1996).
- [vanWees88] B. J. van Wees, H. van Houten, C. W. J. Beenakker, J. G. Williamson, L. P. Kouwenhoven, D. van der Marel, and C. T. Foxon, "Quantized Conductance of Point Contacts in a Two-Dimensional Electron Gas," *Phys. Rev. Lett.* **60**, 848 (1988).
- [Vitkalov88] S.A. Vitkalov, G.M. Gusev, Z.D. Kvon, G.I. Leviev, V.I. Fal'ko, "Dynamic effect of a microwave field on weak localization", *Sov. Phys. JETP* **67**, 1080 (1988).
- [Wang87] S. Wang and P. E. Lindelof, "Microwave-enhanced phase-relaxation observed in weak-localization experiments", *Phys. Rev. Lett.* **59**, 1156 (1987).
- [Washburn93] S. Washburn and R. A. Webb, "Quantum transport in small disordered samples from the diffusive to the ballistic regime," *Rep. Prog. Phys.* **55**, 1311 (1993).
- [Webb98] R. A. Webb, P. Mohanty, E.M.Q. Jariwala, T.R. Stevenson, A.G. Zharikov, "Decoherence in Mesoscopic Systems", preprint (1998).
- [Wharam88] D. A. Wharam et al., "One-dimensional transport and the quantisation of the ballistic resistance," *J. Phys. C* **21**, L209 (1988).

- [Yacoby91] A. Yacoby, U. Sivan, C. P. Umbach, and J. M. Hong, “Interference and Dephasing by Electron-Electron Interaction on Length Scales Shorter than the Elastic Mean Free Path,” *Phys. Rev. Lett.* **66**, 1938 (1991).
- [Yacoby94] A. Yacoby, M. Heiblum, H. Shtrikman, V. Umansky, and D. Mahalu, “Dephasing of ballistic electrons as a function of temperature and carrier density,” *Semicond. Sci. Technol.* **9**, 907 (1994).
- [Zheng96] L. Zheng and S. Das Sarma, “Coulomb scattering lifetime of a two-dimensional electron gas,” *Phys. Rev. B* **53**, 9964 (1996).